Delft University of Technology

The Soil, Ship, and Fender Structure Interaction During Impact Events

Main Report

by
C.D. Verhoeven

A thesis submitted in partial fulfillment of the requirements for the degree of
Master of Science
in
Civil Engineering

May, 2025

Author:	C.D. (Casper) Verhoeven	
Student number:	5651220	
Project duration:	September 2024 - May 2025	
Chair person:	Dr.ir. K.N. (Karel) van Dalen	Dynamics of Solids & Structures
Second supervisor:	Dr. A. (Athanasios) Tsetas	Dynamics of Solids & Structures
Third supervisor:	Dr. C.L. (Carey) Walters	Ship and Offshore Structure
External supervisor:	Ir. B. (Bart) van Aken	IV

Abstract

In the Netherlands there are many waterways where bridges or locks are situated within the navigation way of inland waterway vessels. To protect these civil structures from potential collision risks, protection structures are placed around them. In this research, a commonly used protection structure, the steel piled fender structure, is analyzed under impact events, followed by a comparison with the design methodology prescribed in the Dutch codes. In the Netherlands, design guidance is provided by the "Richtlijnen Ontwerp Kunstwerken" [1], abbreviated as ROK. The ROK adopts a design formula for the required energy absorption capacity of fender structures from the EAU 2012 [2]. By applying the principle of work, the required energy absorption capacity can be converted into an equivalent static load that incorporates dynamic effects. This allows the soil-fender structure system to be designed using static analysis.

In this research, a triangular-shaped fender structure with fixed geometrical properties is examined. Additionally, the bow structure of a CEMT class IV ship is included to capture the interaction between the ship and the fender structure during impact events. The aim of this study is to obtain a transient response of the system, investigate the interaction between the ship, soil, and fender structure during dynamic impact events, and evaluate this against the design methodology prescribed in the Dutch codes.

To determine the transient response, two different models are developed. A simplified dynamic model based on linear beam theory is constructed. In this model, the problem is reduced to two-dimensional space, where the fender structure is modeled as a 2D frame partially supported by linear elastic foundations representing the surrounding soil. The ship's bow structure is simplified as a mass-spring system attached to the frame structure. Furthermore, a non-linear finite element model (NLFE) is developed in three-dimensional space. The NLFE model includes the full geometry of the fender structure of interest, with the ship's bow structure modeled up to the most frontal bulkhead, and the soil is represented by a series of non-linear discrete springs.

Before performing NLFE impact simulations that account for the full interaction between the ship, soil, and fender structure, an extensive sensitivity study was conducted on the individual models, showing expected behavior. Impact simulations performed during the sensitivity study were used to set up the impact configuration for the final head-on and oblique impact simulations, in which the ship, soil, and fender structure behave flexible simultaneously, allowing full interaction.

A comparison between the simplified model and the head-on impact simulation from the NLFE model revealed different peak responses. The response of the NLFE model was dominated by significant plastic deformations, resulting in larger peak displacements compared to the simplified model. However, during the initial stage of impact loading, dominated by elastic deformations, both models showed good agreement.

Finally, NLFE simulation results are compared to the design methodology prescribed in the Dutch codes. The energy absorption observed in the fender-soil system from the NLFE simulations is compared to the required energy absorption capacity according to the codes. For the head-on impact scenario, significant crushing of the ship's bow led to reduced energy absorption by the fender-soil system. In the oblique impact simulation, the NLFE model predicted higher energy absorption by the fender-soil system compared to the code requirements. There are numerous differences in modelling assumptions between the NLFE model and the method prescribed in the codes. Moreover, the NLFE model includes simplifications of the real-world problem that may lead to an overestimation of the absorbed energy by the fender-soil system. Therefore, extending the NLFE model by removing simplifying assumptions remains highly recommended.

Keywords: Fender structure, Ship impact, Energy absorption capacity, Non-linear finite element simulation

Preface

Dear reader,

This thesis marks the completion of my Master's degree in Civil Engineering at TU Delft, with a specialization in Structural Engineering and a particular focus on structural dynamics. The graduation project was initiated by the engineering firm IV, and the research has been fully carried out at their office in Haarlem, within the department of Steel and Movable Bridges. The central topic of this thesis concerns the design of fender structures in the Netherlands, a subject that required a cross-disciplinary approach combining structural and maritime engineering. This interplay of disciplines introduced complex challenges, which in turn motivated me to thoroughly explore and solve the problem at hand. I am confident that the outcomes of this study provide new insights that may contribute to future design practices.

I would like to express my sincere gratitude to everyone involved in the thesis committee at the TU Delft. Thank you to dr.ir. Karel van Dalen and dr. Carey Walters for generously sharing your knowledge and expertise during our meetings. A special thank you goes to dr. Athanasios Tsetas, for your continuous support, your availability to answer questions, and your guidance throughout the project.

Furthermore, I am very grateful to ir. Bart van Aken and all colleagues at IV's department of Steel and Movable Structures for their trust and for offering me the opportunity to carry out this research. Your support and input have been invaluable.

Lastly, I want to thank my family and friends for their constant support and encouragement throughout this entire journey.

Casper Verhoeven
Haarlem, May 2025

Contents

List of Figures

List of Tables

1

Introduction

The first chapter of this thesis introduces the entire research project. To begin with, a section with background information behind the research problem is included. In this section, a general introduction to fender structures in the Netherlands is provided, the geometry of the fender structure of interest is examined, and a brief description of the current design methodology is given. Secondly, the problem statement including the research questions is presented. Thirdly, the research methodology followed during this research is described. The last section of this chapter outlines the thesis report by presenting a brief description of what is included in each chapter of this thesis.

1.1 BACKGROUND

The Netherlands is characterized by its many waterways and extensive infrastructure. To connect the waterways, locks have been constructed. In order to allow the wet infrastructure to cross the dry infrastructure, many bridges are present. At locations where ships navigate near civil structures, there is a potential risk of collision. To avoid direct collisions between civil structures and ships, protection structures are placed around them. When the skipper does not manage to keep the vessel on the correct navigation line, the protection structure must stop the vessel from moving or bounce it off in another direction to avoid collision with the civil structure. One commonly applied type of protection structure in the Netherlands is a steel-piled fender structure. In figure 1.1 a typical example of such a structure is shown.

Figure 1.1: Steel-piled fender structure around a movable bridge [3]

In the Netherlands, fender structures are often constructed using steel piles with steel crossbeams. In the current design methodology a so-called required energy absorption approach is adopted in the "Richtlijnen Ontwerp Kunstwerken" [1]. According to the design methodology of this code, the required energy absorption capacity of the fender structure is first calculated. The EAU 2012 [2] provides an expression to calculate this required capacity, which is based on the velocity and mass of the reference vessel. Further-

more, four factors are included that account for eccentricities, hydrodynamic mass, ship flexibility, and waterfront attenuation. Relying on the work and energy principle, a static equivalent load is found iteratively. By performing a static structural analysis, the fender structure is designed based on this equivalent static load, and a soil failure check is performed. The current design methodology provides an efficient way in designing fender structures without performing dynamic calculations. However, the nature of the process includes many dynamic effects that are simplified and approached by factors in this methodology. Furthermore, the codes do not provide solid statements for the coefficients when calculating the required energy absorption in different design situations.

In this research, a recently constructed (2019) fender structure is used as a case study. Therefore, fixed geometry and cross-sectional properties are maintained throughout this research. Figure 1.2 provides an overview of the geometry of the structure of interest. The structure consists of five piles of length 18.8m, which are connected by triangular-shaped frames in the horizontal plane at three different heights.

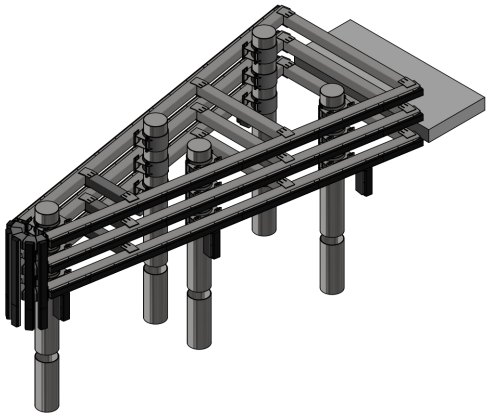

Figure 1.2: 3D view: geometry fender structure

For the structure of interest, there are two different impact scenarios possible: head-on or oblique. A head-on impact can be seen as a extreme impact event for which fender structures are normally not designed to. This impact scenario is included to gather insights about the structural behavior of the soil and the fender structure in case of occurrence of such an extreme event. Are fender structures, how they are designed nowadays, able to withstand the loads during head-on impacts, and what could be the consequence if this occurs? Those questions form the basis for including this scenario in this research. The oblique impact scenario can be described as a general impact scenario for the serviceability state of the fender structure. The soil and fender structure should be able to absorb the impact while maintaining in the elastic regime. Therefore, no permanent deformations occur and after the impact event all structural elements return to their initial state. A schematic overview of the two prescribed impact scenarios is presented in figure 1.3. In the figures, the ship is shown in yellow. The fender structure is recognizable trough the triangular shaped geometry in blue. Furthermore, the initial contact point during the impact is highlighted in red.

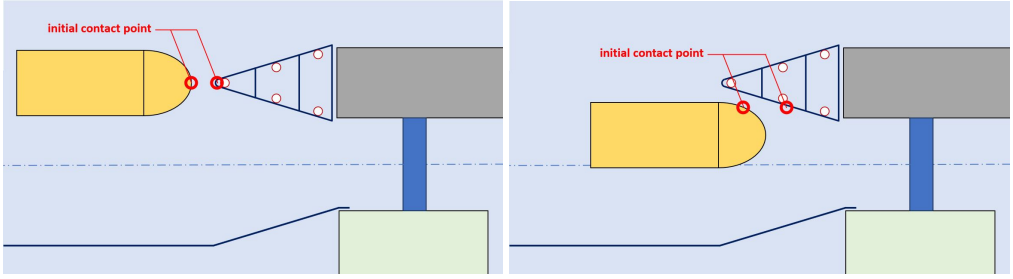

(a) Head-On **(b)** Oblique

Figure 1.3: Impact scenarios impact analysis

1.2 PROBLEM STATEMENT

The main problem of this study is that in the current design method dynamic effects are incorporated into factors that are used to calculate an upper bound for the required energy absorption capacity of fender structures. By examining the dynamic process and taking into the account the interaction between the ship, soil, and fender structure, a better understanding can be obtained with respect to the design of this type of protection structure. By performing a dynamic analysis, the accuracy of the current design method can be assessed.

This research solely focuses on the interaction between the ship, soil, and fender structure. Therefore, hydrodynamic effects caused by the fluid are not considered in this research. Instead, these effects are simplified by added mass to the ship structure, a common used approach in design methods prescribed in engineering codes.

A wide range of ships navigate the Dutch waterways, each with different geometries, structures, and load capacities. However, in this research only one ship structure, classified as CEMT class IV, is included. In the master's thesis by B. Meijer, three bow structures for inland waterway vessels are analyzed [4]. The structural and geometrical data of the CEMT class IV ship used in this research are based on that work. The corresponding model input files are provided at the beginning of this thesis.

1.2.1 Research Questions

To reach the objective of the research the following main research question is formulated:

What is the transient response of the ship, soil, and fender structure system during head-on and oblique impact events, and how does this compare to the equivalent static load method used in the Dutch codes?

Sub-research questions are formulated to break down the complexity of the research. Each sub-research question forms an integral part in answering the main research question at the end of this thesis.

- How can the behavior of the soil be modeled using force-displacement (P-y) relationships derived from CPT data?
- How does the ship's bow structure behave under impact loading, and how is this influenced by the model input parameters?
- How does the soil-fender structure system behave under impact loading, and how is this influenced by the model input parameters?
- How is the ship's initial kinetic energy distributed among the ship, soil, and fender structure during impact events?

1.3 RESEARCH METHODOLOGY

In this section, the research methodology is described. This methodology serves as a guideline that has been followed throughout the research, with the goal of conducting well-structured research that provides reliable answers to the research questions.

First, a background study is conducted to obtain a better understanding of the problem at hand. The background study begins with a review of the current design methodology used in engineering practice, as prescribed in the Dutch codes. By doing this, knowledge is obtained about the design requirements that fender structures generally need to fulfill. Furthermore, a study of laterally loaded piles in sandy soils is conducted. Two different methods for obtaining CPT-based force-displacement relations are studied, followed by a section that focuses on a material model for structural steels in non-linear finite element analysis. At the end of the background study, cylinder buckling failure of steel piles is examined.

Secondly, a detailed impact simulation approach is established. Two different methods are adopted with the aim of obtaining the transient response of fender structures during an impact with a ship. One is called the "simplified model", which relies on a linear dynamic model. The second model is called the "non-linear finite element model". Using these two models, the objective is to study the interaction between soil, ship, and fender structure during head-on and oblique impact events. To reach this objective, multiple simulations need to be performed. Therefore, a well-structured simulation approach was required.

Thirdly, the non-linear finite element (NLFE) model and the simplified model are developed. For the NLFE model, geometries are modeled first in 3D using Ansys SpaceClaim, followed by the definition of the boundary conditions, material models, and specifying general solver settings for the numeric solver. The simplified model, is developed based on a system of partial differential equations using the Euler-Bernoulli beam theory, In the simplified model, the impacting ship is simplified as a mass-spring system. After defining the boundary conditions, a solving strategy is employed to solve the dynamic system for the transient response. To do this, modal analysis is adopted in this research.

Finally, transient responses are obtained by running the impact simulations in LS-DYNA or by solving the simplified model. For the last one, a free vibration analysis is performed first. This results in the natural frequencies with corresponding mode shapes of the frame structure. Add an extra equation of motion for the mass-spring system, formulate a system of ordinary differential equations by employing the modal analysis, and solve for the unknown displacements over time. For the NLFE model, impact simulations are first performed by including only the flexibility of either the ship structure or the fender-soil system. These preliminary simulations are used to study the structural behavior of the individual systems under impact loading, to address possible sensitivities to input parameters, and to set up the final simulation configuration for the head-on and oblique impacts, in which all systems behave flexibly simultaneously. In the end, simulation results from the simplified model and the NLFE model are compared, and a comparison between the NLFE model and the Dutch codes is made. The simulation results, as well as the comparisons, are used to answer the research questions and formulate the conclusions. In addition, recommendations for future research are provided.

1.4 THESIS OUTLINE

This section outlines the thesis report for the remaining chapters.

CHAPTER 2 BACKGROUND The second chapter presents the background study and begins with two sections that include a study of the design standards/guidelines for the Dutch waterways and fender structures. A third section covers laterally loaded piles in sandy soils, and a fourth section covers material models for structural steels. Finally, a section is included on cylinder buckling.

CHAPTER 3 IMPACT SIMULATIONS APPROACH The third chapter includes a description of the impact simulation approach. In the first section, the simplified model is described. The second section includes an overview of the simulations for the NLFE model. The last section includes information about the solving strategy used for the NLFE model.

CHAPTER 4 DEVELOPMENT NON-LINEAR FINITE ELEMENT MODEL The fourth chapter presents the development of the non-linear finite element model. The first three sections evaluate the unit system, model geometries, and boundary conditions, followed by a section on the steel material models. Finally, the last section describes the general solver settings.

CHAPTER 5 SIMPLIFIED DYNAMIC MODEL The fifth chapter includes the development of the simplified model. This chapter begins with a section about the schematization of the dynamic model. Element formulations are given in the second section. The final section describes the modal analysis and the applicability to this problem.

CHAPTER 6 RESULTS AND DISCUSSIONS The sixth chapter provides the results and discussions from the simplified model in the first section, followed by the sensitivity analysis and simulations results with discussions in two separate sections. In the last two sections, a comparison between the simplified model and the NLFE model and a comparison between the NLFE model and Dutch codes is presented.

CHAPTER 7 CONCLUSIONS AND RECOMMENDATIONS In the final chapter of this thesis, research questions are answered and conclusions are presented. Finally, recommendations for future research are included at the end of this chapter.

2

Background

In this chapter required background information is gathered to get a better understanding of the problem. To begin with, a background study to the system of Dutch inland waterways, and current design methodology is conducted. Followed by a theoretical background study in modelling the soil behavior related to laterally loaded piles. Furthermore, a recommended material model for structural steel in non-linear finite element analysis is studied. Finally, cylinder buckling, a well known failure mechanism of cylindrical piles is examined.

2.1 THE DUTCH WATERWAYS

2.1.1 Reference vessels

In Europe there is a classification system that divides inland vessels into separate classes. This system was accepted by the Conferénce Européenne des Ministres des Transports (CEMT) for the first in 1954. Later on in 1992, this system is expanded with the increasing ship sizes ending up with a classification system started at CEMT class I up to class VII. In 2010, a modified classification system is adopted in The Netherlands by Rijkswaterstaat (RWS) because the CEMT1992 is no longer representative anymore.

The largest vessel that is able to navigate through the waterway will be the reference vessel for the design of the waterway itself. Normally, every waterway has three reference vessels: a motor vessel, a pushed convoys, and a coupled unit. For every type and CEMT class the following properties are defined: beam, length, draught, and cargo capacity. Furthermore, in the Richtlijnen Ontwerp Kunstwerken [1] the maximum sailing velocity per CEMT class is described.

Since this research only focuses on motor cargo vessels, only the characteristics for this type of vessel are provided in table 2.1.

Table 2.1: Characteristics motor vessels

CEMT class	**beam**[1] [m]	**length**[1] [m]	**draught**[1] [m]	**deadweight tonnage**[2] [ton]	**sailing velocity**[2] [m/s]
I	5.05	38.5	2.5	400	4.1
II	6.6	50 – 55	2.6	650	4.8
III	8.2	67 – 85	2.7	1000	5.1
IV	9.5	80 – 105	3.0	1500	5.3
Va	11.4	110 – 135	3.5	3000	5.5
VIa	17.0	135	4.0	6000	4.5

[1] Recommended values in Waterway Guildines 2020 [5]
[2] Recommended values in Richtlijnen Ontwerp Kunstwerken [1]

2.1.2 Ship manoeuvres around locks and bridges

In 1994, prototype measurements have been conducted to the ship manoeuvres around a few locks along the Maasroute in The Netherlands [6]. The goal of this measurements was to investigate the relations between sailing velocity, angle between navigational channel with respect to fender structure, and the mass of the ship.

To begin with the relation between sailing velocity and the mass of the ship. Based on the measurements graphs are developed which show the relation between mass of the ship and the sailing velocity perpendicular to the fender structure. In figure 2.1 two graphs are shown for a funnel with an angle of 1:6 for both unloaded and loaded ship conditions. To obtain the values of figure 2.1 the measured sailing velocities are extrapolated as a function of the ship's mass. Therefore, the graphs show three different lines each corresponding with a probability of exceedance (p=0.1, p=0.01, and p=0.001). According to the report of the prototype measurements [6], the results are representative during normal till nautical gushing sailing conditions. Therefore, the values from these graphs are not representative when designing for extreme evasive sailing maneuvers of the ship.

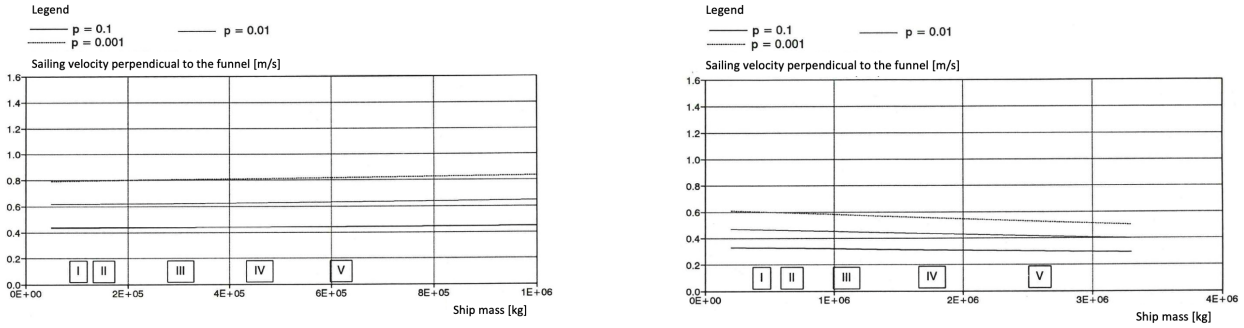

(a) unloaded ship

(b) loaded ship

Figure 2.1: Sailing velocity perpendicular to the fender structure [6]

In the ROK [1] and the Dutch Waterway Guidelines [7] values are prescribed for inland vessels passing fender structures. If the distance between the bridge/lock and the fender structure is smaller than the length of the ship being considered, an impact sailing velocity of 3.0 m/s is prescribed. Note that, no distinction is made for between different CEMT classes or loading conditions of the ship. Assuming that the ship is sailing perfectly in the direction of the channel axis, the sailing velocity perpendicular to the fender structure ($v_\perp$) can be derived filling in (2.1). Doing this, results into a value of $v_\perp$ = 0.5 m/s.

$$v_\perp = v \cdot \sin(\theta) \tag{2.1}$$

Where:
v is the sailing velocity of the ship
θ is the funnel angle of the fender structure

Drawing a horizontal line at the value of $v_\perp$ equal 0.5 m/s and a vertical line at m_s equal 1500 tons gives figure 2.2. From this figure, it can be concluded that the value prescribed in the Dutch standards falls in between the probability of exceedance range of p = $[0.001, 0.01]$.

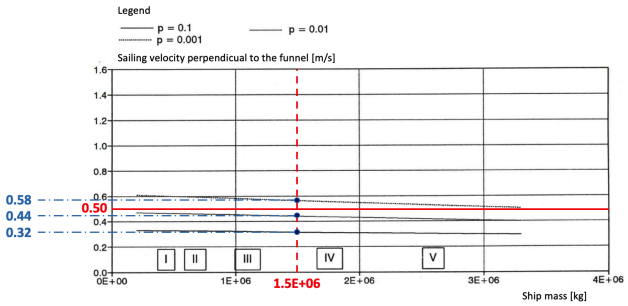

Figure 2.2: Comparison ROK with prototype measurements (modified [6])

2.2 EQUIVALENT STATIC LOAD METHOD FOR THE DESIGN OF FENDER STRUCTURES

In The Netherlands, a large part of the fender structures are in the posses of Rijkswaterstaat (Dutch governmental organization). Besides the well known Eurocodes [8, 9, 10, 11] that provides standards for the design and or renovation of structure, Rijkswaterstaat provides the "Richtlijnen Ontwerpen Kunstwerken" (ROK) [1] as a supplement to the Eurocodes.

The ROK prescribes the design specifications and practical requirements that fender structures need to fulfill. However, those are only applicable under loading conditions where a ship needs to berth, moor, or navigate safely along a civil structure. Therefore, designing for extreme evasive maneuvers is excluded withing design specifications.

2.2.1 Required energy absorption

A "required energy absorption capacity" methodology is adopted in the codes. Based on the situation at interest an energy absorption quantity (E_d) can be calculated. This is the point where the ROK refers to the EAU 2012 [2], in this guideline document an expression is given to calculate the required energy absorption capacity (2.2). This equation is based on the conventional kinetic energy equation from physics multiplied with four coefficients.

$$E_d = \frac{1}{2} \cdot G \cdot v_{\perp}^2 \cdot C_e \cdot C_m \cdot C_s \cdot C_c \tag{2.2}$$

Where:
G = mass of ship
$v_{\perp}$ = sailing velocity perpendicular to fender structure
C_e = eccentricity coefficient
C_m = virtual mass coefficient
C_s = ship flexibility coefficient
C_c = waterfront structure attenuation coefficient

The fender structure must be designed based on this resulting energy absorption capacity. The next section explains how this is done in common engineering practice.

2.2.2 Energy capacity design approach

The energy absorption capacity of a structure can be found based on the force-displacement relation. The energy absorbed by the structure equals the area under the force-displacement curve. Following the design methodology from the codes, an equivalent static load (F) has to be found iteratively by performing

a static structural analysis to the soil-fender structure system. The resulting energy absorption capacity of the soil-fender structure system (E) can be obtained using (2.3).

$$E = \int_0^{s_{max}} F(s) \cdot ds \tag{2.3}$$

Where:
$F(s)$ = equivalent static load dependent on the displacement
s = displacement at load application point

2.3 LATERALLY LOADED PILES IN SOILS

The piles of the fender structure are partly embedded into the soil. Above ground level the pile spans the water column and reaches into the air. This can simply be schematized in 2D as a monopile embedded in the soil. In figure 2.3 the soil is represented by the brown/yellow colored layers with on top the fluid in blue. The monopile is visualized in light blue.

Fender structures need to fulfill the purpose of transferring the horizontal load through the steel structure into the surrounding soil. Therefore, the technique used in modelling the soil could have large consequences to the response of the system. A commonly applied method in engineering is to model the soil as a series of springs. The springs can be modeled as linear, bi-linear, or nonlinear springs dependent on the expected behavior of the soil. In this section two different relations are considered:

- Bi-linear curves based on Ménard with Brinch-Hansen [12, 13].
- Hyperbolic tangent curves based on the API-method [14].

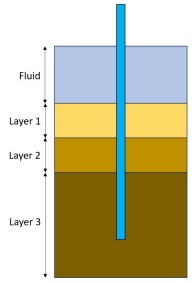

Figure 2.3: Soil layering

Figure 2.4 shows the proposed shapes for the P-y relationships for both methods. In both cases, it can be seen that curves have a clear upper bound that represent the ultimate soil resistance. With the use of this curves it is assumed that the soil pressure remains constant once it reaches the ultimate soil resistance.

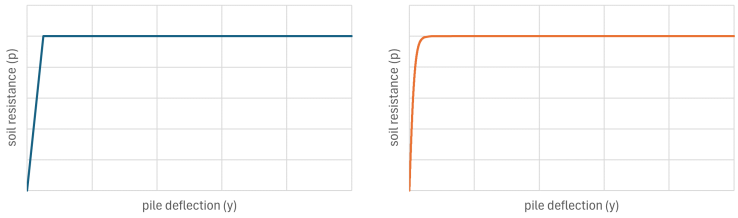

(a) Ménard with Brinch-Hansen **(b)** API-method

Figure 2.4: Comparison shape P-y curves for both methods

2.3.1 Ménard in combination with Brinch-Hansen

The Brinch-Hansen [13] and Ménard [12] method is a semi-empirical approach combining theoretical bearing capacity principles proposed by Brinch-Hansen with in-situ soil stiffness measurements obtained from Ménard Pressuremeter Tests (PMT).

In the research conducted by Brinch-Hansen, relationships were found for the ultimate resistance for

laterally loaded piles in soil. In this proposed method, the pile is assumed to be rigid, square shaped, and rotates around a fixed point. Furthermore, the soil is assumed to be uniform over depth. Based on bearing capacity factors that account for soil properties, pile geometry, and embedment depth, an estimation can be derived for the lateral load capacity of the pile. Brinch-Hansen only considers passive soil pressures. The maximum horizontal passive effective soil pressure can be calculated using (2.4).

$$\sigma\prime_p = K_q \cdot \sigma\prime_v + K_c \cdot c \tag{2.4}$$

Where:
K_q = earth pressure coefficient for overburden pressure
$\sigma\prime_v$ = effective vertical pressure
K_c = earth pressure coefficient for cohesion
c = cohesion

In the determination of the earth pressure coefficient distinction is made between soil layers at ground level and at great depth. The Brinch-Hansen method is a so-called ultimate resistance approach, and therefore can only estimate the response under ultimate loading conditions. As a result, this method can not be used (solely) to calculate deformations of the soil and pile under working load conditions.

Ménard conducted research to the modulus of horizontal subgrade reaction for different soil types. In this research, a relation between the pressuremeter modulus and the modulus of subgrade reaction was found. This relation is given in (2.5).

$$\begin{aligned} \frac{1}{k_h} &= \frac{1}{3E_m}\left[1.3R_0\left(2.65\frac{R}{R_0}\right)^{\alpha} + \alpha R\right] \quad \text{for } R \geq R_0 \\ \frac{1}{k_h} &= \frac{2R}{E_m}\frac{4\,(2.65)^{\alpha} + 3\alpha}{18} \quad \text{for } R < R_0 \end{aligned} \tag{2.5}$$

Where:
k_h = modulus of horizontal subgrade reaction
E_m = pressiometer modulus
R_0 = reference radius (3.0 meter)
R = pile radius
α = rheological coefficient

When combining Ménard with Brinch-Hansen, bi-linear curves can be obtained for laterally loaded piles. Special relations are obtained that relates the derived pressuremeter modulus to the point resistance of Cone Pressure Test (CPT). Full written out mathematical expressions are provided in appendix A.

2.3.2 The API Method

The API-method [14] also propose a set of equations to calculate the ultimate soil resistance. This method was originally introduced by Reese et al. [15] by performing full-scale tests on laterally loaded piles in sandy soils in 1974. Later on in 1980, the equations where simplified when researchers realized that some terms in the formulation of the ultimate soil resistance could be taken as constants. This resulted into a set of equations presented in (2.6).

$$\begin{aligned} P_{us}(z) &= (C_1 \cdot z + C_2 \cdot D)\,\gamma' \cdot z \\ P_{ud}(z) &= C_3 \cdot D \cdot \gamma' \cdot z \\ P_u(z) &= \min(P_{us}(z), P_{ud}(z)) \end{aligned} \tag{2.6}$$

Where:
P_{us} = ultimate soil resistance at shallow depth
p_{ud} = ultimate soil resistance at deep depth

$\gamma\prime$ = submerged soil unit weight
z = depth below the original seafloor
C_1, C_2, C_3 = coefficients as function of internal friction angle ($\phi\prime$)

In the derivation of the ultimate soil resistance not only passive earth pressures are accounted for. In contradiction to the method from section 2.3.1, the API-method also takes into account active and neutral earth pressures in deriving relations for the ultimate soil pressure. Furthermore, distinction is made between shallow an deep failure of the soil. At shallow depths the soil failure is schematized by a wedge shaped failure. At great depths, the soil will undergo so-called flow failure. Full written out mathematical expressions are provided in appendix A.

Once the ultimate soil resistance is known, the non-linear P-y curve can be derived following (2.7).

$$P = A \cdot P_u \cdot \tanh\left[\frac{k \cdot z}{A \cdot P_u} \cdot y\right] \tag{2.7}$$

Where,
A = factor to account for static or cyclic loading condition
k = rate of increase with depth of initial modulus of subgrade reaction
y = lateral deflection at depth z

2.3.3 Multi-directional P-y curves

Until this point the P-y method is only defined for uni-directional loading cases. Therefore, when analyzing 2D problems both methods can be efficiently applied. However, loads do not act always in a single direction. When analyzing 3D problems with non symmetric load conditions, such as eccentricities, an uni-directional model is not sufficient to obtain a realistic response. In [16], a computational efficient method without the need of extra soil properties is proposed to transform P-y relations from uni directional to multi directional. This method is based upon the assumption that the multi-directional P-y curves can be described using the same mathematical expression as the uni-directional curves. The principle of this transformation is visualized in figure 2.5. In the multi-directional case the soil is not represented by springs acting only in one direction. Instead of this, the monopole is now supported by springs in all directions of the xy-plane. Figure 2.5a shows an example of this. In this figure, eight springs are equally spaced around the circumference of the pile. Making the assumptions that the pile always moves in the direction in which one of the springs is oriented, and only springs in compression will be activated. It can be said that the lateral force is absorbed by $N/2-1$ springs for N being an even integer number representing the number of springs around the circumference at a given cross section of the pile. The change of length per spring at a given displacement of the pile can easily be calculated using: $u_j = x\cos\theta_j + y\sin\theta_j$. A visualization of this is given in figures 2.5b and 2.5c.

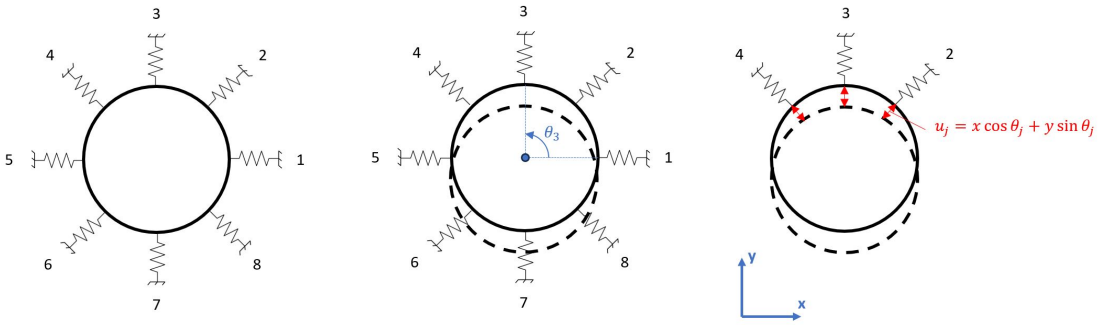

(a) No displacements **(b)** Angle θ_j **(c)** Change of length u_j

Figure 2.5: Cross-section view multi-directional spring model

In literature, two formulas are proposed that transform the modulus of subgrade reaction (2.8) and the ultimate soil resistance (2.9) from uni-directional (k, P_u) to multi-directional parameters ($\tilde{k}$, $\tilde{P}_u$) [17]. This two formulas are derived with the aim to minimize the difference between external work performed by the spring(s) in the uni- and multi-directional model and can be applied to both bi-linear and tangent hyperbolic P-y curves.

$$\tilde{k} = \frac{4k}{N} \tag{2.8}$$

$$\tilde{P}_u = \tan\left(\frac{\pi}{N}\right) \cdot P_u \tag{2.9}$$

2.3.4 A Uni-/Multi-directional comparison

A numerical example, for the tangent hyperbolic case, is included to see what the possible differences are between the uni- and multi-directional model while applying the method from section 2.3.3. Therefore, a test case is compiled. In this case the soil layering, soil properties, and pile cross section are kept constant. The only difference is made in the way the pile is formulated and what directional model is applied. To begin with, figure 2.6a shows a monopile that is modeled using beam elements. The beam model is used to simulate the response of the uni-directional model. In figure 2.6b also the soil springs are included. The model is oriented in the xy-plane and is constrained in the z-direction. Because the assumption of compression only springs is made, the beam must be supported by springs at both sides of the beam. Separation between the soil layers with different properties is visualized with the use of different coloring in green, yellow, brown, and red.

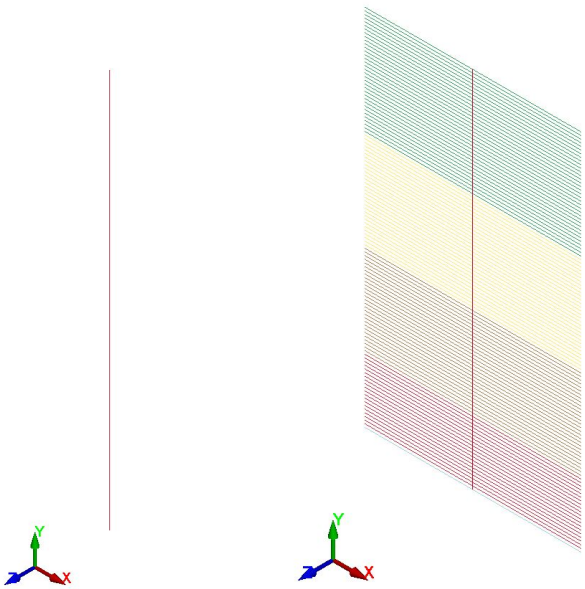

(a) Beam model **(b)** Beam model with springs

Figure 2.6: Uni-directional soil model

For the multi-directional model, the monopile is modeled with shell elements as shown in figure 2.7a. The shell model is used for the test case of the multi-directional model and therefore contains springs in all directions around the circumference of the cross section of the pile as shown in figure 2.7b. In this model a soil spring is generated at every mesh node of the shell. With the applied mesh size this corresponds to a value of $N = 24$ springs around the pile's circumference.

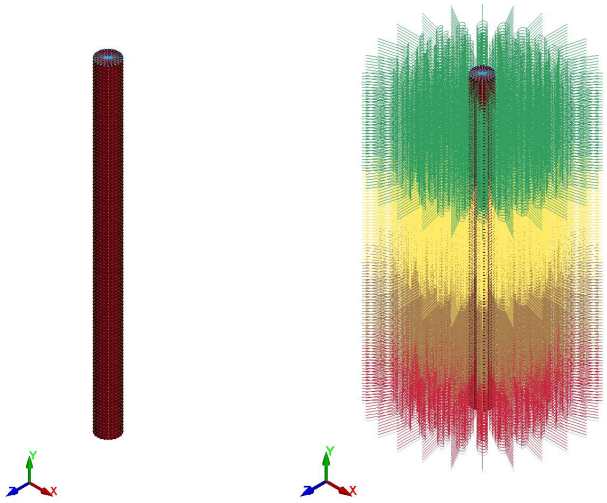

(a) Shell model **(b)** Shell model with springs

Figure 2.7: Multi-directional soil model

Both models are simply supported in the y-direction at the bottom of the pile. At the top of the pile, a boundary condition with a prescribed motion is used to generate relations between the spring force and horizontal deflection of the pile. Results from the test case are presented in figure 2.8. In this graph the relation between the spring force versus the lateral displacement of the pile is shown for both the uni- and the multi-directional model at a single soil layer in depth. This means that for the uni-directional curve the data is only extracted from a single spring and for the multi-directional curve all 24 spring forces (in x-direction) are summed up. For small values of lateral displacement both models almost follow the same path. When the lateral displacement becomes larger, and the transition from elastic to plastic behavior occurs, a small gap occurs between the two models. Though, this is assumed to be acceptable during this research.

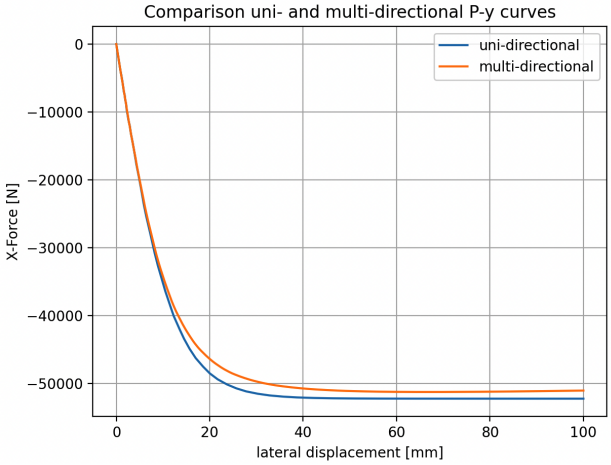

Figure 2.8: Force-Displacement curves soil test case

2.4 MATERIAL MODEL STRUCTURAL STEELS

In numerical simulations of structural impact events, the selection of an appropriate material model is crucial to obtaining realistic and reliable results. The material model defines how a material responds to loading, particularly in non-linear finite element analysis (FEA), where large deformations, plasticity, and strain-rate effects could play a significant role. If the material model is not chosen properly, the resulting

behavior can deviate significantly from reality since it highly influences the stress distributions, failure predictions, and energy dissipation within the system [18].

Steel material properties are generally derived from uniaxial tensile tests. A schematization of an uniaxial tensile test is presented in figure 2.9. In this figure, a test specimen is showed with corresponding engineering stress-strain curve.

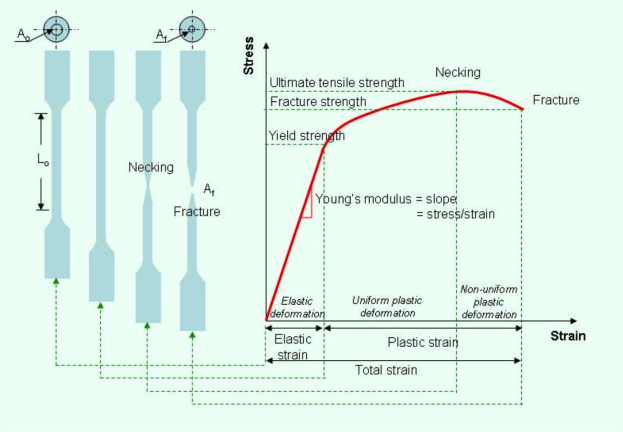

Figure 2.9: Stress-Strain relationship under uniaxial tensile loading [19]

This research employs the DNV-RP C208 (Determination of structural capacity by non-linear finite element analysis methods) [20] recommended material model, which provides a true-stress strain relationship for structural steels ranging from S235 to S460. True stress-strain relations can be directly obtained from engineering stress-strain relations as described in the code. The next paragraph will elaborate on this in more detail.

2.4.1 Recommended true stress-strain curve

The recommended true stress-strain curve following the DNV-RP C208 [20] is presented in figure 2.10. The recommended curve is built up out of two stepwise linear parts, referred to as part 1 and 2, followed by a third power law curve. It must be noted that this recommended curve does not prescribe an end point where fracture of the material occurs.

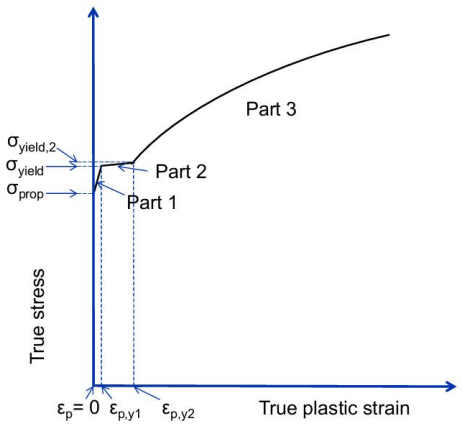

Figure 2.10: Definition true stress-true plastic strain curve [20]

A relation between the stress and strain is provided in the DNV-RP C208 for the third part, as presented in (2.10).

$$\sigma = K\left(\varepsilon_p + \left(\frac{\sigma_{yield,2}}{K}\right)^{\frac{1}{n}} - \varepsilon_{p,y2}\right)^n \quad \text{for } \varepsilon_p > \varepsilon_{p,y2} \tag{2.10}$$

2.5 CYLINDER BUCKLING

For the design of energy-absorbing pile structures, flexural flexibility of the structure plays an important role in the energy-absorption capacity [21]. The degree of flexibility of the structure is one of the main parameters that determine the softness of the impact. The flexibility of a structure can also be expressed by its slenderness. In the Eurocode 1993-1-1 [10] this is expressed by the D/t ratio, also referred to as ductility ratio, of the pile. In which "D" denotes the pile diameter and "t" the wall thickness of the cross section. Piles with a high D/t ratio are more susceptible to local instabilities, like local buckling, in the cross section.

In the Eurocode a distinction is made between three ductility classes. The D/t ratio characterizes the profile class of a given tubular section. Limit values for this are shown in table 2.2. Class 1 corresponds to the pile group with the lowest slenderness ranging up to class 4 which are the pile group with the highest slenderness. A distinction is made between class 3a and 3b where for the latter one a special Eurocode is developed for strength and stability of shell structures (part 1-6).

Table 2.2: Ductility classes [10]

Class	Limits
1	$D/t \leq 50\varepsilon^2$
2	$50\varepsilon^2 < D/t \leq 70\varepsilon^2$
3a	$70\varepsilon^2 < D/t \leq 90\varepsilon^2$
3b	$D/t > 90\varepsilon^2$

The strain value (ε) must be calculated using (2.11).

$$\varepsilon = \sqrt{\frac{235}{f_y}} \tag{2.11}$$

The ductility class characterizes the behavior of circular tubes under bending or compressive load conditions. Ductility classes 1 and 2 allow the cross section to fully develop the plastic moment. If the cross section is classified to be 3a, only the full elastic moment can be developed. When the D/t ratio of the tube is larger then the value given in for class 3b, local buckling can occur before the elastic yield limit is reached in the cross section of the tube. Therefore, special attention needs to be taken when using tubes with high D/t ratios.

3

Impact Simulations Approach

This chapter discusses the methods applied to derive the transient response for various impact scenarios. Two different approaches are utilized. The first method, described in section 3.1, is a combined analytical/numerical approach. The second method, given in section 3.2, involves non-linear finite element (NLFE) computer simulations. At the end of this chapter, a framework followed in developing and solving the non-linear finite element models is provided.

3.1 SIMPLIFIED MODEL

A simplified model is developed in Chapter 5. Using this model, the head-on impact between a ship and a fender structure is analyzed. In this approach, the ship structure is simplified as a mass-spring system, while the fender structure is represented as a two-dimensional (2D) frame structure. By applying Euler's beam theory, a set of partial differential equations is formulated. A free vibration analysis is then conducted to numerically obtain the natural frequencies and mode shapes of the system. Subsequently, the transient response is derived using the modal superposition principle for the frame structure coupled with the mass-spring system.

3.2 NON-LINEAR FINITE ELEMENT SIMULATIONS

The second method employs a model with a higher level of detail to obtain the transient response of the ship, soil, and fender structure during impact events. In this approach, non-linear finite element models are developed for the ship structure, fender structure, and non-linear soil springs that represent the surrounding soil. The development of these models is further described in chapter 4.

This section focuses on the simulation approach used in this research. Non-linear finite element analysis is characterized by numerous input parameters. To manage complexity, the ship structure model and the combined model of the fender structure with soil are initially studied independently. This step allows for a better understanding of the behavior of each model under impact loading conditions. Additionally, these simulations help address sensitivities in the models to various input parameters. Finally, mesh convergence studies are conducted at model level to ensure accuracy and reliability.

3.2.1 Ship model

Related to the ship model, a total of five impact simulations are performed. An overview is provided in table 3.1. The simulations are grouped based on the parameter of interest being investigated. Each group is identified by an alphabetical letter followed by a simulation number within that group. The first model, referred to as A1, serves as the reference model. This reference model establishes the base parameters for the study, with deviations applied to only one parameter at a time.

Table 3.1: Simulations overview: impacting ship

Simulation	Object	Material model	Static friction coefficient
A1	rigid wall	non-linear	0.3
A2	rigid wall	bi-linear	0.3
B1	rigid wall	non-linear	0.1
B2	rigid wall	non-linear	0.5
C1	rigid cylinder	non-linear	0.3

The first group of simulations (Group A) consists of two head-on impact simulations between the ship and a rigid wall, focusing on different steel material models. An elastoplastic-hardening stress-strain curve is implemented in simulation A1. Simulation A2 adopts another commonly used stress-strain relationship, represented by a bi-linear curve.

The static friction coefficient exhibits significant variability in real-world scenarios depending on the type of material between the contacting surfaces. Typically, friction-reducing materials are applied to protection structures. However, due to variations in material properties and potential changes caused by wear, two additional simulations are included in Group B. These simulations evaluate lower (0.1) and higher (0.5) static friction coefficients. The results enable an assessment of the sensitivity of this specific parameter on the response of the impacting ship.

Finally, Group C investigates the influence of the geometry of the impacting object. In simulation C1, the rigid wall is replaced with a cylindrical-shaped object that has a narrower width compared to the ship's bow structure.

3.2.2 Soil-Fender Structure Model

Similar to the ship model, several simulations are performed to understand the structural behavior of the fender structure under impact loads and assess sensitivities to input parameters. In this section, a distinction is made between head-on and oblique impact scenarios.

An overview of the head-on impact simulations is provided in Table 3.2, which includes three simulations. Simulation D1 is defined as the reference model for the head-on scenario. The same approach is applied to the oblique impact simulations, with the performed simulations listed in Table 3.3. For the oblique scenario, five simulations are conducted, with F1 serving as the reference model.

First, group D simulations are performed to examine the effect of the steel material models under impact loading of the fender structure. Furthermore, simulation E1 is added to evaluate the influence of the soil model.

Table 3.2: Simulations overview: impacting fender structure (head-on)

Simulation	Material model	Friction (μ)	Soil model
D1	non-linear	0.3	API-method
D2	bi-linear	0.3	API-method
E1	non-linear	0.3	Ménard with Brinch-Hansen

For the oblique impact scenarios, group F serves the purpose to evaluate the structural behavior for different static friction coefficients. Simulation G1, just as with the head-on impact scenario examines the effect of the applied soil model. Finally, simulations H1 and H2 are added to examine the effect of the impact position.

Table 3.3: Simulations overview: impacting fender structure (oblique)

Simulation	Static friction coefficient	Soil model	Impact position
F1	0.3	API-method	middle crossbeam
F2	0.1	API-method	middle crossbeam
G1	0.3	Ménard with Brinch-Hansen	middle crossbeam
H1	0.3	API-method	lower crossbeam
H2	0.3	API-method	upper crossbeam

3.2.3 Final impact simulation models

The results gathered and data generated during the reduced-complexity impact simulations are not intended to directly answer the main research question of this thesis. However, results from simulations A1 to H2 will be used to relate findings from the complex model, where both the ship and fender structure exhibit flexibility during impact. Additionally, input parameters for the combined model are defined based on these preliminary simulations.

Finally, two comprehensive simulations are conducted, allowing all structural elements to deform. These include a head-on impact at the fender structure's tip and an oblique impact at its side. A detailed configuration of these simulations, along with their results, is provided in chapter 6.

3.3 THE FINITE ELEMENT ANALYSIS APPROACH

To perform the simulations described in section 3.2, an established finite element (FE) software is required. The software should be able to account for both material- and geometrical nonlinearities. This because specifically for the head-on impact scenario, large deformations in combination with plastic material behavior are expected beforehand performing the analysis. One of the generally used software packages in engineering to design and/or predict structural behavior under dynamic loading conditions is LS-DYNA. The FE models in this thesis are developed in LS-DYNA 2024 R2 [22]. This FE software utilizes a numerical explicit method while solving the model which is an efficient and robust method while processing transient dynamic processes with a short time duration. Unlike quasi-static analysis, transient dynamics also takes into account the inertial effects whereas in quasi-static it is assumed that this is negligible. Furthermore, LS-DYNA provides the option to define a fracture criterion into the material models. By doing this, the software is able to simulate damage behavior by eliminating elements out of the model during the analysis.

To begin with, the required geometries are modeled and pre-processed to meet the requirements to perform a proper analysis. This has been done using the SpaceClaim module integrated in the ANSYS 2024 R2 software package [23]. Furthermore, the material model that best fits the material behavior of the element of interest need to be defined inside the software. Additionally, the geometry needs to be discretized. This is also referred to as meshing. The last step before running the simulation is to set-up the analysis by specifying the boundary- and initial conditions. Furthermore, analysis settings for the simulations must be defined. For example: time step size, hourglass control, contacts, etc. Once this steps have been completed, simulations can be performed. Data generated during the simulations will then be used for post-processing.

Detailed information about the geometry, materials, and meshing is given in chapter 4. Simulation configurations and post-processing of model results are included in chapter 6.

3.4 INITIAL KINETIC ENERGY

The mass of the ship and its initial sailing velocity (v) determine the initial kinetic energy ($E_{k,0}$) introduced into the non-linear finite element model. The mass of the ship is enlarged by an added mass to account

for hydrodynamic effects of the surrounding fluid. This added mass varies between head-on and oblique collision scenarios [24]. Table 3.4 presents the calculation of the initial kinetic energy for both scenarios. The equivalent total mass (G), also referred to as displacement tonnage, is obtained by multiplying the mass of the ship by the hydrodynamic mass factor. The final row of the table displays the values of initial kinetic energy derived using (3.1).

$$E_{k,0} = \frac{1}{2} \cdot G \cdot v^2 \tag{3.1}$$

Table 3.4: Initial kinetic energy

Parameter	Head-on	Oblique	Unit
Ship mass	1840	1840	tonne
Hydrodynamic mass factor	1.1	1.5	-
Equivalent total mass	2024	2760	tonne
Initial sailing velocity	3.0	3.0	m/s
Initial kinetic energy	9.11	12.42	MJ

4

Development non-linear finite element model

This chapter provides a description of the non-linear finite element (NLFE) models used in this study. To begin with, a consistent unit system is adopted and applied throughout the impact simulations. The geometries of the ship structure and fender structure are described, followed by the specification of model boundary conditions. Additionally, the material model for steel components is outlined. Finally, general solver settings used to solve the models are discussed.

4.1 CONSISTENT UNITS

LS-DYNA [22] recommends using a specific consistent unit system to ensure accuracy: SI Nmm. Throughout this thesis the SI Nmm unit system is applied.

4.2 GEOMETRY MODELLING

The first step in developing the NLFE model is setting up the model geometries. The geometry of the fender structure is fully modeled in 3D using surface elements based on the technical drawings. Figure 4.1a shows the upper part of the fender structure. The geometry of the ship structure is extracted from the model input files from B. Meijer's thesis work [4]. Similarly to the fender structure, the geometry of the ship is modeled in 3D using surface elements. Figure 4.1b presents a visualization of both the inner and outer geometry of the ship's bow structure. Detailed information about model geometries and element thicknesses is provided in appendix B.

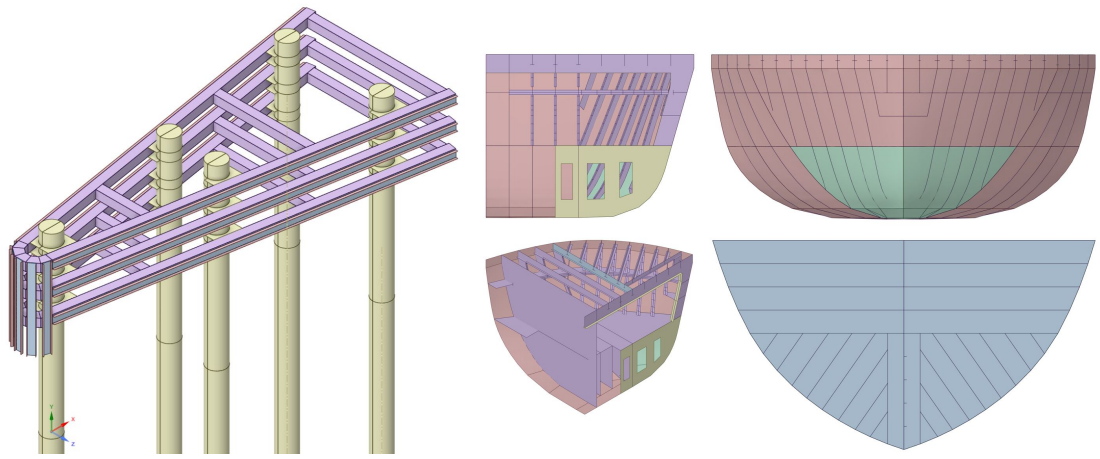

(a) Fender structure **(b)** Ship structure

Figure 4.1: Geometries non-linear finite element models

4.3 BOUNDARY CONDITIONS

This section outlines the boundary conditions applied to the non-linear finite element models. First, the boundary conditions related to the fender-soil system are discussed in section 4.3.1, followed by a description of the boundary conditions for the sailing ship in section 4.3.2.

4.3.1 Soil Structure Interaction

The piles of the fender structure are constrained horizontally by the surrounding soil. As discussed in chapter 2, the soil can be modeled using a series of springs distributed around the pile's circumference. In the finite element model, a spring is attached in the radial direction at every mesh node where the pile is embedded in the soil. Depending on the position of each spring, a linear or non-linear force-displacement curve can be assigned. Additionally, the springs are uncoupled and act independently of one another. Since discrete springs are modeled at every mesh node where soil interacts with the pile, the number of springs depends on the chosen mesh size for the piles in the fender structure. Vertically, the piles are simply supported at their base (foot). Figure 4.2 illustrates how soil springs are incorporated into the LS-DYNA model, with four distinct soil layers represented by different colors.

With the inclusion of soil springs and vertical supports at the base of the piles, the fender structure is constrained in both horizontal and vertical planes. No additional boundary conditions are required to maintain structural stability, provided resistance values are not exceeded.

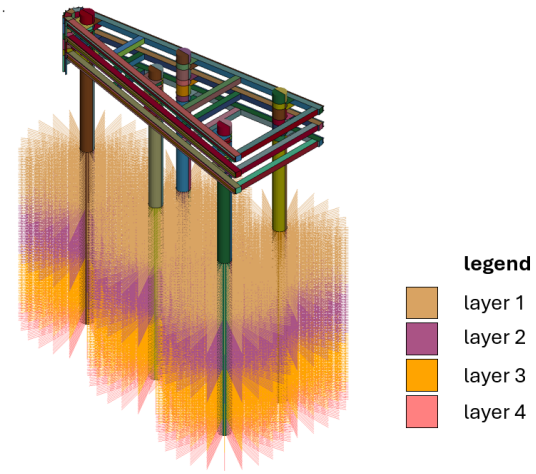

Figure 4.2: Model of soil-structure interaction

The discrete springs are modeled using the `*ELEMENT_DISCRETE` keyword [25], in combination with the `*MAT_SPRING_INELASTIC` keyword [26]. This combination allows for a discrete input of the load-displacement behavior of the springs. Furthermore, the springs are modeled as compression-only types, consistent with the transformation from uni- to multi-directional springs.

4.3.2 Sailing Ship

The ship structure is a moving object during the simulations. Since two different impact scenarios are evaluated, two distinct boundary conditions are formulated.

Scenario 1: head-on impact
In this scenario, a remote point is modeled at the section where the ship structure is no longer explicitly represented. This remote point is rigidly connected to the outermost edges of the bow structure. The boundary conditions for the sailing ship are defined at this remote point. For head-on impact simulations, all rotational degrees of freedom are fixed. Additionally, translations are restricted except for the surging

motion of the ship. Figure 4.3 illustrates how the remote point is implemented in the simulation software. This remote point also serves as the location for modeling a point mass that represents the portion of the ship not included in the model.

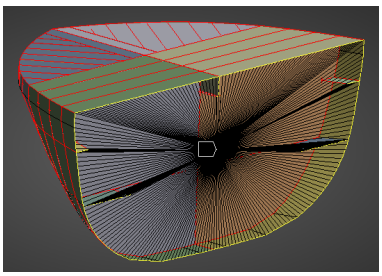

Figure 4.3: Head-on impact: remote point attachment

Scenario 2: oblique impact
For the oblique impact scenario, the remote point is positioned at the mid-length of the ship, which is assumed to represent the ship's center of mass. Similar to the head-on impact scenario, the boundary condition is defined at the location of the remote point. For this scenario, yawing, surging, and swaying motions are permitted, while all other rotational and translational degrees of freedom are fixed. Figure 4.4 illustrates how the remote point is implemented in the simulation software.

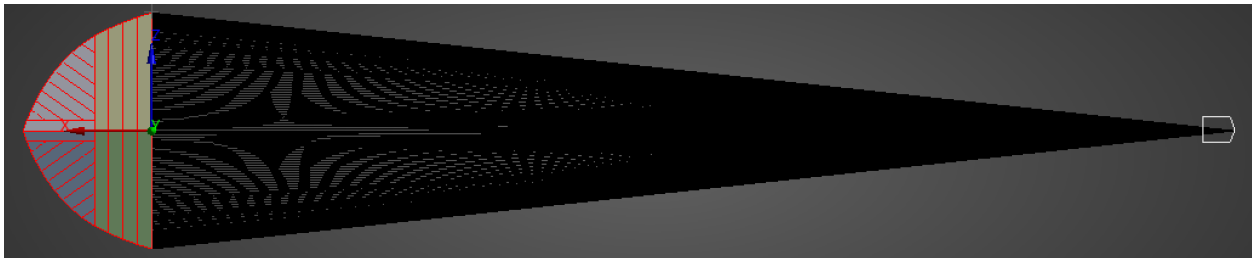

Figure 4.4: Oblique impact: remote point attachment

A point mass is attached to the remote point, representing the portion of the ship not included in the model. Not all rotational degrees of freedom are fixed during the oblique impact. Therefore, a mass moment of inertia is defined in the direction of the ship's yawing axis. By doing this, the following assumptions are made:

- The center of mass is located at the mid-length of the ship;
- The mass of the ship is evenly distributed along its length;
- Hydrodynamic effects may be neglected with respect to yawing motion of the ship.

Under these assumptions, the mass moment of inertia can be approximated using the moment of inertia formula for a uniform rod, as shown in (4.1):

$$I_{\text{yawing}} = \frac{1}{12} \cdot M \cdot L^2 \tag{4.1}$$

Where:
M = total mass of the ship
L = total length of the ship

4.4 STEEL MATERIAL MODELS

The material models for the structural steels in the NLFE model are partly derived based on the method described in section 2.4 following the DNV-RP C208 [20].

The DNV-RP C208 does not specify an end point for the true stress-strain curve. Ultimate tensile stress (σ_{ult}) and tensile fracture strain criterion (ε_{fr}) are taken from idealized material curves specified in the European standard NEN-EN 10025-2 [27]. This standard describes the technical delivery conditions for structural steels and can be considered as representing the lower fractile limit of structural steel properties.

In this thesis, a simplification is made at the final part of the material model. Therefore, a modified true stress-strain curve is adopted as schematized in figure 4.5. The modified material model follows the recommended curve from the DNV-RP C208 until the ultimate tensile stress is reached. From this point a linear part is modeled until the tensile fracture strain criterion is reached.

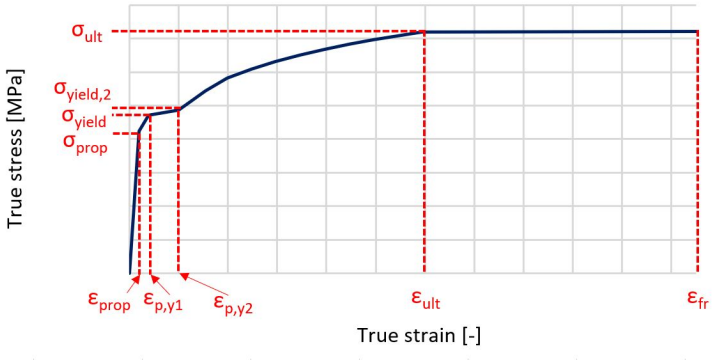

Figure 4.5: Modified true stress-strain curve

4.4.1 Modified true stress-strain curves

In the DNV-RP C208 and the NEN-EN 10025-2, material properties are differentiated based on thickness, resulting in multiple stress-strain relationships within the same structural steel quality class. The following paragraphs discuss the material models used for the ship structure and the fender structure.

In shipbuilding, a different material classification system is used. The ship model included in this research is classified as Grade A steel, which has material properties comparable to structural steel class S235. Therefore, S235 material properties are adopted. The thickness of the ship's structural elements ranges from 8 to 16 mm, allowing for representation by a single material model. Figure 4.6a visualizes the modified true stress-strain relationship for the ship structure.

For the fender structure, a higher material quality is applied. With element thicknesses ranging from 10 to 20 mm and steel quality S355, two stress-strain curves are obtained. Figure 4.6b compares the two curves.

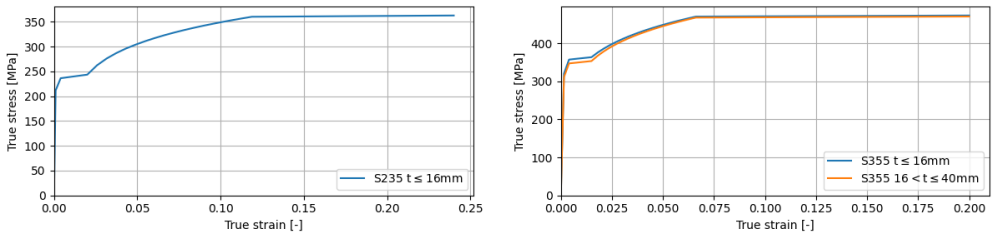

(a) S235 **(b)** S355

Figure 4.6: True stress-strain relation

The material models are implemented into the NLFE model using the `*MAT_PIECEWISE _LINEAR _PLASTICITY` keyword in LS-DYNA [26]. This material model is commonly used for metallic materials in explicit analyses and allows for detailed input of stress-strain relationships, including multiple linear

hardening segments. Numerical derivations of the material properties and the corresponding material cards are provided in Appendix D.

4.5 GENERAL SOLVER SETTINGS

In this section, general solver settings are provided. To obtain numerical stable results, time step size must be chosen carefully. Furthermore, element formulation are provided, hourglass control algorithm is discussed, and the contact definition is elaborated.

4.5.1 Time Step

As mentioned earlier LS-DYNA employs an explicit time integration scheme for solving the problem. However, explicit solvers require a stability condition to ensure accurate end numerical stable solutions. One commonly used criterion for the approximation of the initial time step is the Courant-Friedrichs-Lewy (CFL) criterion, which defines a upper bound for the allowable time step. This condition is based on the theory that a stress wave may not travel through an entire finite element within a single time step. Mathematically, the critical time step is given by (4.2).

$$\Delta t \leq \frac{L}{c} \tag{4.2}$$

Where:
L is the characteristic length of the smallest element in the mesh.
c is the wave speed in the material

The wave speed is dependent to the Young's modulus (E) and the density (ρ) of the material, and can be calculated using (4.3).

$$c = \sqrt{\frac{E}{\rho}} \tag{4.3}$$

From (4.3) it can be seen that an increase in the material density results into a lower wave speed. If the wave speed becomes smaller the critical time step becomes larger. Artificially increasing the density (mass) of elements in the model, known as mass scaling, can reduce computational time by increasing the critical time step. However, adding mass to a dynamic system can alter the physics of the problem. Therefore, no mass scaling is applied during this research. As a result, no special caution need to be taken with respect to automatic mass scaling during the simulations.

4.5.2 Finite Element Formulation

The geometry of the ship and fender structure are completely modeled using surface elements. Therefore, all structural elements are modeled as shell elements in the NLFE model. There are different shell formulations available in LS-DYNA [25], three commonly used formulations are:

- Hughes-Liu (ELFORM=1)
- Belytschko-Lin-Tsay (ELFORM=2)
- Fully-integrated shell element (ELFORM=16)

Hughes-Liu shell element formulation is proven to be well suited for NLFE analysis. It has been shown that this formulation type is able to accurately approximate the response when large stains and rotation effects are involved [28]. Furthermore, the Hughes-Liu formulation can make use of one-point integration to increase computational efficiency. However, attention should be taken to the development of zero energy modes in the response.

Belytschko-Lin-Tsay is an extremely effective element formulation compared to the other formulations.

According to [29], the Hughes-Liu has a processing time more than twice as long compared to this Belytschko-Lin-Tsay formulation. This formulation type can also make use of one-point integration and is therefore also sensitive to the development of zero energy modes. However, the increase in computational efficiency comes with a cost in solution accuracy. Especially, for large deformation responses this element formulation is less accurate compared to Hughes-Liu or fully integrated elements [30]

Fully-integrated shell elements make use of 2x2 normal integration in LS-DYNA. As a result, the number of equations to solve for increases when applying fully-integrated elements. Therefore, this formulation results in the highest computational time for the compared cases. An advantage is that development of zero energy modes is prohibited. Nonetheless, fully integrated elements tends element to "lock" [28]. This results in an overestimation of the stiffness matrix and could lead in underestimation of the response when large deformations occur.

Taking the advantages and disadvantages into comparison leads to the decision to globally make use of the Hughes-Liu formulation. A computational strategy is described in the next section with respect to zero energy modes.

4.5.3 Hourglass Control

In finite elements hourglass modes can occur when using under intergrated elements. Hourglass modes are nonphysical modes of deformation. LS-DYNA has the option to avoid or minimize the amount of hourglass modes by using hourglass control algorithms. Those algorithms introduce internal nodal forces to counteract hourglass modes.

There are two different forms of hourglass control: stiffness and viscous forms. Viscous forms are best applicable to problems that involve high velocity/strain rate while stiffness forms are preferred for lower rate problems, including crash simulations. As a rule of thumb the hourglass energy should not exceed 10 percent of the internal energy. This must hold for the whole system as for individual parts. In the analysis performed in this research a stiffness form for shell elements is used which is also referred to as Flanagan-Belytschko. This has be done using the LS-DYNA keyword `*CONTROL_HOURGLASS` [25] with hourglass control type IHQ = 4.

Element formulation may be switched to fully-integrated elements locally in case the condition related to the allowable hourglass energy cannot be satisfied in the model.

4.5.4 Contact Definition

In LS-DYNA, contact modeling plays a crucial role in accurately capturing interactions between bodies in impact simulations. The software implements sophisticated contact algorithms that detect and resolve interactions between elements to prevent penetration and ensure realistic force transmission [22].

Contact modelling makes it possible for unmerged Lagrangian elements to interact. Possible interactions are segments that: impact, slide, push, or rub against each other. In LS-DYNA it is possible to automatically detect and generate contacts between bodies using the `*CONTACT_AUTOMATIC_SINGLE_SURFACE` keyword [25].

This automatic contact algorithm is a penalty-based contact formulation. This means that a finite stiffness is calculated at both interacting segments that is used to prevent penetration between interacting segments. In contact formulation between two segments, one is called the master and the other is called the slave segment. Once the slave segment penetrates the master segment, a "penalty" force based on the calculated contact stiffness is applied to the slave segment to project it back onto the master segment. In addition, reaction forces are applied on the master segment to keep equilibrium of forces. In other words, the total force on the master segment must equal the penalty force applied to the slave segment.

Alternatively, segments can be tied together to constrain individual translation between segments while allowing for disparate mesh sizes. This type of contact can be defined using the `*CONTACT_TIED_NODES _TO _SURFACE _OFFSET` keyword, which enforces compatibility between interacting surfaces by restricting relative movement.

5

Development Simplified Dynamic Model

This chapter presents the development of the simplified dynamic model. The purpose of the simplified model is to derive the transient response of the fender structure at interest during head-on ship impact conditions without the use computational expensive NLFE simulations.

This chapter describes the simplified model, outlines the modeling assumptions, and explains the solution strategy. Model results are presented and compared with the NLFE model in chapter 6.

5.1 SCHEMATIZATION SIMPLIFIED DYNAMIC MODEL

This section discusses the schematization of the simplified model. To reduce the size and complexity of the model, several assumptions are made during its construction:

- The transient response of the fender structure can be approximated using a linear model for the structural elements.
- Structural elements deform only in the direction perpendicular to their axis.
- The soil is represented by a linear elastic foundation.
- The impacting ship is simplified as a mass-spring system at the point of impact.

Based on these assumptions, a two-dimesnional (2D) frame structure is constructed, as shown in figure 5.1. Reflecting the geometry of the actual fender structure, the simplified model includes two different cross-sections. Cross-sectional properties (ρA and EI) for the piles are subscripted by a letter "p", and those for the crossbeams with "b". Soil layering is modeled using a stepped linear elastic foundation with stiffness values k_{Li}, where "i" denotes the index of the soil layer.

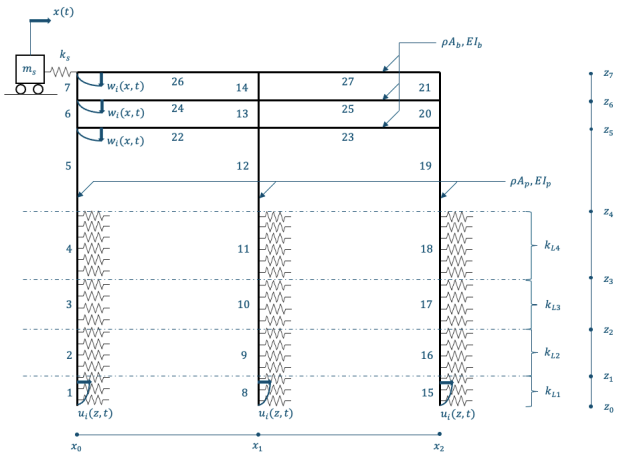

Figure 5.1: Simplified dynamic model

5.2 ELEMENT FORMULATIONS

To perform a dynamic analysis, the structural elements of the frame structure are formulated using Euler-Bernoulli beam theory. This results in a set of partial differential equations (PDEs). Beginning with the piles embedded in the soil ($z_0 \leq z < z_4$). Equation (5.1) presents the PDE for a continuous beam on an elastic foundation.

$$EI_p \frac{\partial^4 u_i(z,t)}{\partial z^4} + \rho A_p \frac{\partial^2 u_i(z,t)}{\partial t^2} + k_{Li} u_i(z,t) = 0 \tag{5.1}$$

Where:
E is the Young's modulus
I is the moment of inertia
ρ is the density
A is the section area
k_{Li} is the stiffness of the linear elastic foundation
u is horizontal displacement pile
t is time
z, x are spatial coordinate

For the piles extending above the soil surface ($z_4 \leq z \leq z_7$), the elastic foundation term is omitted, leading to (5.2)

$$EI_p \frac{\partial^4 u_i(z,t)}{\partial z^4} + \rho A_p \frac{\partial^2 u_i(z,t)}{\partial t^2} = 0 \tag{5.2}$$

A similar form of the equation applies to the crossbeams ($x_0 \leq x \leq x_2$), as shown in (5.3).

$$EI_b \frac{\partial^4 w_i(x,t)}{\partial z^4} + \rho A_b \frac{\partial^2 w_i(x,t)}{\partial t^2} = 0 \tag{5.3}$$

Where:
w is vertical displacement beam

The equation of motion for the mass-spring system is given in (5.4). Note that this equation does not yet include coupling with the frame structure.

$$m_s \frac{d^2 x(t)}{dt^2} + k_s x(t) = 0 \tag{5.4}$$

Where:
m_s is the ship's mass
k_s is the spring stiffness
$x(t)$ is the horizontal displacement of the mass

5.3 MODAL ANALYSIS

Modal analysis is widely used technique for studying the dynamic behavior of structures, particularly under the assumption of linear elasticity. Since the system includes Euler-Bernoulli beams whose governing equations of motion are linear partial differential equations, modal analysis can be employed to obtain the transient response of the system. Modal analysis is based on the principle that, for linear systems, the transient response can be expressed as a summation of spatial mode shapes multiplied by time-dependent modal amplitudes. Equation (5.5) provides a general mathematical expression for the transient response of the piles. A similar formulation applies to the crossbeams. In this equation, $u_i(z,t)$ represents the transient response, $\phi_n(z)$ are the mode shapes obtained from a free vibration analysis, and $q_n(t)$ are the generalized coordinates (modal amplitudes).

$$u_i(x,t) = \sum_{n=1}^{\infty} \phi_n(z) q_n(t) \tag{5.5}$$

To perform the modal analysis, the method of separation of variables is applied by assuming a solution of the form:

$$u(z,t) = \phi(z) q(t) \tag{5.6}$$

Substituting the assumed solution (5.6) into the previously derived PDE (5.2) yield:

$$EI \frac{\phi^{(4)}(z)}{\phi(z)} = -\rho A \frac{\ddot{q}(t)}{q(t)} = \lambda \tag{5.7}$$

Here, λ is the separation constant introduced in (5.7). This substitution results in two ordinary differential equations (ODEs), where the spatial component is given in (5.8) and the time-dependent component in (5.9). By introducing the variable β and rewriting the system, the following two equations are obtained:

$$\phi^{(4)}(z) - \beta^4 \phi(z) = 0, \quad \text{with } \beta^4 = \frac{\rho A \omega^2}{EI} \tag{5.8}$$

$$\ddot{q}(t) + \omega^2 q(t) = 0 \tag{5.9}$$

The same procedure can be applied to the PDE for a pile on an elastic foundation (5.1). resulting in the following expression for β:

$$\beta^4 = \frac{\rho A \omega^2}{EI} - \frac{k_{Li}}{EI} \tag{5.10}$$

5.3.1 Free Vibration Modes

Solving the eigenvalue problem from (5.8) yiels the free vibration modes and corresponding natural frequencies (ω) of the system. The solution to this ODE can be expressed in the following form:

$$\phi(z) = C_1 \cosh(\beta z) + C_2 \sinh(\beta z) + C_3 \cos(\beta z) + C_4 \sin(\beta z) \tag{5.11}$$

Here, C_1, C_2, C_3, and C_4 are constants determined by the boundary conditions of the corresponding beam segment. These boundary conditions arise from continuity between beam segments and the support conditions. Written out boundary conditions are provided in appendix E.

5.3.2 Generalized Coordinates

The mode shapes obrained from the free vibration analysis do not account for external forces acting on the structure. The coupling between the frame structure and the mass-spring system introduces constraints, making it a constrained structure [31].

For any one-directional structure subjected to a distributed force (force per unit length), and for which the normal modes and natural frequencies are known, the deflection at any point and time can be expressed using (5.5). At this stage, the mode shapes $\phi_n(z)$ are known, and the generalized coordinates $q_n(t)$ must be solved to obtain the transient response of the structure. When an external force is present, it can be shown that (5.12) must be satisfied [31].

$$\ddot{q}_n(t) + \omega_n^2 q_n(t) = \frac{1}{M_n} \int f(z,t) \phi_n(z) dz \tag{5.12}$$

Where:

M_n is the modal mass for mode n
$f(z,t)$ is the space and time dependent external force

5.3.3 Coupling with mass-spring system

The coupling between the frame structure and the mass-spring system can be represented as an external load acting on the frame structure. In general, for concentrated loads on structures (5.12) can be rewritten into the following form:

$$\ddot{q}_n(t) + \omega_n^2 q_n(t) = \frac{1}{M_n} F(a,t)\phi_n(a) \tag{5.13}$$

To derive an expression for $F(a,t)$, the displacement method is employed. Figure 5.2 illustrates the method. In figure 5.2a, a zoomed-in view of the system without displacements is shown. Note that the mass-spring system is coupled at the end of the beam in the frame structure. Therefore, other elements are omitted in the figures for clarity. Figure 5.2b depicts the case where the mass (m_s) undergoes a positive displacement, with forces acting on the mass and the beam highlighted in red. Figure 5.2c shows the situation for a positive displacement of the beam's end.

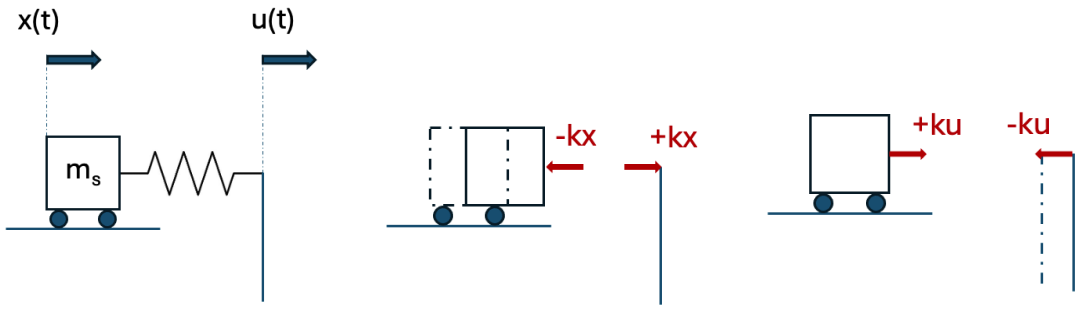

(a) No displacement **(b)** Mass displacement **(c)** Beam displacement

Figure 5.2: Displacement method

In (5.13), the position where the external force acts on the structure is denoted by a. From figure 5.1, it is known that $a = z_7$. Using the displacement method, an expression for $F(z_7,t)$ is obtained.

$$F(z_7,t) = k_s \cdot x(t) - k_s \cdot u(z_7,t) \tag{5.14}$$

By applying the modal superposition principle, the displacement $u(z_7,t)$ can be replaced by the expression given in (5.15).

$$u(z_7,t) = \sum_{i=1}^{\infty} \phi_i(z_7) \cdot q_i(t) \tag{5.15}$$

Substitution of (5.15) into the previously derived relation for the concentrated force (5.14) yields the following equation for the concentrated load on the frame structure:

$$F(z_7,t) = k_s \cdot x(t) - k_s \cdot \sum_{i=1}^{\infty} \phi_i(z_7) \cdot q_i(t) \tag{5.16}$$

The same concentrated force, but with opposite sign, acts on the mass. This results in two coupled ODEs: one describing the frame structure and the other the mass-spring system, coupled through the concentrated force function. Coupled equations are given in (5.17).

$$\begin{cases} \ddot{q}_n(t) + \omega_n^2 \cdot q_n(t) = \dfrac{1}{M_n} \cdot F(z_7,t) \cdot \phi_n(z_7) \\ m_s \cdot \ddot{x}(t) = -F(z_7,t) \end{cases} \tag{5.17}$$

The mass-spring system is included to approximate the impact loading of the ship. However, physically, this spring coupling is not present. A more realistic approach is to define the spring coupling as compression-only as expressed in (5.18).

$$F(z_7,t) = \begin{cases} k_s \cdot x(t) - k_s \cdot \sum_{i=1}^{\infty} \phi_i(z_7) \cdot q_i(t), & \text{if} \quad x(t) > u(z_7,t) \\ 0, & \text{if} \quad x(t) < u(z_7,t) \end{cases} \tag{5.18}$$

Combining (5.18) with the previously obtained system of ODEs (5.17) results in the final set of equations. Two equations with two unknowns ($x(t)$ and $q_n(t)$) that can be solved simultaneously. Transforming these into a system of first-order ODEs makes the problem compatible with SciPy's `solve_IVP` solver, which employs the RK45 time integration method [32]. Therefore, two auxiliary variables, p_n and v, are introduced as shown in (5.19).

$$\begin{cases} \dot{q}_n = p_n \\ \dot{p_n} = -\omega_n^2 \cdot q_n(t) + \dfrac{1}{M_n} \cdot \phi_n(z_7) \cdot F(z_7,t) \\ \dot{x} = v \\ \dot{v} = \dfrac{1}{m_s} \cdot (-1) \cdot F(z_7,t) \end{cases} \tag{5.19}$$

6

Results and Discussion

First, the transient response of the head-on impact scenario is obtained using the simplified dynamic model. Then, the effect of the model input parameters on the structural behavior under impact loading is studied. By doing this, potential sensitivities of the separate NLFE models are addressed. This is followed by a presentation of the simulation results for both the head-on and oblique impact scenarios, including the flexibility of all models simultaneously. Finally, a comparison is made between the simplified and the NLFE models, as well as a comparison between the NLFE model and the Dutch codes.

During the analysis of the results, references are made to both the global level and the model level. When analyzing at global level, the unity of the whole system is discussed, which is represented by the enclosing ellipse in figure 6.1. When analyzing individual parts, this will be referred to as model level. Figure 6.1, shows the individual models using green tiles.

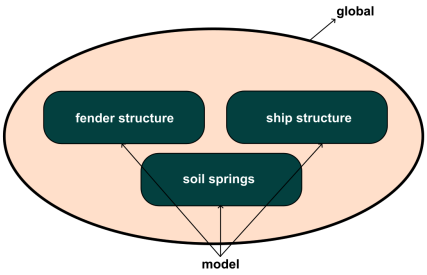

Figure 6.1: Definitions NLFE simulations

6.1 RESULTS SIMPLIFIED MODEL

In this section, the transient response for the head-on impact scenario is derived using the simplified dynamic model. A description of the simplified model can be found in chapter 5.

6.1.1 Model Input

Values for the spatial coordinates of the frame structure are provided in table 6.1. Pile distances are equivalent to those in the NLFE model. Crossbeams are positioned at the height of the centerline in the NLFE model.

Table 6.1: coordinate data [m]

z_0	z_1	z_2	z_3	z_4	z_5	z_6	z_7
0.0	1.0	4.0	7.0	10.5	16.2	17.2	18.1
x_0	x_1	x_2					
0.0	5.9	11.8					

Cross-sectional properties are based on the design of the fender structure of interest. Normalized values for the Young's modulus and density of structural steel are used. Stiffness values for the elastic foundation are based on the modulus of horizontal subgrade reaction from the API-method. Numerical values for the model input parameters are presented in table 6.2.

Table 6.2: Simplified model: input parameters

Parameter	Value	Unit
E	$2.1 \cdot 10^{11}$	Pa
ρ	7850	kg/m^3
A_p	$4.66 \cdot 10^{-2}$	m^2
A_b	$2.14 \cdot 10^{-2}$	m^2
I_p	$3.21 \cdot 10^{-3}$	m^4
I_b	$3.98 \cdot 10^{-4}$	m^4
k_{L1}	$1.26 \cdot 10^{7}$	N/m/m
k_{L2}	$5.82 \cdot 10^{6}$	N/m/m
k_{L3}	$1.01 \cdot 10^{7}$	N/m/m
k_{L4}	$1.01 \cdot 10^{7}$	N/m/m

6.1.2 Free Vibration Modes

A free vibration analysis is performed on the structure of interest. The resulting mode shapes and natural frequencies are provided in figure 6.2. Only the first ten mode shapes found are shown. The mode shapes are mass-normalized and scaled for visualization purpose to increase readability. Furthermore, orthogonality is checked, and the resulting mode shapes are found to be perfectly orthogonal.

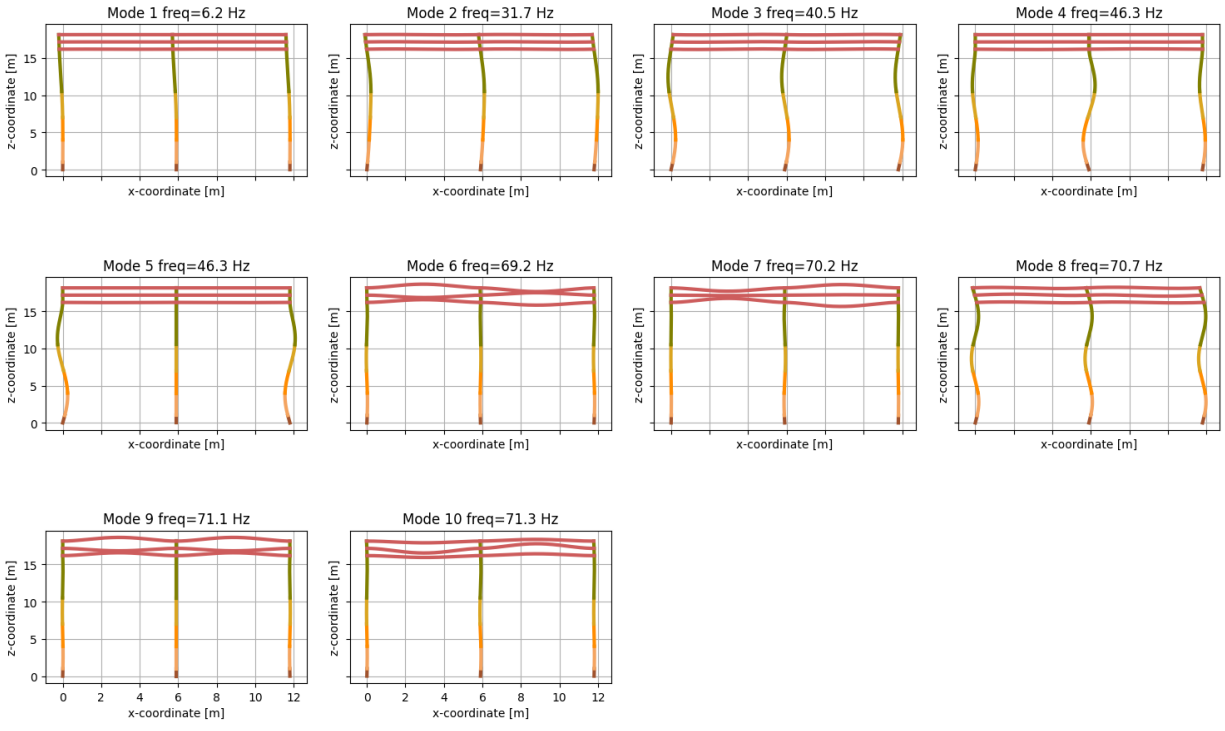

Figure 6.2: First 10 mode shapes with natural frequencies

Verification of free vibration modes

A free vibration analysis is also performed using numerical finite element software. In this analysis, the same frame structure with the same properties is used. Resulting natural frequencies are presented in the

second column of table 6.3. Additionally, the natural frequencies derived using the simplified model are listed in the third column. The final column presents the absolute relative error between the two analysis.

Table 6.3: Verification free vibration modes

mode	numerical ω_n	simplified model ω_n	absolute relative error [%]
1	6.1	6.2	1.6
2	31.4	31.7	0.9
3	39.9	40.5	1.5
4	42.1	46.3	9.1
5	43.1	46.3	6.9
6	62.9	69.2	9.1
7	64.4	70.2	8.3
8	65.2	70.7	7.8
9	66.2	71.1	6.9
10	66.7	71.3	6.5

The values obtained from the simplified model closely match those from the numerical software, especially for the first three natural frequencies, where the difference is smaller than 2%.For the higher-order modes, the results start to deviate between 6% and 10%. Based on this, it is concluded that the system of equations for the simplified model is constructed and solved correctly and can be used to solve for the transient response.

6.1.3 Transient response

The transient response is derived by solving the system of first-order ODEs for the mass displacement ($x(t)$) and the generalized coordinate ($q(t)$). Before solving this problem, the properties of the mass-spring system and initial conditions must be specified. The frame structure is initially at rest and therefore has zero initial conditions throughout. For the mass-spring system, a zero initial displacement is defined. The initial velocity is nonzero and equals the initial velocity of the sailing ship (v_0). The mathematical expressions are presented in (6.1).

$$\begin{aligned} q_n(0) = 0, \quad \dot{q}_n(0) = 0 \\ x(0) = 0, \quad \dot{x}(0) = v_0 \end{aligned} \tag{6.1}$$

The properties of the mass-spring system are shown in table 6.4, which lists the numerical values for the mass (m_s) and the spring stiffness (k_s). The initial velocity of the mass-spring system is provided in the last row of the table.

Table 6.4: Properties mass-spring system

Parameter	Value	Unit
m_s	$2024 \cdot 10^3 \cdot 3/5$	kg
k_s	$16.0 \cdot 10^6$	N/m
v_0	3.0	m/s

To account for the fact that the simplified model is defined only in 2D space, the discrete mass (m_s) is multiplied by a factor 3/5. This factor is based on the ratio of the number of piles included in the fender structure. In 3D, the structure consists of 5 piles in total, whereas the simplified model includes only 3 piles. Dividing the number of piles in the simplified model by the total number of piles in the 3D case yields the reduction factor for the discrete mass.

Mass is a linear scalar in the equation for initial kinetic energy. Therefore, scaling down by a factor of 3/5 reduces the initial kinetic energy by a factor of $1 - 3/5 = 2/5$. It is assumed that this scalar adjustment enables meaningful comparison between the simplified model and the detailed NLFE model.

Displacements

The transient response of the frame structure at discrete moments in time is presented in figure 6.3. The frame structure is initially at rest, as expected from the initial conditions. The mass-spring system, however, has a non-zero initial velocity and starts translating from the first time step. This results in lateral displacements of the frame structure at time steps t = 0.50s and t = 1.00s. At the final two time steps (t = 1.50s and t = 2.00s), the fender structure is vibrating with small displacements around its initial state.

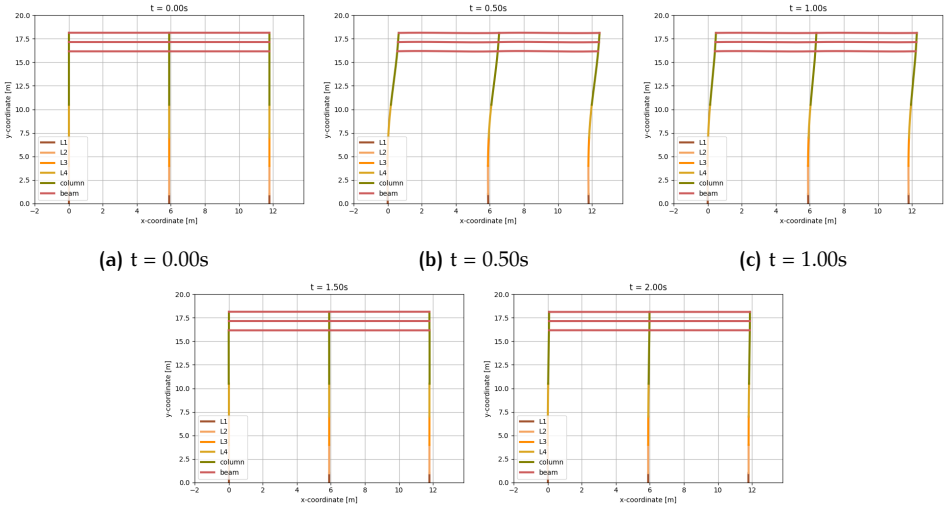

(a) t = 0.00s **(b)** t = 0.50s **(c)** t = 1.00s

(d) t = 1.50s **(e)** t = 2.00s

Figure 6.3: Simplified model: transient response frame structure

The coupled behavior between the frame structure and the mass-spring system is examined in more detail in Figure 6.4, which shows the lateral displacement of the upper left corner of the frame structure ($u_7(z_7, t)$) and the translation of the discrete mass ($x(t)$) over time. A second scenario is included in the graph, in which the spring stiffness (k_s) of the mass-spring system is multiplied by a factor 100. As a result, the spring is tends to behave more like a rigid link that is only activated in compression, representing an impact scenario where ship deformations are neglected. The compression-only coupling is clearly reflected in the graph. At the time increment when the spring goes into tension, decoupling occurs, and the mass begins moving away from the frame structure. From that point onward, the frame structure continues vibrating in steady-state, as no damping is included in the model.

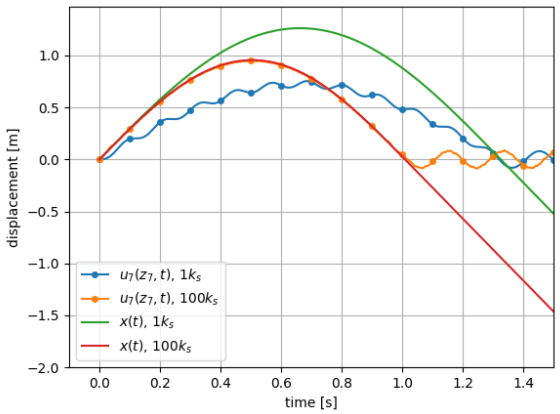

Figure 6.4: Simplified model: peak displacement frame with mass displacement

Table 6.5 summarizes the peak displacements and impact duration for both scenarios. It can bee seen that the largest peak displacement occur in the scenario with a high value of k_s. Furthermore, the longest

impact duration is observed for the scenario with a low value of k_s. For the scenario where $k = 100k_s$, the displacement of the frame structure and the discrete mass closely follow the same path until decoupling occurs. This is consistent with the "rigid link" analogy described above.

Table 6.5: Simplified model: summary results

Parameter	$1k_s$	$100k_s$	Unit
Peak displacement frame structure	0.75	0.95	m
Peak displacement discrete mass	1.26	0.96	m
Impact duration	1.33	1.02	s

6.2 SENSITIVITY ANALYSIS

In this section, the simulation results of the sensitivity analysis are provided and discussed following the same structure as prescribed in section 3.2. Therefore, this section begins with simulation results of the independent models. These simulations are included to first reduce complexity and to gain a better understanding of the structural behavior under impact loading at model level. Additionally, important parameters are studied to address possible sensitivities in the models. Based on the knowledge obtained, a setup is chosen for the final analysis for head-on and oblique impact events.

6.2.1 Mesh Convergence

An important aspect when using (non-linear) finite element methods is selecting an appropriate mesh size. Mesh size greatly influences the accuracy of model results and should be sufficient small to capture local deformations and failure modes. Therefore, a mesh convergence study was performed for both the ship structure and the fender-soil system. The results are provided below.

Mesh convergence: ship structure
Figure 6.5a presents the force displacement graph for mesh sizes: 50, 75, 100, and 150 mm. The force-displacement relations are obtained using a head-on impact configuration with a rigid fender structure. Displacements are measured relative to the reference point shown in figure 6.5b. Force is measured by recording the reaction forces of the rigid fender in the ship's sailing direction and summing them. During all four simulations, only the mesh size was varied. All other input parameters were kept the constant to ensure a proper comparison.

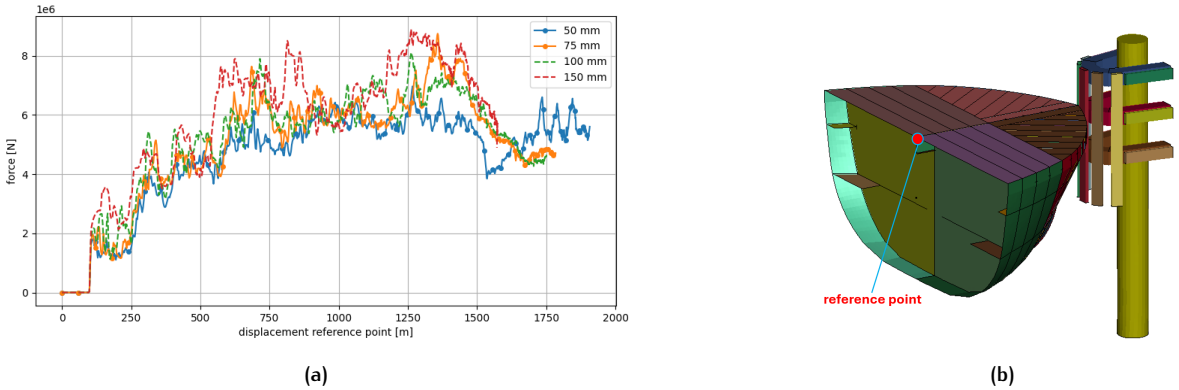

Figure 6.5: Reaction force versus ship displacement w.r.t. reference point over time

As seen in figure 6.5a, convergences has not yet been reached for the complete simulation. Since this model involves a head-on impact with a rigid obstacle, all kinetic energy of the ship is converted into internal energy of the ship structure, leading to large plastic deformations with complex folding patterns. In the final NLFE simulations of this research, the fender structure is not rigid, so bow crushing is expected to

be significantly reduced. Focusing on the small displacement range in figure 6.6, mesh sizes of 50 and 75 mm appear nearly converged.

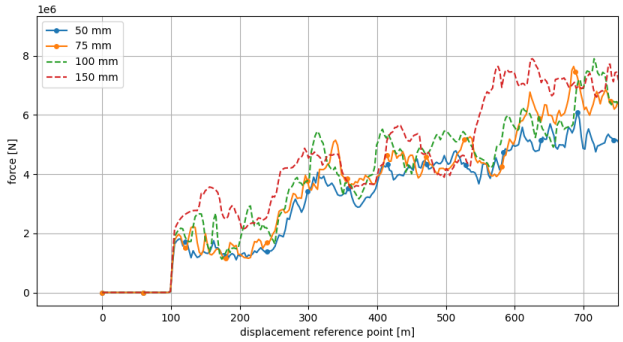

Figure 6.6: Reaction force versus ship displacement w.r.t. reference point over time (zoomed-view)

Another commonly used metric to assess accuracy of numerical simulations is the ratio between the hourglass energy and peak internal energy. For all four mesh sizes, this ratio ranges between 4 and 7%, indicating numerically stable results. None exceed the 10% limit prescribed in section 4.5.3.

Mesh convergence: fender-soil system

A mesh convergence study was also conducted for the piles of the fender structure, including the non-linear soil springs. Only one pile (monopile) was considered, undergoing a forced displacement in a single direction, for two mesh sizes: 50 and 100 mm. Figure 6.7 compares the forced displacement versus the peak Von Mises-stress at the overturning point and the total internal energy of the pile. The overturning point is defined as the cross-section at riverbed level.

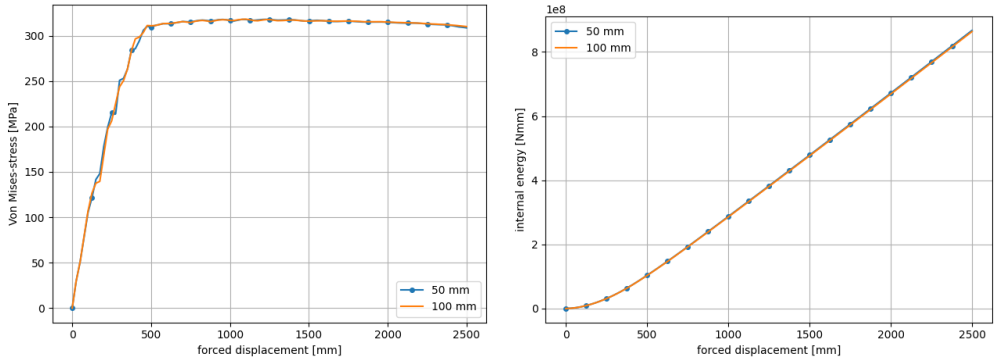

Figure 6.7: Forced displacement versus (a) Von Mises-stress and (b) internal energy

As described in section 4.3.1, the number of soil springs depends on the mesh size applied to the pile. Therefore, a comparison of the resultant total spring force versus the pile head displacement at different soil layers is made, as shown in figure 6.8.

It can be concluded that for both mesh sizes almost the same results are obtained within the steel of the pile. The curves are almost on top of each other for both the Von Mises-stress and the internal energy. Furthermore, the mesh size of the pile seems to have limited effect to the reaction forces at different soil layers. Therefore, statement can be made that the mesh is converged for both sizes included in this study.

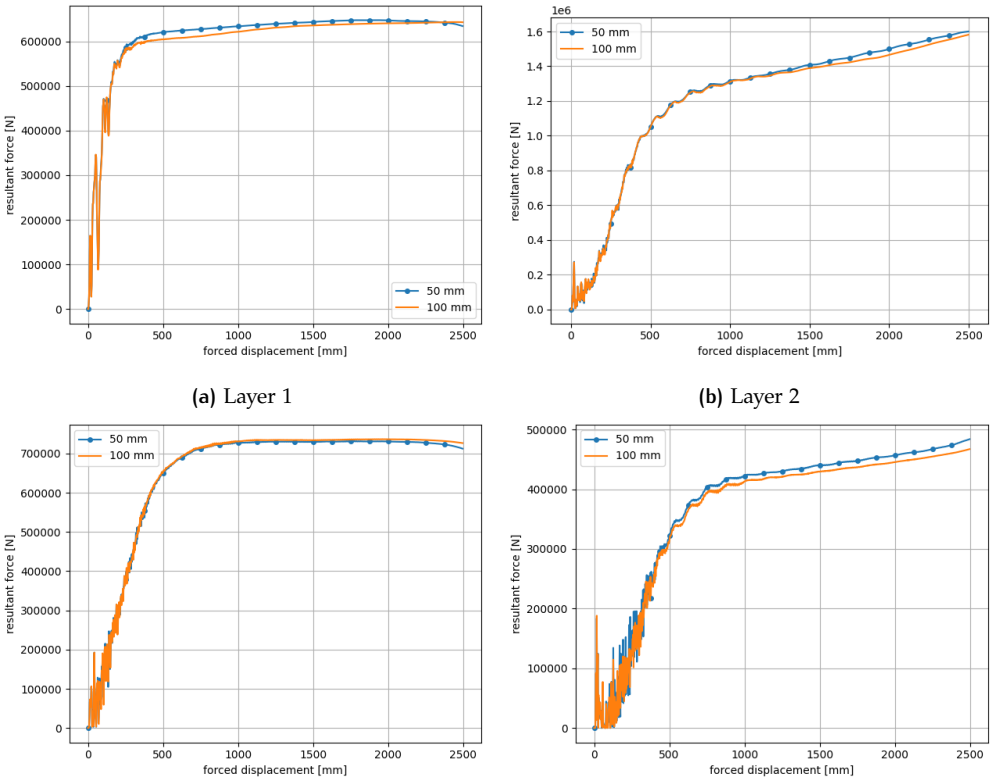

(a) Layer 1

(b) Layer 2

(c) Layer 3

(d) Layer 4

Figure 6.8: Forced displacement versus resultant force soil springs

Conclusion
For the ship structure, a mesh size of 75 mm is selected for the detailed model. For the fender structure, a mesh size of 100 mm is used. While a finer mesh size would improve accuracy, these mesh sizes provide an optimal balance between accuracy and computational cost.

6.2.2 Sensitivity analysis: ship's bow structure

Five simulations were performed to study the structural behavior of the ship's bow during impact loading. Across these simulations, the following input parameters were varied: steel material model (A1, A2), static friction coefficient (B1, B2), and obstacle geometry (C3). Table 6.6 summarizes the numerical results obtained from the non-linear finite element (NLFE) simulations. Visualizations at discrete time steps are provided in appendix F.

Table 6.6: Summary of results flexible ship

	Unit	A1	A2	B1	B2	C1
Obstacle	-	rigid wall	rigid wall	rigid wall	rigid wall	rigid fender
Peak internal energy ship	MJ	7.80	7.73	8.45	8.08	8.00
Peak indentation ship	m	1.17	1.13	1.32	1.08	1.61
Peak impact force	MN	12.96	13.00	10.33	14.68	8.40
Impact duration	s	0.77	0.77	0.95	0.74	> 1

In the paragraphs below, results are discussed group by group, according to the parameter varied.

Group A
Simulations A1 and A2 employ two steel material models. A1 uses the non-linear model described in

Chapter 2. A2 uses a simplified but widely applied bilinear model. Ultimate tensile stress and fracture strain criterion are kept identical as shown in figure 6.9.

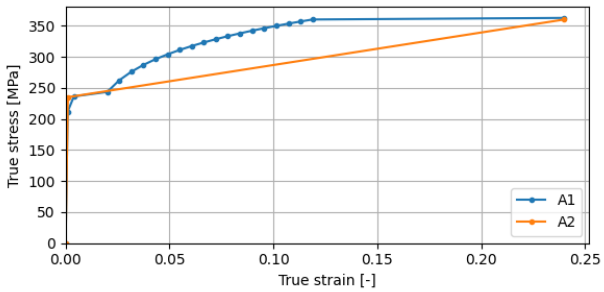

Figure 6.9: Steel material models, A1: non-linear and A2: bi-linear

Table 6.6 shows that peak values are nearly identical. The non-linear model (A1) produces a slightly softer response since a larger indentation depth but a marginally lower peak impact force are observed.

Group B

To assess friction effects, simulation B1 employs a lower static-friction coefficient, while B2 uses a higher value than the reference case A1 (see Table 6.7).

Table 6.7: Static friction coefficients

Simulation	Static friction coefficient
A1	0.3
B1	0.1
B2	0.5

Comparing the results from table 6.6, relations between peak responses and static friction coefficient are visible. Lowering the static friction coefficient increases bow crushing, prolongs impact duration, and reduces the peak impact force. As a result, greater amount of the kinetic energy is converted to internal energy of the ship. The opposite trend is observed for a higher static friction coefficient.

Group C

Simulation C1 replaces the rigid wall (used in A1, A2, B1, B2) with a rigid fender structure whose contact area covers only part of the bow cross-section (Figure 6.10).

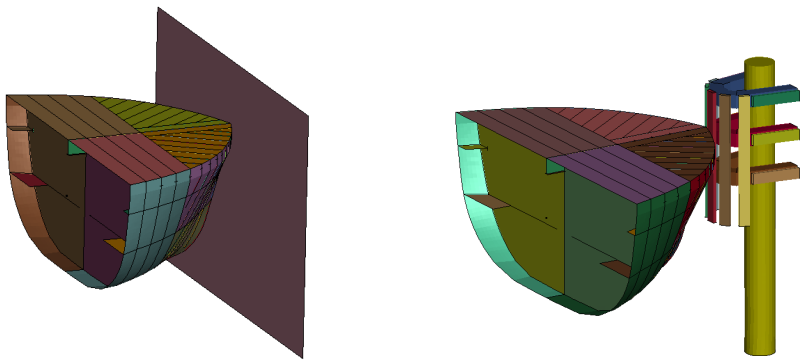

(a) A1 **(b)** C1

Figure 6.10: Type of impacts, A1: rigid wall and C1: rigid fender structure

Compared to the rigid wall, the smaller contact area (C1) activates fewer stiffeners and plates, reducing stiffness. Consequently, impact duration increases, peak forces decrease, and indentation depth rises significantly.

6.2.3 Sensitivity analysis: soil-fender structure (head-on)

Three simulations were performed to examine the structural behavior of the soil-fender system under head-on impact. Parameters varied were the steel material model (D1, D2) and the soil model (E1). Key results are listed in table 6.8, with visualizations in appendix G.

Table 6.8: Summary of results flexible soil-fender structure - Head-on

	Unit	D1	D2	E1
Peak internal energy fender structure	MJ	7.34	7.37	6.88
Peak internal energy soil	MJ	1.49	1.40	1.97
Kinetic energy ship at end	MJ	0.16	0.09	0.09
Peak displacement fender structure	m	2.18	2.14	2.25

Group D
Simulation D1 employs the non-linear steel model. D2 uses a bilinear model. Ultimate tensile stress and fracture criterion are kept identical for both models. In D1, two stress-strain curves are defined to reflect plate-thickness variations.

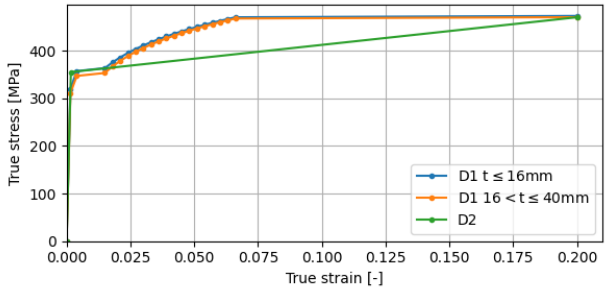

Figure 6.11: Steel material models, D1: non-linear and D2: bi-linear

Table 6.8 shows only minor differences. The non-linear material model (D1) yields a global peak displacement about 40 mm larger than that of the bilinear case (D2).

Group E
Two soil models, introduced in chapter 2, are compared: the API method (D1, reference) and Ménard with Brinch-Hansen (E1). Their multi-directional P–y curves are shown in figure 6.12. Derivations of the P-y curves are provided in appendix C.

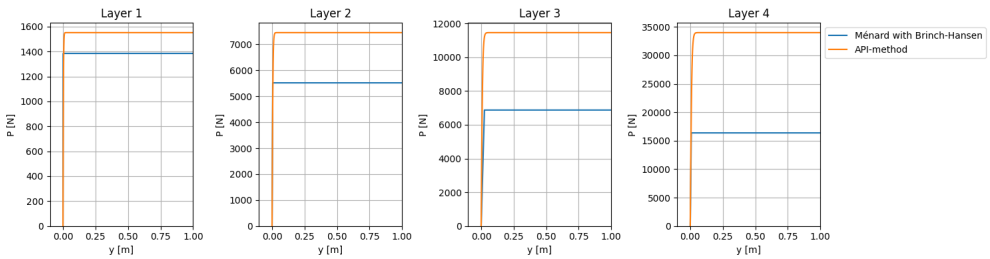

Figure 6.12: Soil model, D1: API-method and E1: Ménard with Brinch-Hansen

The API-method predicts stiffer behavior and a higher ultimate soil resistance, so less energy is absorbed by soil springs and more by the fender structure. Conversely, the Ménard with Brinch-Hansen model yields slightly larger global displacements and greater soil-spring energy absorption. These trends match findings for laterally loaded piles in literature [21].

6.2.4 Sensitivity analysis: soil-fender structure (oblique)

Additional simulations assess the structural behavior of the soil-fender structure under oblique impact loading. Unlike the head-on case, this scenario involves sliding motion between the ship's hull and the fender structure. Furthermore, oblique impacts do not result in a point of zero kinetic energy for the ship. In other words, the ship maintains a positive translational velocity throughout the simulation duration.

Parameters investigated are the static friction coefficient (F1, F2), the soil model (G1), and impact position (H1, H2). Results are summarized in table 6.9. Visualizations are given in appendix H.

Table 6.9: Summary of results flexible soil-fender structure - Oblique

	Unit	F1	F2	G1	H1	H2
Peak internal energy fender structure	MJ	1.60	1.49	1.57	1.59	1.63
Peak internal energy soil	MJ	0.28	0.25	0.31	0.29	0.26
Frictional energy dissipation	MJ	2.79	0.99	2.80	2.78	2.81
Kinetic energy ship at end	MJ	7.81	9.67	7.81	7.83	7.78
Peak displacement fender structure	m	0.90	0.87	0.91	0.88	0.92

Group F
To assess friction effects, simulation F1 (reference) employs a higher static-friction coefficient, while F2 uses a lower value than the reference case (see table 6.10).

Table 6.10: Static friction coefficients

Simulation	Static friction coefficient
F1	0.3
F2	0.1

From table 6.9, it can be seen that the simulation with a higher static friction coefficient (F1) results in higher peak values for internal energy absorption compared to simulation F2. This occurs due to a larger force component developed by friction in the longitudinal direction of the fender structure. Furthermore, increased friction leads to greater energy dissipation within the model, which is evident in the reduced kinetic energy of the ship at the end of the simulation. From these results, it can be concluded that changes in the static friction coefficient primarily influence both the frictional energy dissipation and the ship's remaining kinetic energy. While the static friction coefficient also affects the internal energy absorption by the soil-fender structure, this influence is notably smaller.

Group G
Similar to the head-on simulations in group E, the effect of the soil model is examined under oblique impact conditions. The same P-y curves are applied (figure 6.12), as they are not dependent on the type of impact. The reference model for the oblique simulations (F1) uses the P-y curves from the API-method, whereas simulation G1 uses the P-y curves based on Ménard with Brinch-Hansen.

The same characteristics are observed as in the head-on simulations of group E. Key results are summarized in table 6.9. However, the oblique impact scenario involves smaller lateral displacements of the soil-fender structure system, resulting in almost similar responses between the two different P-y relationships.

Group H
The finial result group assess the influence of the vertical impact position as shown in figure 6.13.

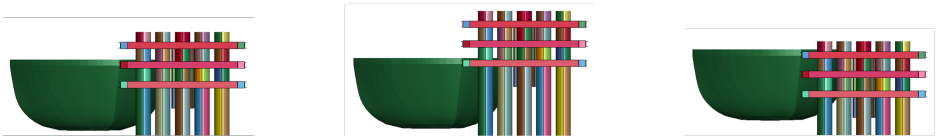

(a) F1 (b) H1 (c) H2

Figure 6.13: Impact positions, F1: middle crossbeam, H1: lower crossbeam and H2: upper crossbeam

From the results provided in table 6.9, a clear trend is visible between the different impact positions. A higher impact position results into greater internal energy adsorption by the fender structure, along with a larger global peak displacement. On the other hand, a higher impact position leads to slightly smaller deformations in the soil, which is reflected in the lower value for the peak internal energy of the soil.

6.2.5 Conclusions sensitivity analysis

A sensitivity analysis has been performed to the following model (input) parameters: steel material model, static friction coefficient, soil model, impact position, and obstacle geometry. The following conclusions are drawn:

- The two material models studied were found to have limited influence on the simulation results. The non-linear material model best describes the material behavior from experimental tests and will therefore be used in the detailed impact simulations.
- The static friction coefficient has a major influence on the simulation results for both head-on and oblique impact simulations. A higher static friction coefficient results in higher impact forces and peak responses. Therefore, neglecting friction in the models will lead to overly optimistic results.
- The soil models studied show different responses for the head-on impact, which is consistent with the obtained P-y relationships for both methods. Using the API-method results in stiffer behavior of the soil springs, leading to higher internal energy absorption by the fender structure and lower absorption by the soil springs. The opposite is observed when using Brinch-Hansen with Ménard. For the oblique impact, the difference in the response becomes negligible, and almost the same results are obtained.
- The vertical impact position between the ship and fender structure does influence the contribution of the internal energy of the fender structure and soil springs. A higher impact position results in larger values for the fender structure and lower for the soil. However, these differences remain within a deviation of a few percent.
- Comparing an impact between a rigid wall or rigid fender and a flexible ship structure was found to have major influence on the simulation results. Reducing the impact area results in a smaller impact force, but larger crushing depth and longer impact duration are observed.

In conclusion, the NLFE models respond as expected. Furthermore, valuable insights have been gained regarding the behavior of the individual models under different circumstances, which can be useful for extrapolating the results obtained from the detailed model, where only one specific impact configuration is considered.

6.3 RESULTS NON-LINEAR FINITE ELEMENT SIMULATIONS

In this section, the final simulations results are presented. As discussed in section 3.2, two simulations were performed: a head-on and an oblique simulation. In these simulations, all models behave flexibly and interact simultaneously. This setup allows the ship, soil, and fender structure to fully interact with each other during the impact event.

First, the impact configuration is described by specifying the applied input parameters and position of first

interaction (impact position). This is followed by a discussion of the simulation results for the head-on impact. Lastly, the stimulation results for the oblique impact scenario are presented and discussed.

6.3.1 Impact Configuration

The impact configuration for the head-on simulation is described first. Figure 6.14a shows a top view of the initial state the NLFE model. This figure also indicates the direction of the ship's initial velocity and the eccentricity between the ship's central axis and that of the fender structure. The level of the ship's upper deck aligns with the uppermost crossbeam of the fender structure. Therefore, the first contact between the ship and the fender structure is at the level of the upper most crossbeam of the fender structure. This location is marked in figure 6.14c.

For the oblique impact, the ship is translated to the side of the fender structure and oriented at an angle relative to the waterway axis. The ship's initial velocity again follows the direction of its central axis. A top view of the initial state is shown in figure 6.14b. As with the head-on impact, the initial impact position is highlighted in figure 6.14c.

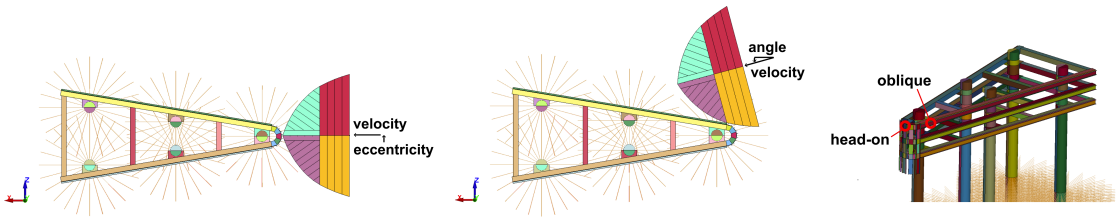

(a) Head-on impact (b) Oblique impact (c) Impact positions

Figure 6.14: Overview impact configurations NLFE model

The model input parameters for the head-on and oblique impact simulations are summarized in table 6.11 and table 6.12, respectively. The input parameters identical for both impact simulations. The non-linear steel material model described in section 4.4 is used. A static friction coefficient of 0.3 is applied. The non-linear soil springs are modeled using the force-displacement relationships derived from the API-method. In the last column of table 6.11, the eccentricity value is specified. In table 6.12 this column provides the value for the angle.

Table 6.11: Simulations configuration: head-on impact

Material model	Static friction coefficient	Soil model	eccentricity
non-linear	0.3	API-method	50 mm

Table 6.12: Simulations configuration: oblique impact

Material model	Static friction coefficient	Soil model	angle
non-linear	0.3	API-method	15 ^{o}

6.3.2 Head-On Impact

In the following paragraphs, the simulation results for the head-on impact are presented and discussed. Visualization of these simulation results are provided in appendix I.

Global energy balance

During the simulation, various energy components are recorded in LS-DYNA. First, the global energy of the simulation is evaluated. Figure 6.15 shows the global energies recorded during the head-on impact simulation. Global means that all energy contributions from the individual models are summed up and

reported as a single parameter. The total energy primarily consist out of kinetic energy, internal energy, hourglass energy, and frictional dissipative energy.

No external forces are applied during the simulation. The ship structure, including the point mass, is assigned an initial velocity, which is applied instantly at the first time step. Since no external forces act on the bodies during the analysis timeframe, a closed system is at hand. A characteristic of a closed system is that its total energy remains constant over time. This condition is clearly satisfied in the global energy balance.

Furthermore, it is observed that the largest portion of the initial kinetic energy is converted into internal energy. The reported internal energy consists of both elastic and plastic strain energy. Only a small value of frictional dissipative energy is recorded, which aligns with the expectation for a head-on impact. Finally, the hourglass energy remains well below the 10% of the peak internal energy. Therefore, from the perspective of energy balance, it is proven that the numerical simulation accuracy and mesh resolution are satisfactory.

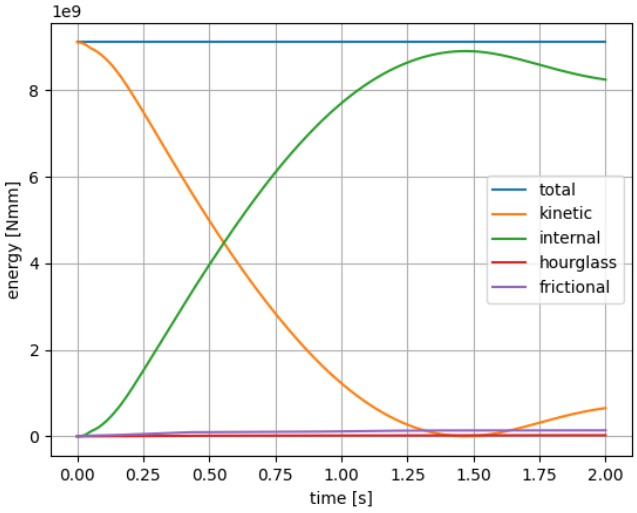

Figure 6.15: Head-on: global energy balance

Model energy balance

To provide a more detailed view of energy absorption during the simulation, internal energies at model level are presented in figure 6.16. This figure shows the individual energy contributions of the soil springs, ship structure, and fender structure.

Focusing first on the internal energy of the fender structure. The structure is initially at rest, as indicated by the zero initial energy at $t = 0.00s$. From the moment of interaction between the ship and fender structure, a smooth increase in internal energy is observed, peaking around $t = 1.40s$. After reaching this maximum, the internal energy gradually decreases. This corresponds with the release of the stored elastic strain energy in the structure that is released during the unloading of the structure. Nevertheless, a significant amount of internal energy is remains at $t = 2.00s$, due to the extensive plastic deformation that has been developed during the impact loading.

The internal energy of the soil follows a similar trend to that of the fender structure, though with a smaller magnitude. This is consistent with expectations for a coupled system, in which the fender structure's piles are directly connected to the soil springs. As a result, an increasing value for the internal energy of the soil is observed during the loading stage of the fender structure (until $t = 1.40s$). However, unlike the fender structure, the internal energy in the soil remains nearly constant during unloading. This behavior is explained by the characteristics of the P-y curves, which reach a plateau at relatively small displacements

(< 0.10 m), after which permanent (plastic) deformation occurs. As a result, only a small amount of elastic energy is stored during the loading, leading to a minimal decay in internal energy for $t > 1.40s$.

Turning to the ship's internal energy. It begins at zero at $t = 0s$, then increases until approximately $t = 0.40s$. At this point, instead of a smooth curve, a kink is recorded in the internal energy, after which the internal energy resumes a smooth increase towards the end of the simulation. This phenomenon will be examined further in the next paragraph through analysis of the deformation patterns during the simulation.

In contrast to internal energy, the ship's kinetic energy does not start at a zero. At $t = 0.00s$, it matches the total global energy and begins to decay smoothly until it reaches nearly zero at $t = 1.40s$. After this point, a increase is observed. As previously explained, the elastic strain energy stored in the soil-fender system is partially returned to the system for $t > 1.40s$, pushing the ship backward (opposite direction of the initial motion) and causing kinetic energy to reappear toward the end of the simulation.

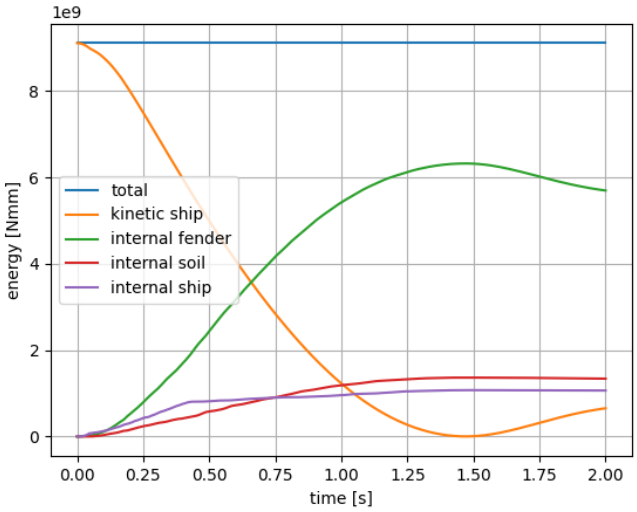

Figure 6.16: Head-on: model energy balance

Deformations

Deformations of the ship's bow structure during the head-on impact simulation at discrete moments in time are shown in figure 6.17. Relative displacements are presented, as the bow structure undergoes translational motion throughout the simulation. The same approach is used for the displacements of the fender structure in figure 6.18.

At the start of the simulation (t = 0.00s), both the ship and fender structure are in their undeformed, initial state. From this point onward, the ship structure and fender structure start interacting, leading to increasing deformation in both structures. Deformations continue to grow until $t = 1.48s$, when the ship's kinetic energy is nearly zero, and maximum internal deformations are reached in both structures. This observation aligns with the model-level energy balance shown in figure 6.16. After this preak response, and up to the end of the simulation (t = 2.00s), elastic energy gradually restored, leading to decreasing deformations as the structures begin to return toward their initial state.

When analyzing the model-level energy balance (figure 6.16), a kink was noted in the internal energy curve of the ship structure around $t = 0.43s$. From the simulation results, it is evident that the majority of the bow crushing occurs during the first half second of the simulation. While deformation of the ship's bow continues after this point, it proceeds at a significantly lower rate, leading to the kink in the internal energy curve of the ship.

In contrast, the deformation of the fender structure show a more gradual increase until the peak response

is reached. This corresponds to the smooth internal energy development for both the soil springs and the fender structure.

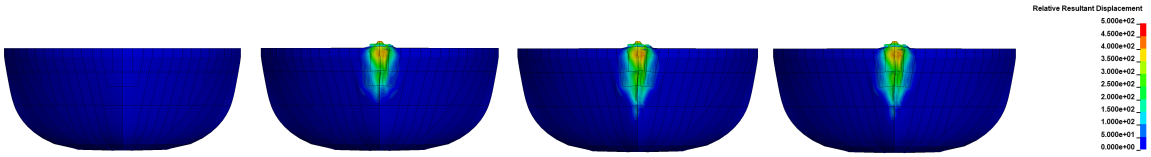

(a) t = 0.00 s **(b)** t = 0.43 s **(c)** t = 1.48 s **(d)** t = 2.00 s **(e)**

Figure 6.17: Head-on: deformations ship structure

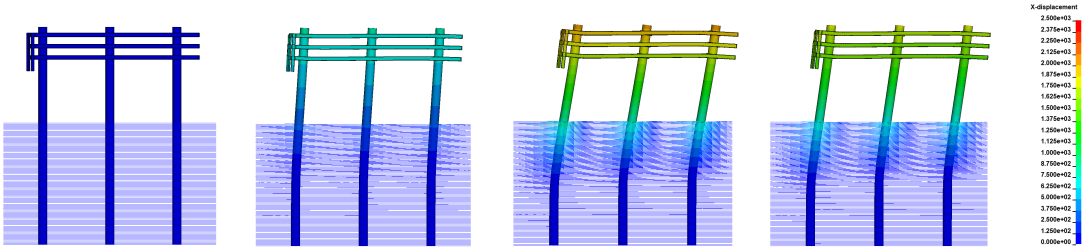

(a) t = 0.00 s **(b)** t = 0.43 s **(c)** t = 1.48 s **(d)** t = 2.00 s **(e)**

Figure 6.18: Head-on: deformations fender structure

Analysis relative energy absorption
To compare the contributions to kinetic energy absorption by the different model parts, a relative energy absorption metric is introduced. The relative energy absorption at any moment in time can be calculated by dividing the individual energy quantity by the total energy and multiplying by 100 to obtain a percentage. Results for this metric at $t = 1.40s$ are given in table 6.13. At this time step, the ship's kinetic energy is zero and, therefore all initial kinetic energy must have been absorbed as internal energy by the ship, soil, and fender structure, or dissipated through friction. The largest portion of the energy is absorbed by the fender structure where 69% of the total energy is absorbed by the internal deformation of the fender structure. The soil springs contribute 15%, while the ship structure accounts for 12%. Small amounts remain for frictional dissipation and artificial energy.

Table 6.13: Head-on: relative energy absorption at $t = 1.40s$

Part	Relative energy absorption
Fender structure	69%
Soil springs	15%
Ship structure	12%
Frictional dissipation	2%
Artificial energy	2%

6.3.3 Oblique Impact

In the following paragraphs, the simulation results for the oblique impact are presented and discussed. More detailed visualizations of the simulation results are provided in appendix I.

Global energy balance
Similar to section 6.3.2, global energies are recorded during the impact simulation. Results are presented in figure 6.19. The conditions for a closed system are also satisfied for the oblique impact simulation.

The recorded total energy remains constant throughout the simulation and equals the initial kinetic energy of the ship. The kinetic energy shows a smooth decreasing trend towards the end time of the simulation. However, in contrast to the head-on impact, a large amount of kinetic energy is conserved at the end.

The internal energy shows a smooth increasing trend until a peak is reached at approximately $t = 1.25s$, after which a gradual decrease is observed until the end of the simulation. Similar to the head-on impact, the internal energy consists of both elastic and plastic strain energies, which are combined into a single value at every time step. During the oblique impact simulation, frictional dissipative energy is recorded, showing a smooth increase throughout the simulation. At the end of the simulation, the slope of the frictional dissipative energy curve becomes zero, implying that no further energy is dissipated by friction from this point onward. Finally, hourglass energy is reported and remains well below 10% of peak internal energy.

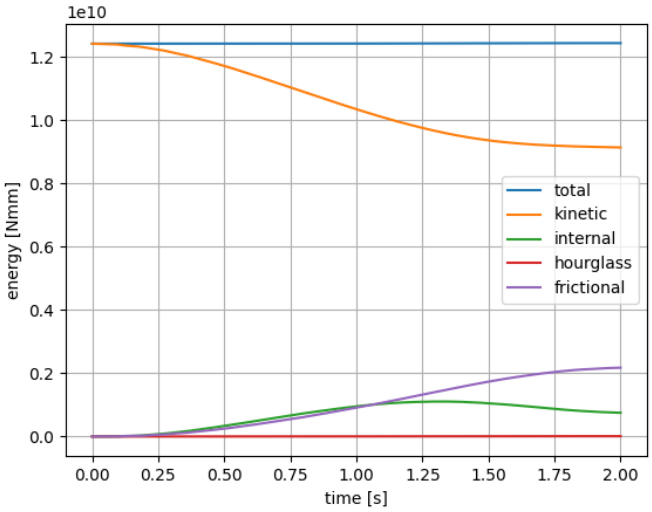

Figure 6.19: Oblique: global energy balance

Model energy balance

Moving from the global level to the model level, figure 6.20 presents the internal energy development for the soil springs, ship structure, and the fender structure. Focusing on the internal energy of the fender structure over time, a smooth increase is observed until $t = 1.30s$. Beyond this point, a gradual decrease occurs until the end of the simulation at $t = 2.00s$, as elastic energy is released and the fender structure tends to return to its initial shape. The internal energy of the soil follows a similar trend. As with the head-on impact, the fender structure and soil springs are directly coupled. Therefore, similar behavior in the development of internal energy between the fender structure and the soil is expected, and the energy balance confirms this expectation.

The internal energy of the ship increases slightly during the loading stage of the impact. However, the amount of internal energy developed in the ship's bow structure remains very low compared to the total energy involved in the simulation. A more predominant effect is observed for the frictional energy dissipation during the oblique impact simulation. In the model, frictional contact is implemented by defining a static friction coefficient ($\mu = 0.3$). The frictional energy dissipation increases steadily throughout the simulation and stabilizes at the end.

Finally, the kinetic energy of the ship is equal to the total global energy at $t = 0.00s$. The kinetic energy of the ship decreases from the moment the fender structure and the ship's bow interact. At the end of the simulation, at $t = 2.00s$, the ship still retains a significant portion of its initial kinetic energy. In conclusion, part of the ship's initial kinetic energy is dissipated by friction. Furthermore, due to the impact with the fender structure, this ship's translational motion and rotation (yawing) are altered, and by the end of the simulation, the ship is moving away from the fender structure with a remaining amount of kinetic energy.

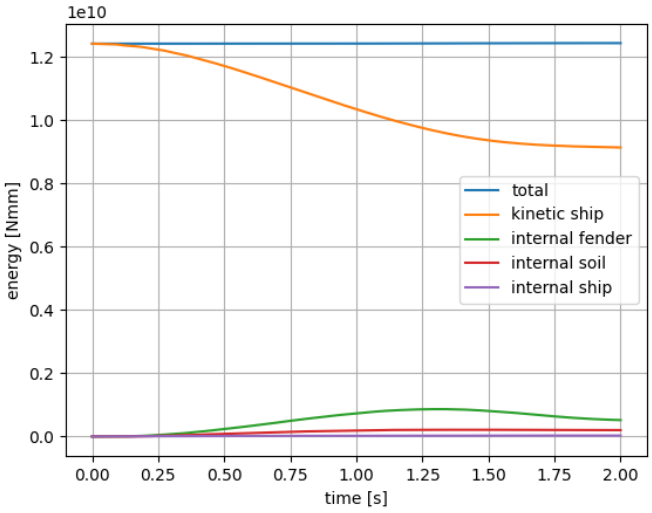

Figure 6.20: Oblique: model energy balance

Deformations

A top view of the transient response of the oblique impact simulation is provided in figure 6.21. At the initial time step ($t = 0.00s$) the ship structure and fender structure are not in contact. The second time frame at $t = 1.30s$, corresponds to the peak internal energy of the fender structure. At this moment, the maximum global displacement for the fender structure is reached. Finally, at the end of the simulation ($t = 2.00s$), contact begins to be lost between the ship structure and the fender structure, after which the ship starts moving away. This behavior is consistent with the observed frictional dissipative energy in the global energy balance for this simulation. The sliding motion between the ship's bow and the crossbeams of the fender structure takes place along almost half of the length of the fender structure for nearly the entire simulation time.

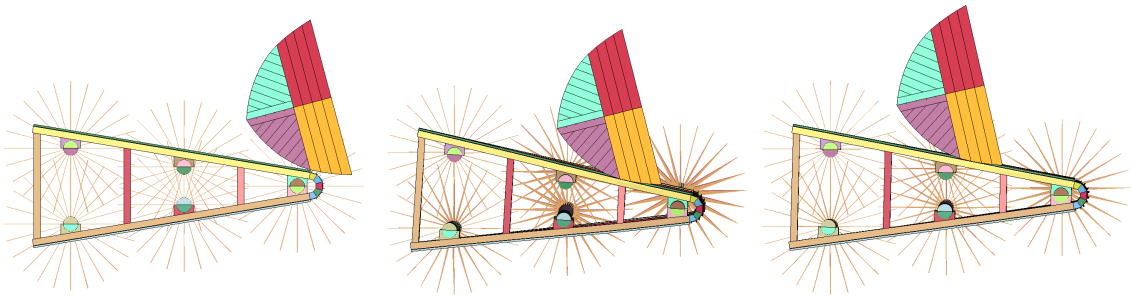

(a) t = 0.00 s **(b)** t = 1.30 s **(c)** t = 2.00 s

Figure 6.21: Oblique: top-view simulation

Figure 6.22 shows a top view of the resultant displacements of the fender structure. Peak resultant displacement is reached at rightmost pile of the fender structure around $t = 1.30s$. Furthermore, it can be seen that the fender structure undergoes a clockwise global rotation at this time step. At the end of the simulation, the fender structure has partially returned to its initial state. No plastic strain limit is reached in the steel of the fender structure. However, at the soil springs just below the riverbed, the ultimate resistance of the soil is reached, resulting in non-zero displacements at the end of the simulation.

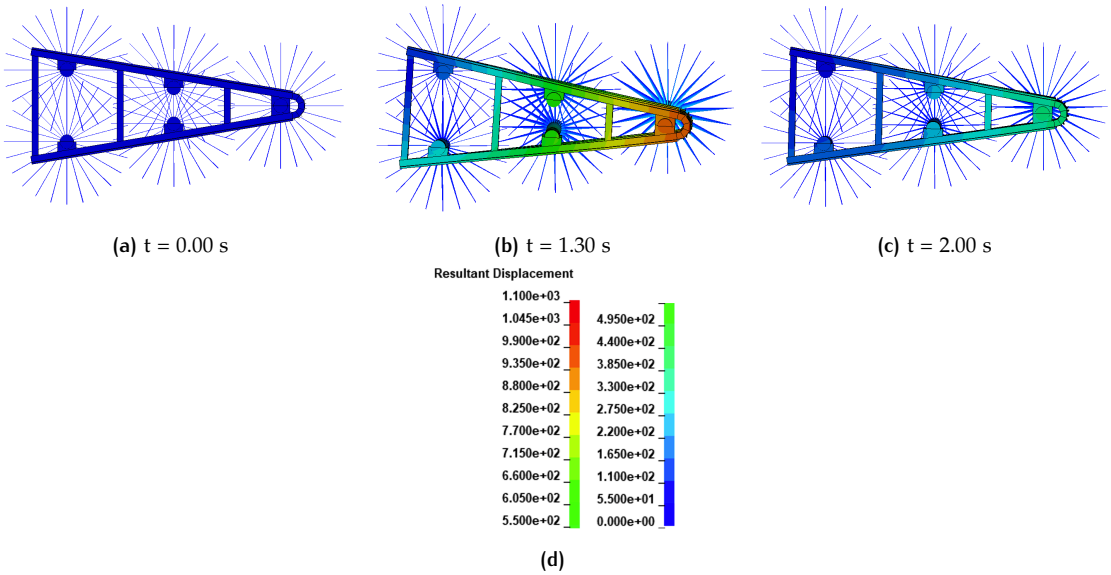

(a) t = 0.00 s **(b)** t = 1.30 s **(c)** t = 2.00 s

(d)

Figure 6.22: Oblique: deformations fender structure

As observed in the model-level energy balance, only a small amount of internal energy is developed in the ship structure. As a result, only minor deformations occur at the ship structure during the impact. Figure 6.23 presents the Von Mises-stress at the outer bow structure, at the impact position, during the simulation. The recorded stress concentrations show average values around 230 MPa. Furthermore, at $t = 0.75s$, a small region with a peak value around 280 MPa is observed. Therefore, Von Mises-stress concentrations remain in the elastic regime for almost the entire bow structure.

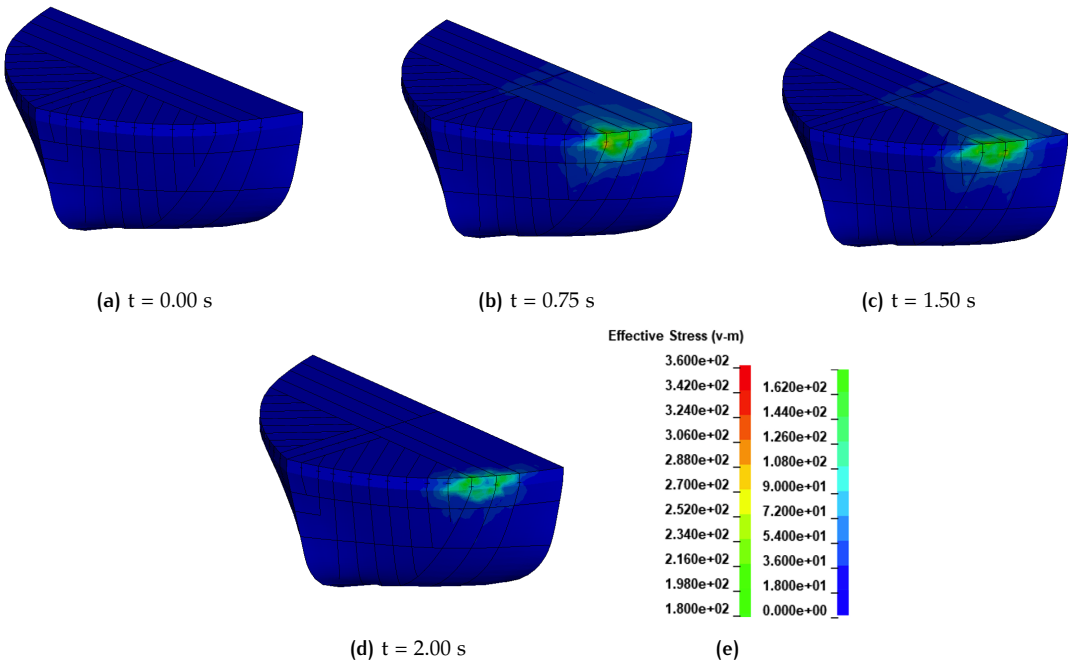

(a) t = 0.00 s **(b)** t = 0.75 s **(c)** t = 1.50 s

(d) t = 2.00 s **(e)**

Figure 6.23: Oblique: Von Mises-stress ship structure

Relative energy absorption contributions

Energy absorption percentages with respect to the total global energy are reported in table 6.14. Values are taken at $t = 1.3s$, when the maximum global displacement occurs for the fender structure. Around 11% of the initial kinetic energy is dissipated by contact friction between the crossbeam of the fender structure

and the ship's bow. The fender structure absorbs approximately 7% of the initial kinetic energy. Around 2% is absorbed by the soil springs and for the ship structure only a small percentage of 0.3% is found.

Summing up all the contributions provided in table 6.14 results into a relative initial kinetic energy absorption by the soil springs, ship structure, and fender structure of 9%. Adding the contribution of frictional dissipative energy brings the total to 19.8%. In comparison, for the head-on impact, energy absorption reaches almost 100% of the initial kinetic energy. At the end of the oblique impact, the ship retains a large portion of its initial kinetic energy. At $t = 1.3s$, the ship still contains around 77% of the initial kinetic energy. Therefore, this provides a logical explanation for the difference in the energy absorption contributions between the head-on and oblique impact.

Table 6.14: Oblique: relative energy absorption at $t = 1.3s$

Part	Relative energy absorption
Fender structure	7.0%
Soil springs	1.7%
Ship structure	0.3%
Frictional dissipation	10.8%

6.4 COMPARISON SIMPLIFIED MODEL WITH HEAD-ON NLFE MODEL

This section provides a comparison between simplified model and the NLFE model. The simplified model is developed to obtain a transient response of the fender structure during a head-on impact loading. Therefore, only a comparison with the head-on impact simulation, from section 6.3, is included.

Figure 6.24 presents the peak global displacements over time for the two models considered. The peak global displacement takes place at the top of the piles of the fender structure. This holds for both models. The pieces of the pile above the upper crossbeam are not included in the simplified model, therefore pile displacement at the upper crossbeam are used for the peak displacement of the NLFE model.

A significant difference is observed in the extreme values shown in the graph. The simplified model underestimates the response by approximately a factor 2.6 compared to the NLFE model. Furthermore, the impact duration deviates significantly. For the simplified model, the peak displacement takes place at $t = 0.69s$. In the NLFE model this peak value is observed at $t = 1.48s$.

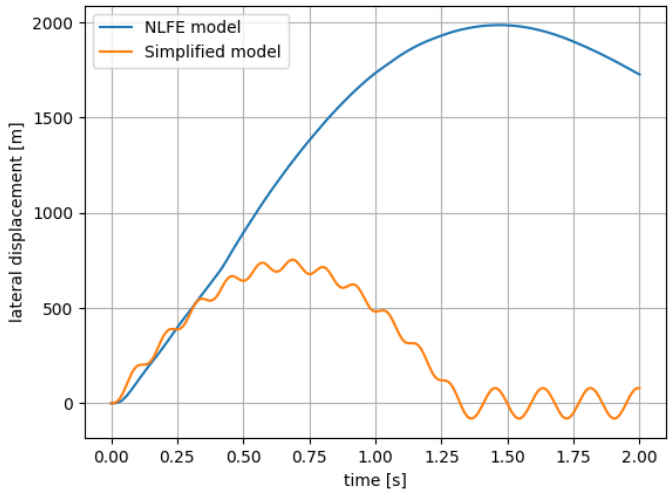

Figure 6.24: Comparison peak displacements fender structure for NLFE and simplified model

To study the difference in more depth, a comparison of the full fender structure is provided in figure 6.25 at $t = 0.23s$. At this time increment, the global peak displacements are equal for both models, as can be observed in figure 6.24. It can be seen that the response of the fender structure follow the same path in both models. The crossbeams are slightly bent in both models, but remain almost straight. Examining the pile displacements within the soil, it is evident that significant displacements occur only in the uppermost soil layer in both models. In the simplified model, the soil layers are colored and labeled from L1 to L4. In general, it can be concluded that at $t = 0.23s$, the same response is obtained for both models.

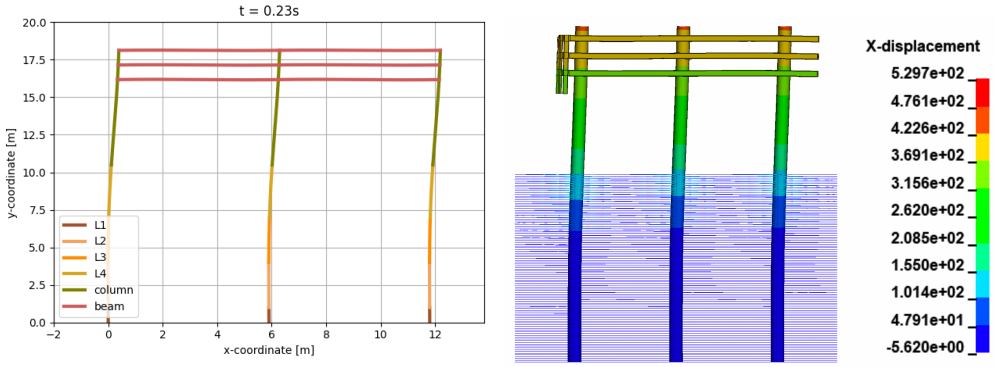

(a) Simplified model **(b)** NLFE model

Figure 6.25: Comparison displacements at t = 0.23s

Another comparative plot is presented in figure 6.26, where for both models, the time frame at peak response is chosen. For the simplified model, the peak response occurs at $t = 0.69s$, whereas for the NLFE model, it occurs at $t = 1.48s$. In contrast to the comparison made earlier, clear differences are visible for the peak response of the fender structure.

Focusing on the upper part of the piles, where a connection with the (horizontal) crossbeams is present, the simplified model shows that the upper part of the fender structure behaves more rigidly compared to the NLFE model. The piles exhibit much larger curvature and tend to become nearly vertical. In the NLFE model, the upper part of the piles shows only a a small curvature and remains almost straight relative to the pile sections below the crossbeams.

Furthermore, a significant difference is observed in the pile displacements within the soil. In the simplified model, the largest displacements still occur only in the uppermost soil laye, with only a very small displacement observed at the top of the second soil layer. In the NLFE model, displacements have become significantly larger in the two uppermost soil layers. As a result, the bending point of the piles embedded in the soil moves downward.

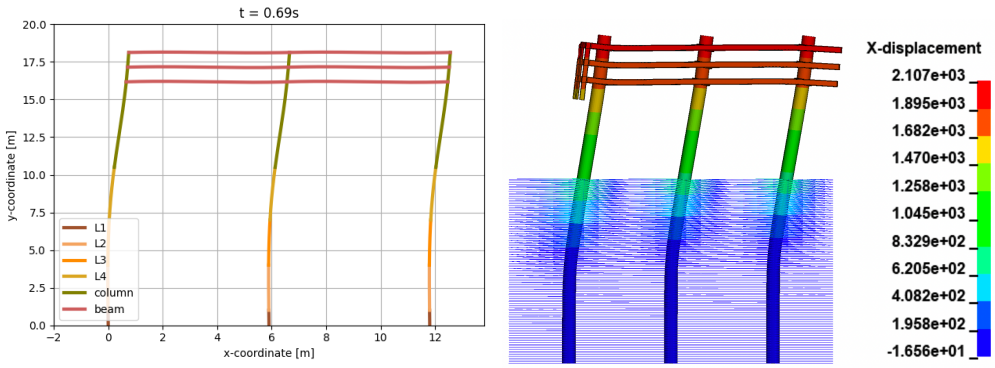

(a) Simplified model **(b)** NLFE model

Figure 6.26: Comparison displacements at (a) t = 0.69s and (b) t = 1.48s

The peak response for both models shows clear differences, which can be attributed to assumptions made during model development. The simplified model relies on the theory of a beam on an elastic foundation, so no plastic deformations can occur in its response. In contrast, the NLFE model includes plastic material behavior in both the steel structure and soil springs. From the derivation of the P-y curves for the NLFE model, it is known that after small displacement values, the soil springs begin to behave plastically, resulting in larger soil displacements and a different loading of the steel piles of the structure.

As mentioned earlier in this section, a clear difference is observed in the structural behavior at the intersections of the crossbeams with the piles. In the simplified model, the crossbeams are coupled rigidly to the piles by means of boundary conditions, so no relative rotations can occur at the connecting elements. In the NLFE model, connections are realized using steel plates. Under small loading conditions the connecting plates behave elastically and only small deformations occur. However, with increased loading, stress concentrations become larger and plastic deformations develop in the connecting plates. As a result, relative rotation occurs between the crossbeams and the piles.

Model responses are also affected by the element formulation used. The simplified model relies on 1D beam elements, which are not able to develop local deformations in the cross-section. In the NLFE model, structural elements are modeled using shell elements in 3D space which are able to capture local deformations of the cross-section. In the response of the NLFE model, a phenomenon called "ovalisation" is observed at the piles of the fender structure. Due to the high bending moment at the pile sections embedded into the soil, the cross section tends to deform into an oval shape. As a result, bending resistance decreases in the loading direction resulting into larger stress levels and curvature of the piles.

In conclusion, a similar response is obtained during the first 0.23 seconds of the analysis, where the responses are dominated by elastic material and soil behavior. From this point onward, the responses start to deviate significantly. However, the different behavior observed can be explained by the underlying model assumptions.

6.5 COMPARISON NLFE MODEL WITH THE DUTCH CODES

In this section, the impact simulations of the NLFE model from section 6.3 are compared with the design methodology prescribed in the Dutch codes. First, the design formula for the required energy absorption capacity is restated, and an explanation of the coefficients is provided. This is followed by a comparison between the energy absorption obtained for the soil-fender system from the NLFE model and the required energy absorption capacity from the code. At the end of this section, results are discussed and reviewed in the context of the design methodology outlined in the codes.

6.5.1 Design Provisions Dutch Codes

The "Richtlijnen Ontwerpen Kunstwerken" (ROK) [1] provides design guidance for fender structures during impact events. As described in section 2.2, the ROK uses a required energy absorption capacity approach. To calculate the design value for the required energy absorption capacity, the ROK refers to the EAU 2012 [2]. This formula is restated in equation (6.2).

$$E_d = \frac{1}{2} \cdot G \cdot v_{\perp}^2 \cdot C_e \cdot C_m \cdot C_s \cdot C_c \tag{6.2}$$

The following provide a description of the coefficients in accordance with the design guidelines.

Eccentricity factor C_e:
The eccentricity factor accounts for the effect that the point of impact between the ship and the fender structure is usually aligned with the middle of the ship's side. As a result, the point of impact does not coincide with the ship's center of mass. In the EAU 2012, the formula given in (6.3) is proposed to calculate the eccentricity factor.

$$C_e = \frac{k^2 + r^2 \cos^2 \alpha}{k^2 + r^2} \tag{6.3}$$

Where,
k is the radius of gyration of the ship [m]
r is the distance between the ship's center of mass and the point of impact [m]
α is the angle between the velocity vector and and distance r [^{o}]

Figure 6.27 shows the definition of the different parameters included in the equation for the eccentricity factor. The radius of gyration may be approximated by $0.25L$ for ship's with a high block factor. For this research, it is assumed that this is a valid assumption.

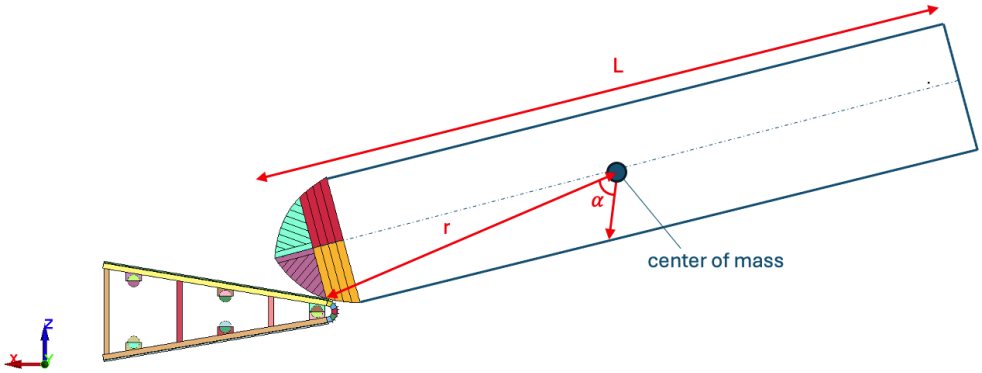

Figure 6.27: Schematic overview eccentricity factor parameters

During head-on impact events, under the assumption that the ship's central axis is aligned with the fender structure, the eccentricity factor drops out of the equation by setting C_e equal to 1.0.

Virtual mass factor C_m:
The virtual mass factor is similar to the hydrodynamic coefficient reported earlier in this report (section 3.4). For site conditions where the keel clearance is greater than half the draft of the ship, a value of $C_m = 1.1$ should be applied for head-on impacts and $C_m = 1.5$ for oblique impacts. This is in accordance with the applied value during the non-linear finite element simulation.

Ship flexibility factor C_s:
For the ship flexibility factor, no clear definition is provided in the codes. Only a statement is made that when designing hard fenders in combination with large vessels, a value between $0.9 < C_s \leq 1.0$ must be applied. When dealing with soft fenders and small vessels, a factor of $C_s = 1.0$ is prescribed.

Waterfront attenuation factor C_c:
For open waterfront structures, such as steel piled fender structures, a value of $C_c = 1.0$ must be applied.

6.5.2 Calculation Required Energy Absorption Capacity

Table 6.15 provides the values applicable for the head-on impact scenario in the second column, while the third column presents the values for the oblique impact scenario.

The calculation of the required energy absorption capacity for the head-on impact scenario is straightforward. For the velocity perpendicular to the fender structure ($v_\perp$), the sailing velocity of the ship (= 3.0 m/s) must be used. The coefficients are taken as prescribed in section 6.5.1.

For the oblique impact scenario, some additional values need to be defined. For the calculation of the eccentricity factor, the length of the ship (L) is 86 m. Additionally, the angle between the velocity vector perpendicular to the fender structure ($v_\perp$) and the ship's center of mass is $\alpha = 66^o$. The sailing velocity

perpendicular to the fender structure can be derived by $v_{\perp} = 3.0 \sin(9 + 15)$. Here, 9 is the angle of the funnel of the fender structure, and 15 is the angle between the ship's central axis and the waterway axis. Both values given in degrees.

Substitution of all variables into (6.2) yields the design value for the required energy absorption capacity (E_d), which is shown in the last row of the table.

Table 6.15: Calculation required energy absorption capacity

Parameter	Head-On	Oblique	Unit
G	1840	1840	tonne
$v_{\perp}$	3.0	1.22	m/s
C_e	1.0	0.35	[-]
C_m	1.1	1.5	[-]
C_s	1.0	1.0	[-]
C_c	1.0	1.0	[-]
E_d	9.11	0.72	MJ

6.5.3 Comparison and Discussions

The results are compared and presented in a bar chart in figure 6.28. The values corresponding to the NLFE model represent the sum of the internal energy of the fender structure and the soil springs. For the head-on impact, this results into a value of 7.60 MJ. For the oblique impact, a value of 1.08 MJ is obtained. Additionally, the values derived according to the design guidelines are presented and labeled as "Codes".

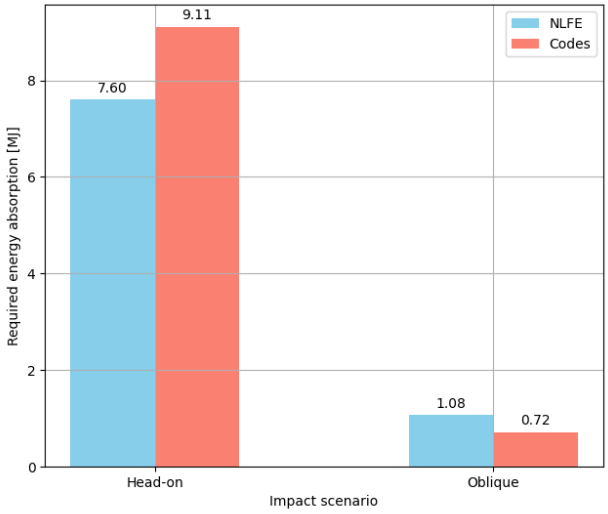

Figure 6.28: Comparison energy absorption between NLFE models and Dutch codes

Discussion head-on impact scenario

In the calculation of the required energy absorption capacity according to the codes, a ship flexibility factor (C_s) equal 1.0 is used. However, for the head-on impact simulation from section 6.3.2, a relative energy absorption for the ship was found to be 12%. Furthermore, a total of 4% of the initial kinetic energy is dissipated by friction and artificial energy. By subtracting these percentages from the value obtained from the codes, $9.11 - \frac{100-12-4}{100} = 7.6$ MJ, the same value as presented in the bar chart is found. Based on the simulation results, a value for the ship flexibility coefficient equal $1.0 - 0.12 = 0.88$ can be justified.

The artificial energy dissipation is a numerical artifact inherent to the methodology and cannot be included in the design guidelines. Furthermore, frictional dissipation is also is not accounted for in the formula provided in the codes. The contribution from friction was found to be limited (around 2%).

Discussion oblique impact scenario
As with the head-on impact scenario, a ship flexibility factor (C_s) equal to 1.0 is used for the oblique impact scenario. In the NLFE simulation in section 6.3.3, it is observed that the relative energy absorption of the ship is only 0.3%. Therefore, reducing the ship flexibility factor would be overly optimistic for this specific impact event. Nevertheless, the NLFE model still achieves an energy absorption that is a factor 1.5 higher than the required energy absorption capacity specified by the codes.

A significant difference between the NLFE model and the design codes is that the NLFE model simulates a simplifies representation of the dynamic process. As a result, certain model assumptions were made at the start of this research. The design methodology from the codes also employs a highly schematized approach to the real dynamic process, relying on model assumptions and simplifications that differ from those in the NLFE model. Therefore, the gap observed between the energy absorption values does not necessarily have to be considered remarkable. The following paragraphs elaborate on this.

To begin with, in the NLFE model, it is assumed that the portion of the ship not explicitly modeled can be represented by a point mass at the ship's center of mass. Additionally, it is assumed that the yawing behavior can be represented by a rotational inertia at this point mass. This is a significant simplification of the real process, especially when combining with the simplification of the hydrodynamic effects, which are incorporated as added mass to the ship. The influence of these simplification on the energy absorption capacity in the NLFE simulation results has not been investigated and remains uncertain.

Secondly, the NLFE model includes friction by specifying a static friction coefficient at interacting bodies. From the sensitivity study in section 6.2.4, it is observed that the static friction coefficient has a significant effect on the energy absorption of the fender-soil system. This component is not accounted for in the formula provided in the Dutch codes and therefore contributes to a lower calculated energy absorption for the fender-soil system when following the codes.

Finally, the NLFE model does not include any form of damping. Which is a significant simplification of reality, where the steel structure, connections, and surrounding soil would introduce some damping to the system. Therefore, it is highly probable that including damping in the NLFE model would result in a lower peak response. In contrast, to the design methodology of the codes, in which the required energy absorption capacity is converted into an equivalent static load, does not involve the inclusion of damping.

7

Conclusions and Recommendations

In the final chapter of this thesis conclusions are provided. Furthermore, limitations are discussed, and recommendations for future research are presented in the final section.

First, a restatement of the main research question is given below:

What is the transient response of the ship, soil, and fender structure system during head-on and oblique impact events, and how does this compare to the equivalent static load method used in the Dutch codes?

7.1 CONCLUSIONS

The purpose of this thesis is to establish a method to derive the transient response of the fender structure under head-on and oblique impact loading taking into account the interaction between the ship, soil, and fender structure and compare this to the current design methodology prescribed in the Dutch codes. To study this behavior an existing fender structure is used in the analysis with fixed geometrical properties, CPT data at the construction site is used for the soil model, and a reference vessel of CEMT class IV is used.

First, the background of the problem is studied to provide the required knowledge to understand the problem at hand. By doing this, information is gathered about establishment of the current design methodology adopted in the Dutch codes. Furthermore, before developing the simulation models studies have been performed to the implementation of the soil model, and material models for the structural steel. From this study, it was found that two CPT-based methods are widely used to define properties for the non-linear springs that represent the soil behavior at laterally loaded piles: API-method and Brinch-Hansen with Ménard.

A dynamic non-linear finite element model (NLFE) is developed using LS-DYNA which utilizes a numerical explicit solver. A sensitivity study is conducted to study the behavior of the separate models (soil, ship, and fender) during head-on and oblique impact events. Multiple simulations are performed between rigid ship and flexible soil-fender system. The same is done for impacts between rigid wall/fender structure and flexible ship structure. The responses obtained by the two different soil models are in agreement to relations found in literature in studies to laterally loaded monopoles. The API-method results into a stiffer force-displacement relations compared to the relations obtained with Brinch-Hansen with Ménard. For the head-on impact this results into a slightly different response between the two applied methods. However, for the oblique impact scenario almost similar results are obtained for both methods. Furthermore, sensitivities to model input parameters are addressed for: the static friction coefficient, steel material model, and impact position. Results obtained are in line with the expected behavior.

Additionally, a simplified dynamic model is developed. A comparison between the simplified model and the non-linear finite element model is included for the head-on impact. The simplified model relies on the assumption of a linear model which seems to be inappropriate in analyzing the transient response

under head-on impact loading. High level of plastic deformations occur in the NLFE model which results into significantly larger displacements of the soil springs and fender structure. However, the two models show agreement in the response during the initial stage of the impact loading where the responses are dominated in the elastic regime.

Contributions to the initial kinetic energy absorption are extracted form the NLFE simulations for both impact scenarios. Results showed that for the head-on impact also a significant amount of energy is absorbed by crushing of the ship. For the oblique impact this contribution is found to be very small. Furthermore, at the head-on impact scenario largest part of the initial kinetic energy is absorbed by the fender-soil system, a percentage of 84% is observed. For the oblique impact scenario the fender-soil system only absorbed 9% of the ship's initial kinetic energy. This as a result of the large amount of kinetic energy that is conserved by the ship after the impact. From the NLFE simulation it is observed that after the impact event, the ship still contains 77% of the initial kinetic energy.

With the answers to the sub-research questions known, the main research question can be answered. The NLFE model developed in this thesis is able to obtain a transient response of the fender structure taking into account the interaction between the soil, ship, and fender structure. Comparison with the design formula for the required energy absorption capacity from the Dutch codes resulted into a higher energy absorption of the fender-soil system for the oblique impact simulation while using the NLFE model. The model assumptions made in the NLFE model differ from the assumptions made in the design codes which results into different energy absorption quantities between the two methods. For the head-on impact, similar results are obtained when a reduced ship flexibility factor (C_s) is used in the calculation of the required energy absorption capacity. It must be noted that the accuracy of the predicted responses can still be discussed, since no experimental data was available for the structures at interest.

7.2 LIMITATIONS

One of the important limitations of the NLFE model is the simplification of the fluid through the use of added mass applied to the ship's bow structure. In both the head-on and the oblique impact simulations the boundary conditions constrain multiple degrees of freedom that, in reality, are not fixed. Therefore, it remains unknown how much this simplification influences the calculated energy absorption capacity of the soil-fender system. Further research aimed at improving the boundary conditions for the ship's bow structure is therefore highly recommended.

Furthermore, for the boundary conditions of the fender structure, it was assumed that the piles are fixed in the vertical direction at their base. Due to impact loading, large axial forces develop in the piles as a result of this boundary condition. A more realistic structural response could be achieved by improving this assumption, for example, by modelling the pile bases with (non-linear) springs instead of fixed constraints.

The material model applied for the structural steel also introduces some limitations, as a simplified material model was used in this research. Strain rate effects were not included, and no mesh size-dependent fracture criterion was derived using the calibration case described in DNV-RP C208. These simplifications result in less realistic material behavior and should be addressed in future model development.

Additional simplifications were made in the setup of the model geometries. Connections between plates or steel profiles were modeled using mesh connections. As a result, local failure in connections (e.g. bolts or welds) cannot be realistically captured in the NLFE model.

Another major limitation of the method applied in this research is the computational cost of the non-linear finite element simulations. Even though only a small portion of the ship structure was included in the model, a large number of nodes and element are required to achieve sufficient mesh resolution and convergence. This is especially true for the ship structure, which was found to be not been fully converged even with mesh sizes of 50 mm.

7.3 RECOMMENDATIONS FOR FUTURE RESEARCH

The final section of this thesis provides recommendations for future research. These recommendations aim to guide future researchers in contributing to the further development of the design of steel piles fender structures.

- The first recommendation is to extend the NLFE model by including the fluid during the impact simulation. This would enable all degrees of freedom of the ship, resulting in a more realistic simulation of the ship's impact behavior on the fender structure. Currently, it is not well known whether this will lead to lower of higher energy absorption by the fender-soil system. Furthermore, incorporating damping effects of the steel structure, connections, and surrounding soil into the model could provide a more realistic representation of the problem at hand and improve the prediction of the energy absorption of the soil-fender system.
- Secondly, this thesis considered only a single ship geometry from CEMT class IV. It is highly recommended to perform impact simulations using various ship geometries from the same and/or different CEMT classes to study their influence on the energy absorption of the ship during impact events with fender structures. This would provide better insights into the conditions under which a reduction of the ship flexibility factor (C_s) is justified, as the code currently does not offer solid statements on this matter.
- Additionally, fender structures come in different shapes and with varying cross-sectional properties. Extending this research to include different geometries and cross-sectional configurations would lead to broader insights into the interaction between the ship, soil, and fender structure during impact events.
- Finally, extending this research to include different soil layering and types would provide better insights into the interactions among the ship, soil, and fender structure during impact events. It is well known that different soil types exhibit different force-displacement behaviors. Since this problem involves a high level of interaction between the ship, soil, and fender structure, studying these effect could strengthen and expand the conclusions drawn in this thesis.

Bibliography

[1] Rijkswaterstaat. *Richtlijnen Ontwerp Kunstwerken*. Tech. rep. RTD 1001. Rijkswaterstaat Minesterie van Infrastructuur en Waterstaat, 2021.

[2] HTG. *Recommendations of the Committee for Waterfront Structures Harbours and Waterways*. Wilhelm Ernst and Sohn Verlag fur Architektur und Technische, 2015. ISBN: 9783433605202.

[3] Dqfn13. WikiMedia Commons, 2017. URL: https://commons.wikimedia.org/wiki/File:Tesselsebrug,_open,_Alkmaar.jpg. [accessed: 11 October 2024].

[4] Meijer B. "Impact forces on bridge piers in the event of ship collisions". MA thesis. Delft University of Technology, 2020.

[5] Rijkswaterstaat. *Waterway Guidelines 2020*. Rijkswaterstaat Water, Verkeer en Leefomgeving (WVL), 2020. ISBN: 978-90-9033423-3.

[6] Vrijburcht A. *Aanvaarsnelheden Geleidewerken Voorhavens Maasroute*. Tech. rep. Q1815. Delft Hydraulics Laborator, 1994.

[7] Technische Adviescommissie voor de Waterkeringen. *Leidraad Kunstwerken*. DWW-2003-059. Technische Adviescommissie voor de Waterkeringen, 2003. ISBN: 9036955440.

[8] European Committee for Standardization (CEN). *Eurocode 0: Basis of Structural Design*. CEN, 2002.

[9] European Committee for Standardization (CEN). *Eurocode 1: Actions on structures*. CEN, 2002.

[10] European Committee for Standardization (CEN). *Eurocode 3: Design of Steel Structures*. CEN, 2002.

[11] European Committee for Standardization (CEN). *Eurocode 7: Geotechnical Design*. CEN, 2002.

[12] Menard L, Bourdon G, Gambin M. "Methode generale de calcul d'un rideau ou d'un pieu sollicite horizontalement en fonction des resultats pressiometriques". In: *Solssoils* 6 (22/23 1971).

[13] Brinch Hansen J. "The Ultimate resistance of rigid piles against transversal forces". In: *The Danish geotechnical institute* (1961).

[14] American Petroleum Institute. *Geotechnical and Foundation Design Considerations*. Tech. rep. ANSI/API RP 2 GEO. API Publishing Services, 2011.

[15] Reese LC, Cox WR, Koop FD. *Analysis of Laterally Loaded Piles in Sand*. Tech. rep. OTC 2080. Sixth Annual Offshore Technology Conference, 1974.

[16] Lovera A, Ghabezloo S, Sulem J, Randolph MF, Kham M, Palix E. "Pile response to multi-directional lateral loading using P-y curves approach". In: *Géotechnique* 71(4) (2021), pp. 288–298. DOI: https://doi.org/10.1680/jgeot.18.P.297.

[17] Winkler E. "Die Lehre Von der Elastizität und Festigkeit". In: *Lands of the Bohemian Crown: Dominicus* (1867).

[18] Storheim M, Alsos HS, Amdahl J. "Evaluation of Nonlinear Material Behavior for Offshore Structures Subjected to Accidental Actions". In: *Journal of Offshore Mechanics and Arctic Engineering* 140(4) (2018). DOI: https://doi.org/10.1115/1.4038585.

[19] Faridmehr I, Osman MH, Adnan AB, et al. "Correlation between Engineering Stress-Strain and True Stress-Strain Curve". In: *American Journal of Civil Engineering and Architecture* 2(1) (2014), pp. 53–59.

[20] DNV-GL recommended practices. *Determination of structural capacity by non-linear finite element analysis methods*. Vol. RP-C208. DNV GL AS, 2019.

[21] SBRCURnet. *Flexible Dolphins*. SBRCURnet, 2018. ISBN: 978-90-5367-656-1.

[22] *LS-DYNA Theory Manual*. Livermore Software Technology Corporation (LSTC), 2024.

[23] *Ansys Academic Research Mechanical 2024 R2*.

[24] Ye X, Fan W, Sha Y, Hua X, Wu Q, Ren Y. "Fluid-structure interaction analysis of oblique ship-bridge collisions". In: *Engineering Structures* 274 (2022). DOI: https://doi.org/10.1016/j.engstruct.2022.115129.

[25] *LS-DYNA keyword user's manual volume I*. Livermore Software Technology Corporation (LSTC), 2024.

[26] *LS-DYNA keyword user's manual volume II*. Livermore Software Technology Corporation (LSTC), 2024.

[27] European Committee for Standardization (CEN). *Hot rolled products of structural steels - Part 2*. CEN, 2019.

[28] Hughes TJR, Liu WK. "Nonlinear finite element analysis of shells: part I. Three-dimensional shells". In: *Computer Methods in Applied Mechanics and Engineering* 26(3) (1980), pp. 331–362. DOI: https://doi.org/10.1016/0045-7825(81)90121-3.

[29] Prabowo AR, Ridwan R, Moritz B, et al. "Comperative study of shell element formulations as NLFE parameters to forecast structural chrasworthiness". In: *De Gruyter, Curved and Layered Structures* 10 (2023). DOI: https://doi.org/10.1515/cls-2022-0217.

[30] Haufe A, Schweizerhof K, Dubois P. "Properties Limits: Review of Shell Element Formulations". In: *DYNAmore GmbH* (2013). DOI: http://dx.doi.org/10.13140/RG.2.2.28097.35688.

[31] Thomsom WT, Dahleh MD. *Theory of Vibration with Applications - Fifth Edition*. Prentice-Hall, inc. Simon & Schuster, 1998. ISBN: 0-13-651068-X.

[32] Virtanen P, Gommers R, Oliphant TE, et al. "SciPy 1.0: Fundamental algorithms for scientific computing in Python". In: *Nature Methods* 17(3) (2020), pp. 261–272.

A

Theoretical background P-y curves

This appendix provides the theoretical background to calculate the P-y curves for the soil. This research includes two types of P-y relationships: Ménard with Brinch-Hansen and the API-method. For the derivations of the P-y curves used in this research the equations given in this appendix are used.

A.1 MÉNARD WITH BRINCH-HANSEN

Brinch-Hansen uses the following equation to calculate the passive pressure against a pile.

$$\sigma_p = K_q \cdot \sigma\prime_v + K_c \cdot c \tag{A.1}$$

Where,
K_q = resultant earth pressure coefficient caused by the vertical overburden pressure
K_c = resultant earth pressure coefficient caused by the cohesion
$\sigma\prime_v$ = effective vertical pressure
c = cohesion

To calculate the resultant earth pressure coefficients at an arbitrary depth two equations are proposed by Brinch-Hansen.

$$K_q = \frac{K_q^0 + K_q^\infty \cdot \alpha_q \cdot \frac{D}{B}}{1 + \alpha_q \cdot \frac{D}{B}} \tag{A.2}$$

$$K_c = \frac{K_c^0 + K_c^\infty \cdot \alpha_c \cdot \frac{D}{B}}{1 + \alpha_c \cdot \frac{D}{B}} \tag{A.3}$$

Where,
K_q^0, K_c^0 = resultant earth pressure coefficients near the ground surface
K_q^∞, K_c^∞ = resultant earth pressure coefficients at great depth
α_q, α_c = friction angles
D = average depth at the middle of the layer
B = pile diameter

The yet unknown variables can be derived using the equations below. This are all functions dependent on the internal friction angle (ϕ) of the soil.

$$K_q^0 = e^{\left(\frac{\pi}{2}+\phi\right)\cdot\tan\phi} \cdot \cos\phi \cdot \tan\left(\frac{\pi}{4} + \frac{\phi}{2}\right) - e^{\left(-\frac{\pi}{2}+\phi\right)\cdot\tan\phi} \cdot \cos\phi \cdot \tan\left(\frac{\pi}{4} - \frac{\phi}{2}\right) \tag{A.4}$$

$$K_c^0 = \left[e^{\left(\frac{\pi}{2}+\phi\right)\cdot\tan\phi} \cdot \cos\phi \cdot \tan\left(\frac{\pi}{4} + \frac{\phi}{2}\right) - 1\right] \cdot \cot\phi \tag{A.5}$$

$$K_q^\infty = K_c^\infty \cdot K_0 \cdot \tan\phi \tag{A.6}$$

$$K_c^{\infty} = N_c \cdot d_c^{\infty} \tag{A.7}$$

$$d_c^{\infty} = 1.58 + 4.09 \cdot \tan^4 \phi \tag{A.8}$$

$$N_c = \left[e^{\pi \cdot \tan \phi} \cdot \tan^2 \left(\frac{\pi}{4} + \frac{\phi}{2} \right) - 1 \right] \cdot \cot \phi \tag{A.9}$$

$$K_0 = 1 - \sin \phi \tag{A.10}$$

$$\alpha_q = \frac{K_q^0}{K_q^{\infty} - K_q^0} \cdot \frac{K_0 \cdot \sin \phi}{\sin \left(\frac{\pi}{4} + \frac{\phi}{2} \right)} \tag{A.11}$$

$$\alpha_c = \frac{K_c^0}{K_c^{\infty} - K_c^0} \cdot 2 \sin \left(\frac{\pi}{4} + \frac{\phi}{2} \right) \tag{A.12}$$

The Brinch-Hansen method only derives a ultimate limit state since. To include more information about the loading trajectory until the limit stage is reached Brinch-Hansen is often combined with the Ménard method. The Ménard method gives an expression to calculate the modulus of horizontal subgrade reaction. This stiffness factor in combination with the derived limit state using Brinch-Hansen makes it possible to obtain a bi-linear force displacement curve for the soil.

$$\begin{aligned} \frac{1}{k_h} &= \frac{1}{3E_m} \left[1.3 R_0 \left(2.65 \frac{R}{R_0} \right)^{\alpha} + \alpha R \right] \quad \text{for } R \geq R_0 \\ \frac{1}{k_h} &= \frac{2R}{E_m} \frac{4\,(2.65)^{\alpha} + 3\alpha}{18} \quad \text{for } R < R_0 \end{aligned} \tag{A.13}$$

Where,
k_h = modulus of horizontal subgrade reaction
E_m = pressiometer modulus
R_0 = reference radius (3.0 meter)
R = pile radius
α = rheological coefficient

Relations are known to calculate the pressiometer modulus based on the cone resistance (q_c) from CPT data. Since this research only involves sandy soils only the formula related to sand is given.

$$E_{M,sand} = (0.7 - 1) \cdot q_c \tag{A.14}$$

Ménard also proposed values for the rheological coefficient for sandy soils. For over consolidated soil $\alpha = 1/2$ and for normal consolidated soil $\alpha = 1/3$.

A.2 API-METHOD

The API-method makes a clear distinction between the generation of P-y curves for clay and for sand. This research only involves sandy soils. Therefore, only the expressions for P-y curves for sandy soils are given in this appendix.

The API-method starts with the calculating the ultimate soil resistance at shallow and deep depths below the ground surface.

$$p_{us} = (C_1 z + C_2 D)\, \gamma' z \tag{A.15}$$

$$p_{ud} = C_3 D \gamma' z \tag{A.16}$$

Where,
p_{us} = ultimate soil resistance at shallow depth
p_{ud} = ultimate soil resistance at deep depths
D = pile diameter
γ' = effective volume weight
z = depth below ground surface
C_i = coefficients as function of the internal friction angle

The ultimate soil resistance is dependent on some coefficients based on the internal friction angle (ϕ) of the soil.

$$C_1 = \frac{(\tan\beta)^2 \tan\alpha}{\tan(\beta - \phi')} + K_o \times \left[\frac{\tan\phi' \times \sin\beta}{\cos\alpha \times \tan(\beta - \phi')} + \tan\beta \times (\tan\phi' \times \sin\beta - \tan\alpha) \right] \tag{A.17}$$

$$C_2 = \frac{\tan\beta}{\tan(\beta - \phi')} - K_a \tag{A.18}$$

$$C_3 = K_a \times \left[(\tan\beta)^8 - 1 \right] + K_o \times \tan\phi' \times (\tan\beta)^4 \tag{A.19}$$

$$\alpha = \frac{\phi'}{2} \tag{A.20}$$

$$\beta = 45 + \frac{\phi'}{2} \tag{A.21}$$

$$K_o = 0.4 \tag{A.22}$$

$$K_a = \frac{1 - \sin\phi'}{1 + sin\phi'} \tag{A.23}$$

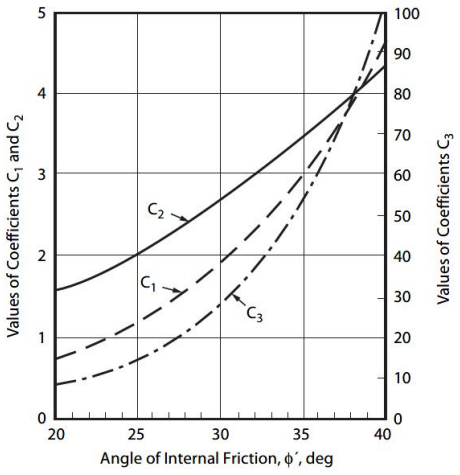

Figure A.1: Coefficients as function of ϕ'

At every depth of interest the minimum value of the ultimate soil resistance should be applied. The API-method proposed a tangent hyperbolic curve as function of the lateral displacement as shown below.

$$p = A \times p_u \tanh\left[\frac{k \times z}{A \times p_u} y \right] \tag{A.24}$$

Where,
$p_u = \min(p_{us}, p_{ud})$
k = soil stiffness
y = lateral displacement
$A = \left(3.0 - 0.8\frac{z}{D}\right) \geq 0.9$

For the soil stiffness the API prescribes the following values dependent on the ineternal friction angle of the soil.

Table A.1: Soil stiffness according to API-method

φ' [^{o}]	k [kN/m^3]
25	5400
30	11000
35	22000
40	45000

B

Model Geometries

This appendix provides the model geometries of the non-linear finite element models. First, the model geometry of the ship's bow structure is presented in section B.1. Section B.2 presents the model geometry of the fender structure.

B.1 GEOMETRY SHIP'S BOW STRUCTURE

The figures presented in this section show the the geometry of the ship's bow structure. Geometrical and structural data are extracted from B. Meijer's thesis work [4]. Elements are colored based on their plate thickness.

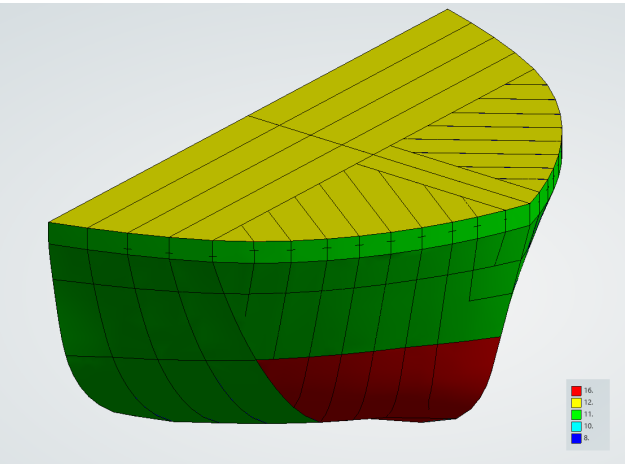

Figure B.1: 3D view: ship structure

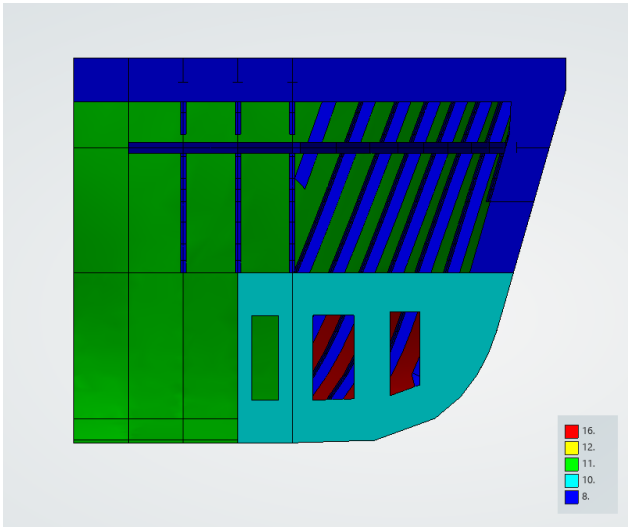

Figure B.2: Cross section view central axis: ship structure

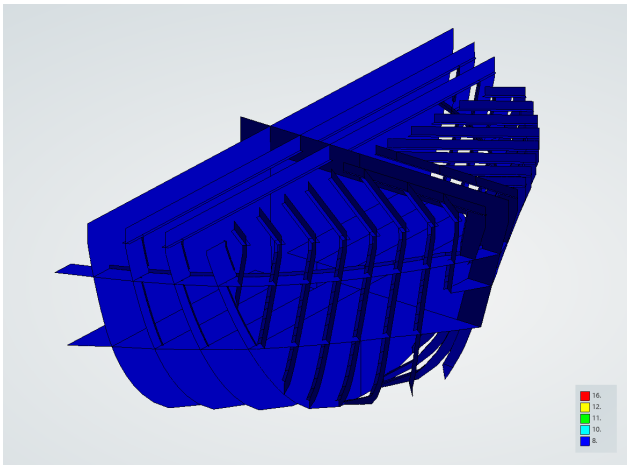

Figure B.3: Element thickness 8 mm: ship structure

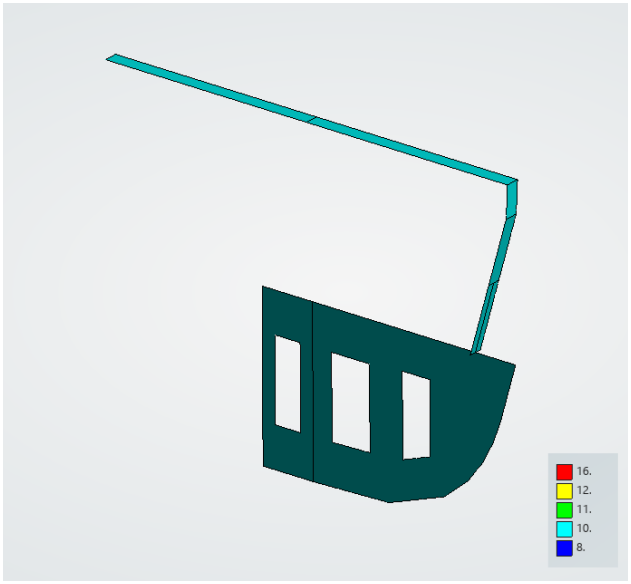

Figure B.4: Element thickness 10 mm: ship structure

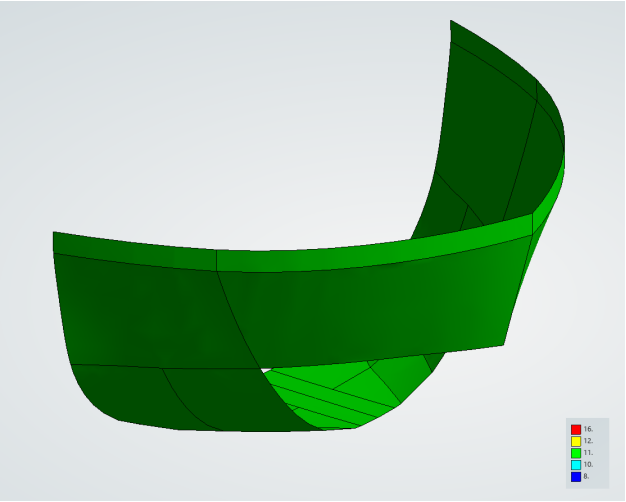

Figure B.5: Element thickness 11 mm: ship structure

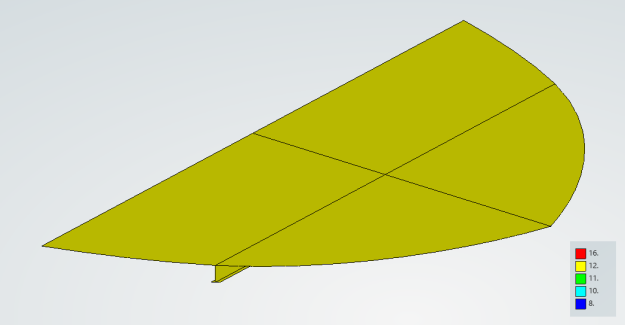

Figure B.6: Element thickness 12 mm: ship structure

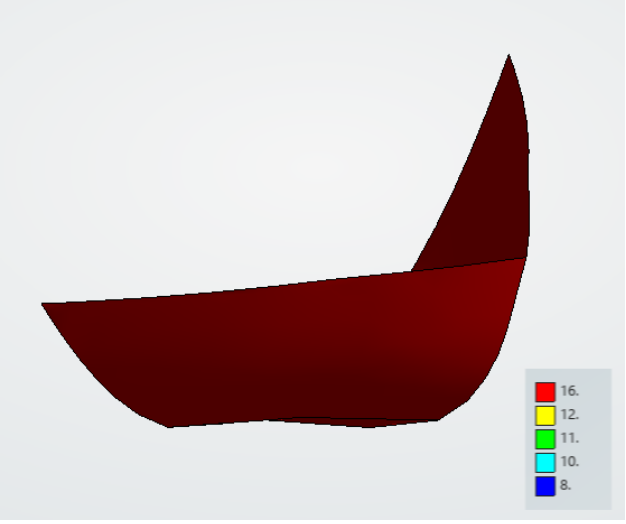

Figure B.7: Element thickness 16 mm: ship structure

B.2 GEOMETRY FENDER STRUCTURE

The figures presented in this section show the geometry of the fender structure. Geometrical and structural data are extracted from technical drawings available internally at IV. Elements are colored according to their plate thickness.

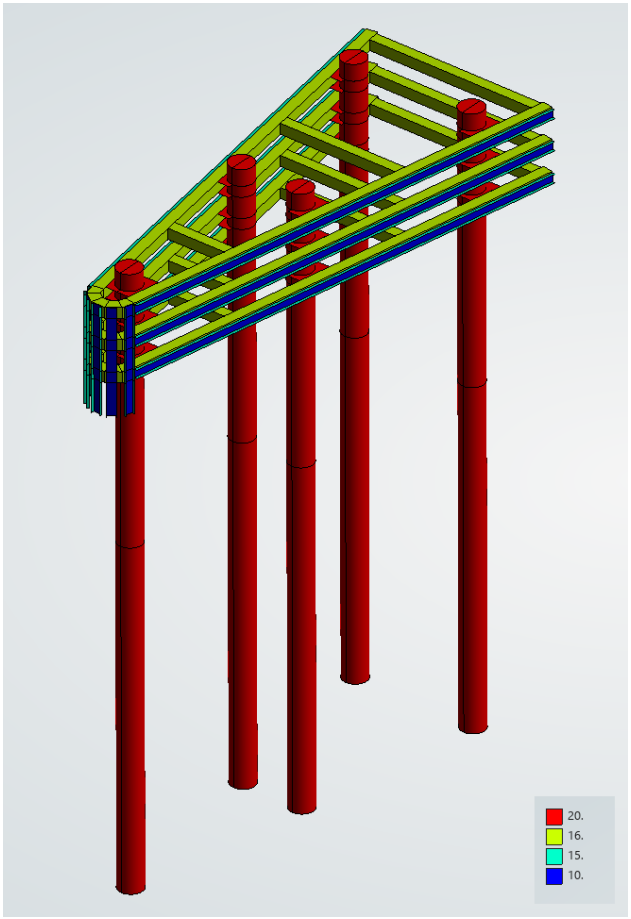

Figure B.8: 3D view: fender structure

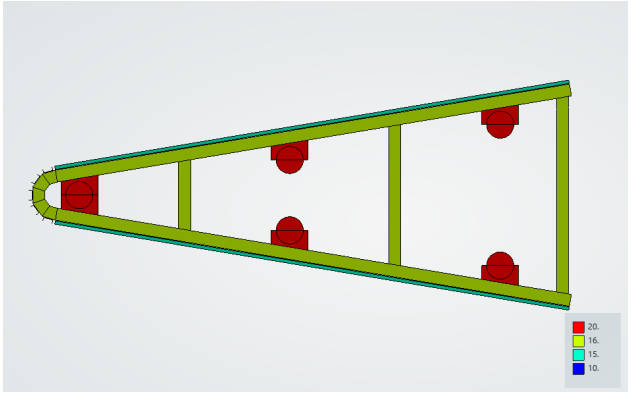

Figure B.9: Top view: fender structure

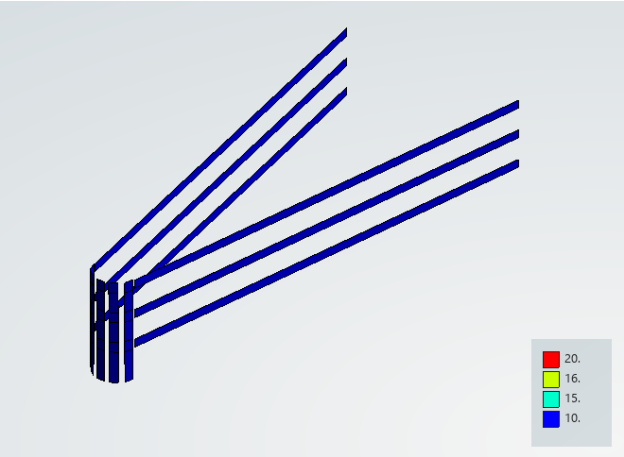

Figure B.10: Element thickness 10 mm: fender structure

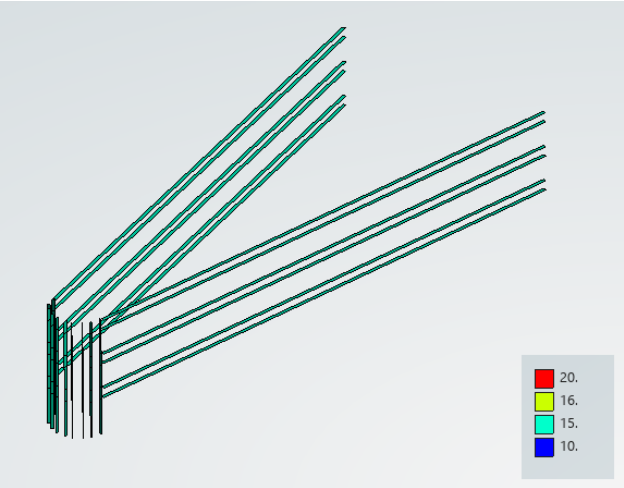

Figure B.11: Element thickness 15 mm: fender structure

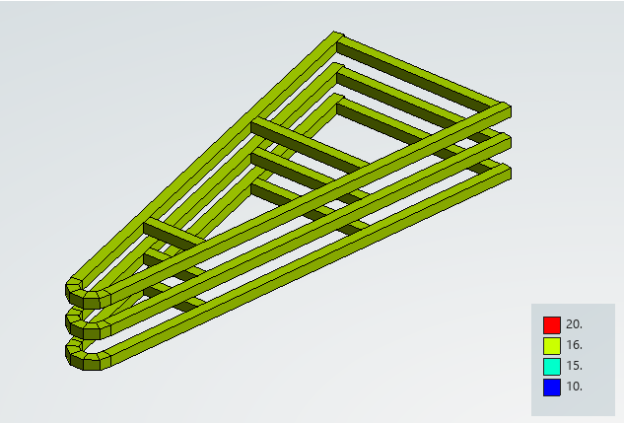

Figure B.12: Element thickness 16 mm: fender structure

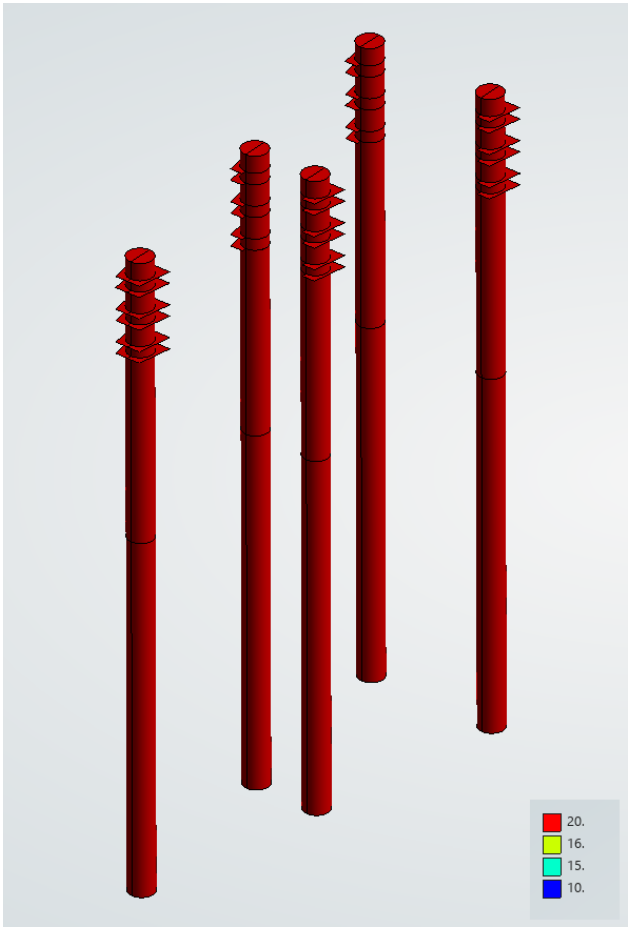

Figure B.13: Element thickness 20 mm: fender structure

C

Derivation P-y curves

This appendix only shows the procedure of deriving the P-y curves used in this research. No equations or calculations are shown but derived values can be reproduced by using the equations given in appendix A.

Soil properties are extracted based on available CPT data from the fender structure at interest. The most important values are summarized in figure C.1. From this figure, it can be seen that soil layers are combined and values are averaged. In total 5 unique soil layers are included.

soil layer		w.r.t. reference [m]			q_c [MPa]	γ_{dry} [kN/m^3]	γ_{sat} [kN/m^3]	γ_{eff} [kN/m^3]	Φ [°]	δ [°]	c [kN/m^2]
-	silt	river bed	to	0.0	-	-	-		-	-	-
1	sand	0.0	to	-3.5	10.0	18.0	20.0	10.0	31.0	20.7	0.0
2	sand	-3.5	to	-6.5	8.0	18.0	20.0	10.0	31.0	20.7	0.0
3	sand	-6.5	to	-9.5	2.0	17.0	19.0	9.0	27.0	18.0	0.0
4	sand	-9.5	to	-11.5	15.0	18.0	20.0	10.0	32.5	21.7	0.0
5	sand	-11.5	to	-19.0	8.0	18.0	20.0	10.0	31.0	20.7	0.0

Figure C.1: CPT-based soil properties

Where,
q_c = cone resistance
γ_{dry} = dry volume weight of soil
γ_{sat} = saturated volume weight of soil
γ_{eff} = effective volume weight
ϕ = internal friction angle
δ = interface friction angle
c = cohesion of soil

Based on this soil properties force-displacement relationships are defined based on two different theories. First the derivation of bi-linear P-y curves using Ménard with Brinch-Hansen is given followed by the tangent hyperbolic P-y curves using the API-method.

C.1 MÉNARD WITH BRINCH-HANSEN: BI-LINEAR P-Y CURVES

First, the Brinch-Hansen pressure coefficients are derived at ground level and at great depth. Calculated values are summarized in figure C.2.

soil layer	K_q^0 [-]	K_c^0 [-]	K_q^∞ [-]	K_c^∞ [-]	d_c^∞ [-]	N_c [-]	K_0 [-]	α_q [-]	α_c [-]
1	5.13	7.30	20.12	69.04	2.11	32.67	0.48	0.10	0.21
2	5.13	7.30	20.12	69.04	2.11	32.67	0.48	0.10	0.21
3	3.80	6.11	12.36	44.43	1.86	23.94	0.55	0.13	0.27
4	5.76	7.85	24.59	83.43	2.25	37.02	0.46	0.09	0.18

Figure C.2: Brinch-Hansen coefficients

Filling in the formulas for the pressure coefficients at arbitrary depth the passive pressure (σ_p) against the pile can be derived. Values at the middle depth of each soil layer are given in figure C.3.

soil layer	D [m]	K_q [-]	K_c [-]	σ'_v [kN/m^2]	σ_p [kN/m^2]
1	1.75	7.89	27.13	17.50	138.0
2	5.00	11.00	42.79	50.00	550.0
3	8.00	8.73	34.50	78.50	685.3
4	10.50	16.01	61.90	102.00	1633.1

Figure C.3: Brinch-Hansen passive pressure

Based on the CPT data the modulus of horizontal subgrade reaction can be derived using Ménard's established relation. The values found are given in C.4.

soil layer	E_m [kPa]	α [-]	k_h [kN/m^3]
1	8.50	0.33	35842
2	6.80	0.33	28674
3	1.70	0.33	7168
4	12.75	0.33	53763

Figure C.4: Ménard modulus of horizontal subgrade reaction

To construct the bi-linear curves based on the derived values from Brinch-Hansen and Ménard a value for the ultimate soil resistance (p_u) needs to be derived. This can be done by multiplying the passive pressure (σ_p) with the pile diameter. Furthermore, the modulus of subgrade reaction may be multiplied by a Dynamic Amplification Factor (DAF) to account for short-term dynamic loading effects. This results in the values for k_{dynamic}. The lateral displacement (u) at which the transition between elastic and plastic soil behavior takes place can be found by: $u = p_u / k_{\text{dynamic}}$. Values are shown in figure C.5

soil layer	p_u [kN/m]	DAF [-]	$k_{dynamic}$ [kN/m^2]	u [m]
1	105.2	3.0	81935	0.0013
2	419.1	3.0	65548	0.0064
3	522.2	3.0	16387	0.0319
4	1244.4	3.0	122903	0.0101

Figure C.5: Bi-linear curve parameters

Figure C.6 shows the derived bi-linear P-y curves based on Ménard with Brinch-Hansen.

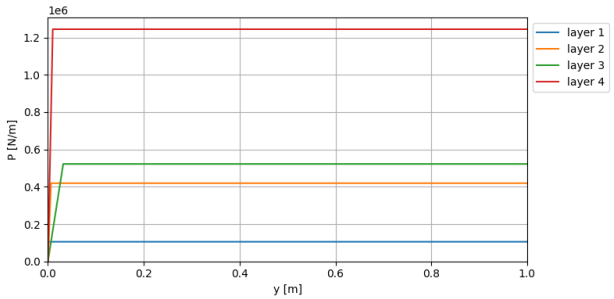

Figure C.6: Bi-linear uni-directional P-y curves

C.2 API-METHOD: TANGENT HYPERBOLIC P-Y CURVES

First, the coefficients to calculate the ultimate soil resistance are derived. Calculated values for the different soil layers are summarized in figure C.7.

soil layer	α [rad]	β [rad]	k [kN/m^3]	K_0 [-]	K_a [-]	C_1 [-]	C_2 [-]	C_3 [-]
-	-	-	-	-	-	-	-	-
1	0.27	1.1	13200	0.4	0.3	2.1	2.8	32.5
2	0.27	1.1	13200	0.4	0.3	2.1	2.8	32.5
3	0.24	1.0	7640	0.4	0.4	1.5	2.3	20.0
4	0.28	1.1	16500	0.4	0.3	2.4	3.0	39.2
5	0.27	1.1	13200	0.4	0.3	2.1	2.8	32.5

Figure C.7: Coefficients ultimate soil resistance

The ultimate soil resistance over depth is calculated and a graph is shown in figure C.8. The embedment length of the pile is also shown in this figure. Furthermore, separation lines between the different soil layers are shown by the black dashed lines. The fifth soil layer can be neglected because of the embedment length of the pile.

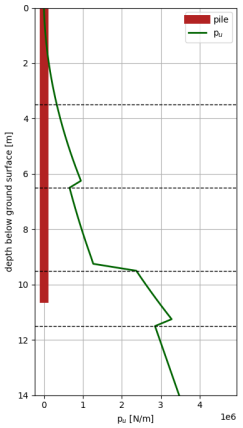

Figure C.8: Ultimate soil resistance

Figure C.9 summarizes the applied parameters used for the calculation of the tangent hyperbolic P-y curves. Note that, the values for the soil stiffness (k) are linear interpolated from the table given in appendix A. For the value of the ultimate soil resistance (p_u) and the load factor (A) values at the middle height (z) of the soil layer are used.

soil layer	z [m]	k [kN/m^3]	p_u [kN/m]	A [-]
1	1.75	13200	101.4	1.20
2	5.00	13200	629.0	0.90
3	8.00	7640	967.5	0.90
4	10.50	16500	2870.2	0.90

Figure C.9: Tangent hyperbolic curve parameters

Substitution of the parameters into the formula for the tangent hyperbolic curves and evaluating for a range of values for the lateral displacement (y) results into the P-y curves shown in figure C.10.

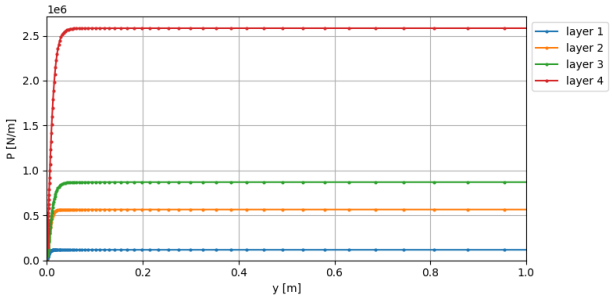

Figure C.10: API-method: tangent hyperbolic uni-directional P-y curves

D

Derivation Material Models

This appendix describes the numerical derivation of the steel material models.

Structural steel S235
For structural steel quality class S235 the recommended values from the DNV-RP C2028 and the European standard EN 10025 − 2 are given in figure D.1.

DNV-RP C208_2019+A1_2022 Table 4-2 Proposed properties for S235 steels (true stress strain)			
		t≤16	16<t≤40
E	[MPa]	210000	210000
σ_prop	[MPa]	211.7	202.7
σ_yield	[MPa]	236.2	226.1
σ_yield,2	[MPa]	243.4	233.2
ε_prop	[-]	0.0010	0.0010
ε_p,y1	[-]	0.004	0.004
ε_p,y2	[-]	0.02	0.02
K	[MPa]	520	520
n	[-]	0.166	0.166

EN 10025-2:2019 (E) Table 6 - Mechanical properties			
		t ≤ 16	16 < t ≤ 40
σ_ult	[MPa]	360	358.7
ε_fr	[-]	0.24	0.24

Figure D.1: Material properties S235

Figure D.2 shows the numerical values for the full length of the true stress-strain curve. For the calculations of the values the curve is subdivided into five parts shown in the most left column. Part 0 till 3 can be constructed with linear curves using the the values given in table D.1. Part 4 is the power law curve part and can be calculated using (2.10) from section 2.4.1. The end point of the fourth part is defined at the value for the total strain for which the power law curve equals the ultimate tensile strength (σ_{ult}). Finally, part 5 follows a linear curve with as end point the fractile strain value (ε_{fr}). A slope of 1/10000 the Young's modulus is applied to the stress parameter in the fifth part. This to avoid convergence issues while numerically solving the problem.

Note that in figure D.2 both total strain and effective plastic strain values are given. This is because, LS-DYNA requires as input the true stress-effective plastic strain relation.

Part	Total strain	Effective plastic strain t ≤ 16	Stress t ≤ 16	Effective plastic strain 16 < t ≤ 40	Stress 16 < t ≤ 40
0	0.0000	0.0000	0.0	0.0000	0.0
1	0.0010	0.0000	211.7	0.0000	202.7
2	0.0040	0.0030	236.2	0.0030	226.1
3	0.0200	0.0190	243.4	0.0190	233.2
4	0.0258	0.0248	262.1	0.0248	255.4
4	0.0316	0.0306	275.9	0.0307	270.7
4	0.0374	0.0364	286.8	0.0365	282.6
4	0.0432	0.0422	296.0	0.0423	292.5
4	0.0491	0.0481	304.0	0.0481	300.9
4	0.0549	0.0539	311.0	0.0539	308.3
4	0.0607	0.0597	317.3	0.0597	314.8
4	0.0665	0.0655	323.0	0.0655	320.8
4	0.0723	0.0713	328.3	0.0713	326.2
4	0.0781	0.0771	333.2	0.0772	331.2
4	0.0839	0.0829	337.7	0.0830	335.9
4	0.0897	0.0887	342.0	0.0888	340.3
4	0.0956	0.0945	346.0	0.0946	344.4
4	0.1014	0.1004	349.7	0.1004	348.2
4	0.1072	0.1062	353.3	0.1062	351.9
4	0.1130	0.1120	356.7	0.1120	355.4
5	0.1188	0.1178	360.0	0.1178	358.7
5	0.2400	0.2390	362.5	0.2390	361.2

Figure D.2: Numerical values S235

Structural steel S355

The same methodology is applied in deriving the numerical values for the true stress-strain relations for structural steel S355. Figure D.3 shows the recommended values from the standards. Figure D.4 gives the numerical values.

DNV-RP C208_2019+A1_2022 Table 4-4 Proposed properties for S355 steels (true stress strain)			
		t ≤ 16	16 < t ≤ 40
E	[MPa]	210000	210000
σ_prop	[MPa]	320	311
σ_yield	[MPa]	357	346.9
σ_yield,2	[MPa]	363.3	353.1
ε_prop	[-]	0.0015	0.0015
ε_p,y1	[-]	0.004	0.004
ε_p,y2	[-]	0.015	0.015
K	[MPa]	740	740
n	[-]	0.166	0.166

EN 10025-2:2019 (E) Table 6 - Mechanical properties			
		t ≤ 16	16 < t ≤ 40
σ_ult	[MPa]	470	467.4
ε_fr	[-]	0.2	0.2

Figure D.3: Material properties S355

Part	Total strain	Effective plastic strain t ≤ 16	Stress t ≤ 16	Effective plastic strain 16 < t ≤ 40	Stress 16 < t ≤ 40
0	0.0000	0.0000	0.0	0.0000	0.0
1	0.0015	0.0000	320.0	0.0000	311.0
2	0.0040	0.0025	357.0	0.0025	346.9
3	0.0150	0.0135	363.3	0.0135	353.1
4	0.0180	0.0165	375.4	0.0165	366.9
4	0.0210	0.0195	385.9	0.0195	378.5
4	0.0240	0.0225	395.0	0.0225	388.5
4	0.0270	0.0255	403.2	0.0256	397.4
4	0.0301	0.0285	410.7	0.0286	405.4
4	0.0331	0.0315	417.5	0.0316	412.7
4	0.0361	0.0345	423.8	0.0346	419.3
4	0.0391	0.0376	429.7	0.0376	425.5
4	0.0421	0.0406	435.2	0.0406	431.3
4	0.0451	0.0436	440.4	0.0436	436.7
4	0.0481	0.0466	445.3	0.0466	441.8
4	0.0511	0.0496	449.9	0.0496	446.6
4	0.0541	0.0526	454.3	0.0526	451.1
4	0.0571	0.0556	458.5	0.0557	455.5
4	0.0602	0.0586	462.5	0.0587	459.6
4	0.0632	0.0616	466.3	0.0617	463.6
5	0.0662	0.0646	470.0	0.0647	467.4
5	0.2000	0.1985	472.8	0.1985	470.2

Figure D.4: Numerical values S355

E

Description Simplified Dynamic Model

E.1 GEOMETRY

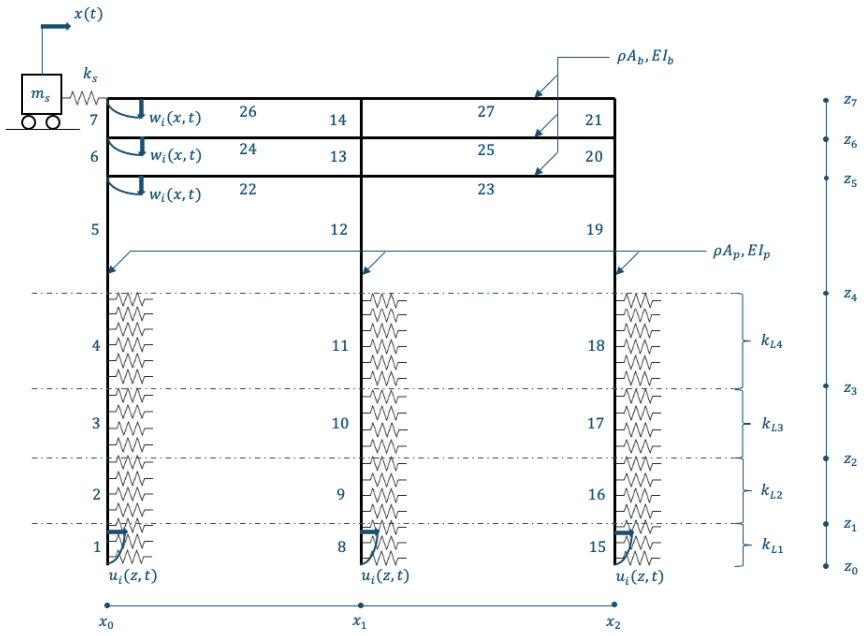

Figure E.1: Semi-numerical model: geometry

E.2 BOUNDARY CONDITIONS

Boundary condition at z_0:

$$\begin{aligned} u_i(z_0,t) &= 0 \\ \frac{\partial^2 u_i(z_0,t)}{\partial z^2} &= 0 \end{aligned} \tag{E.1}$$

Where:

$$i = \begin{cases} 1 & \text{, at } x_0 \\ 8 & \text{, at } x_1 \\ 15 & \text{, at } x_2 \end{cases}$$

Boundary condition at z_1:

$$\begin{aligned} u_i(z_1,t) &= u_j(z_1,t) \\ \frac{\partial u_i(z_1,t)}{\partial z} &= \frac{\partial u_j(z_1,t)}{\partial z} \\ EI\frac{\partial^2 u_i(z_1,t)}{\partial z^2} &= EI\frac{\partial^2 u_j(z_1,t)}{\partial z^2} \\ EI\frac{\partial^3 u_i(z_1,t)}{\partial z^3} &= EI\frac{\partial^3 u_j(z_1,t)}{\partial z^3} \end{aligned} \tag{E.2}$$

Where:

$$i = \begin{cases} 1 & \text{, at } x_0 \\ 8 & \text{, at } x_1 \\ 15 & \text{, at } x_2 \end{cases} \qquad j = \begin{cases} 2 & \text{, at } x_0 \\ 9 & \text{, at } x_1 \\ 16 & \text{, at } x_2 \end{cases}$$

Boundary condition at z_5:
At x_0:

$$\begin{aligned} u_5(z_5,t) &= u_6(z_5,t) \\ w_{22}(x_0,t) &= 0 \\ \frac{\partial u_5(z_5,t)}{\partial z} &= \frac{\partial u_6(z_5,t)}{\partial z} \\ \frac{\partial u_5(z_5,t)}{\partial z} &= \frac{\partial w_{22}(x_0,t)}{\partial x} \\ -EI_b\frac{\partial^2 w_{22}(x_0,t)}{\partial x^2} - EI_p\frac{\partial^2 u_6(z_5,t)}{\partial z^2} + EI_p\frac{\partial^2 u_5(z_5,t)}{\partial z^2} &= 0 \end{aligned} \tag{E.3}$$

At x_1:

$$\begin{aligned} u_{12}(z_5,t) &= u_{13}(z_5,t) \\ w_{22}(x_1,t) &= 0 \\ w_{23}(x_1,t) &= 0 \\ \frac{\partial u_{12}(z_5,t)}{\partial z} &= \frac{\partial u_{13}(z_5,t)}{\partial z} \\ \frac{\partial u_{12}(z_5,t)}{\partial z} &= \frac{\partial w_{22}(x_1,t)}{\partial x} \\ \frac{\partial u_{12}(z_5,t)}{\partial z} &= \frac{\partial w_{23}(x_1,t)}{\partial x} \\ EI_p\frac{\partial^2 u_{12}(z_5,t)}{\partial z^2} - EI_p\frac{\partial^2 u_{13}(z_5,t)}{\partial z^2} + EI_b\frac{\partial^2 w_{22}(x_1,t)}{\partial x^2} - EI_b\frac{\partial^2 w_{23}(x_1,t)}{\partial x^2} &= 0 \end{aligned} \tag{E.4}$$

At x_2:

$$\begin{aligned} u_{19}(z_5,t) &= u_{20}(z_5,t) \\ w_{23}(x_2,t) &= 0 \\ \frac{\partial u_{19}(z_5,t)}{\partial z} &= \frac{\partial u_{20}(z_5,t)}{\partial z} \\ \frac{\partial u_{19}(z_5,t)}{\partial z} &= \frac{\partial w_{23}(x_2,t)}{\partial x} \\ EI_b\frac{\partial^2 w_{23}(x_2,t)}{\partial x^2} + EI_p\frac{\partial^2 u_{19}(z_5,t)}{\partial z^2} - EI_p\frac{\partial^2 u_{20}(z_5,t)}{\partial z^2} &= 0 \end{aligned} \tag{E.5}$$

At x:

$$\begin{aligned} u_5(z_5,t) &= u_{12}(z_5,t) \\ u_5(z_5,t) &= u_{19}(z_5,t) \\ \frac{\partial^3 u_5(z_5,t)}{\partial z^3} + \frac{\partial^3 u_{12}(z_5,t)}{\partial z^3} + \frac{\partial^3 u_{19}(z_5,t)}{\partial z^3} - \frac{\partial^3 u_6(z_5,t)}{\partial z^3} - \frac{\partial^3 u_{13}(z_5,t)}{\partial z^3} - \frac{\partial^3 u_{20}(z_5,t)}{\partial z^3} &= -\frac{\omega^2 m_b u_5(z_5,t)}{EI_p} \end{aligned} \tag{E.6}$$

Boundary condition at z_7:
At x_0:

$$\begin{aligned} w_{26}(x_0,t) &= 0 \\ \frac{\partial u_7(z_7,t)}{\partial z} &= \frac{\partial w_{26}(x_0,t)}{\partial x} \\ -EI_b \frac{\partial^2 w_{26}(x_0,t)}{\partial x^2} + EI_p \frac{\partial^2 u_7(z_7,t)}{\partial z^2} &= 0 \end{aligned} \tag{E.7}$$

At x_1:

$$\begin{aligned} w_{26}(x_1,t) &= 0 \\ w_{27}(x_1,t) &= 0 \\ \frac{\partial u_{14}(z_7,t)}{\partial z} &= \frac{\partial w_{26}(x_1,t)}{\partial x} \\ \frac{\partial w_{26}(x_1,t)}{\partial x} &= \frac{\partial w_{27}(x_1,t)}{\partial x} \\ EI_p \frac{\partial^2 u_{14}(z_7,t)}{\partial z^2} + EI_b \frac{\partial^2 w_{26}(x_1,t)}{\partial x^2} - EI_b \frac{\partial^2 w_{27}(x_1,t)}{\partial x^2} &= 0 \end{aligned} \tag{E.8}$$

At x_2:

$$\begin{aligned} w_{27}(x_2,t) &= 0 \\ \frac{\partial u_{21}(z_7,t)}{\partial z} &= \frac{\partial w_{27}(x_2,t)}{\partial x} \\ EI_b \frac{\partial^2 w_{27}(x_2,t)}{\partial x^2} + EI_p \frac{\partial^2 u_{21}(z_7,t)}{\partial z^2} &= 0 \end{aligned} \tag{E.9}$$

At x:

$$\begin{aligned} u_7(z_7,t) &= u_{14}(z_7,t) \\ u_7(z_7,t) &= u_{21}(z_7,t) \\ \frac{\partial^3 u_7(z_7,t)}{\partial z^3} + \frac{\partial^3 u_{14}(z_7,t)}{\partial z^3} + \frac{\partial^3 u_{21}(z_7,t)}{\partial z^3} &= -\frac{\omega^2 m_b u_7(z_7,t)}{EI_p} \end{aligned} \tag{E.10}$$

F

Simulation results sensitivity analysis: ship structure

Simulation A1	
t = 0.0 s	
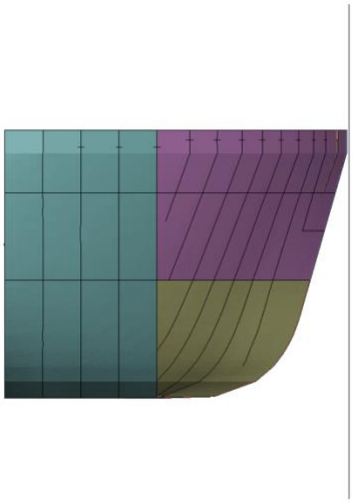	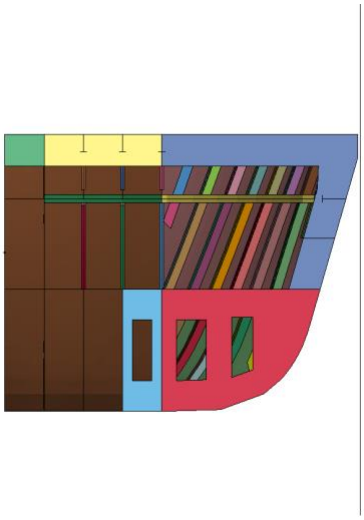
t = 0.25 s	
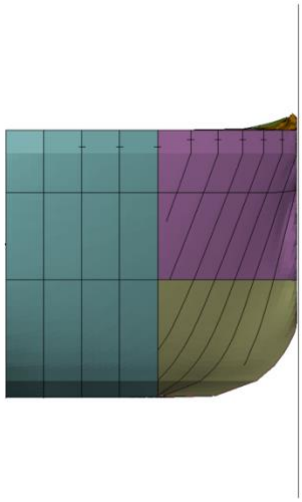	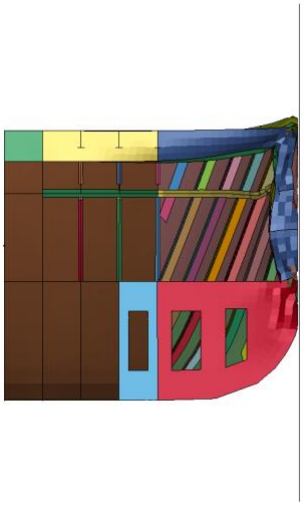
t = 0.50 s	
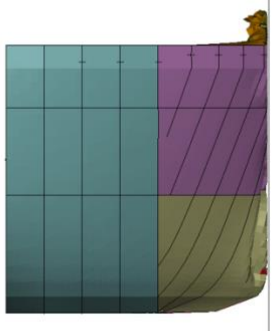	

t = 0.75 s	
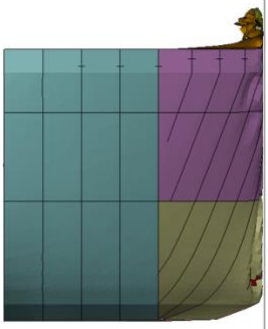	
t = 1.0 s	
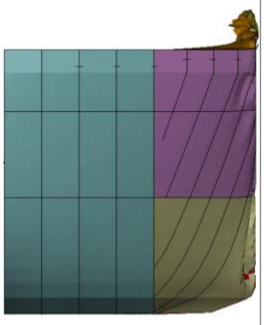	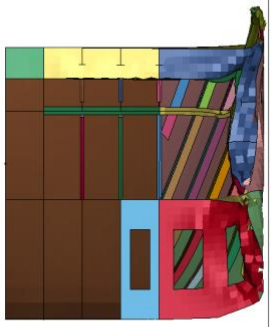

Simulation A2	
t = 0.0 s	
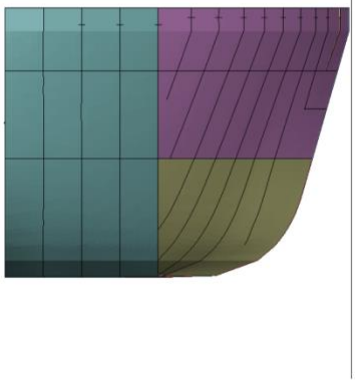	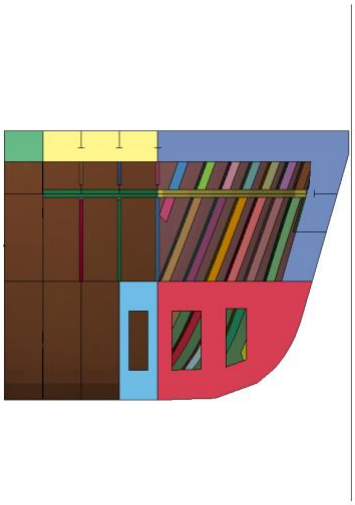
t = 0.25 s	
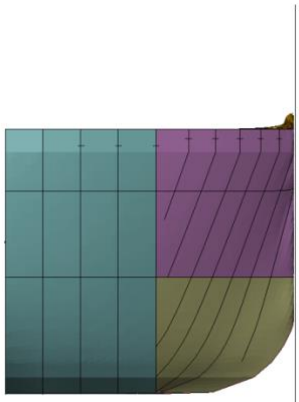	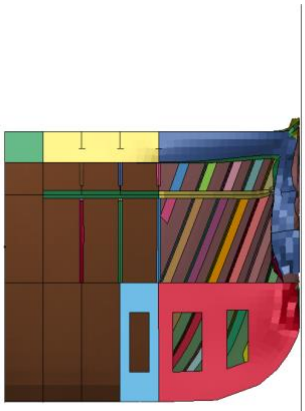
t = 0.50 s	
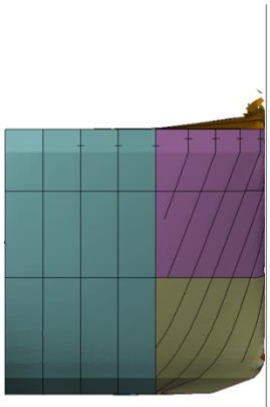	

t = 0.75 s	
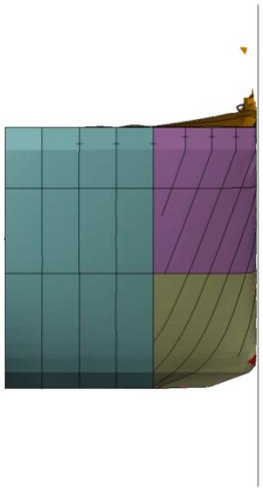	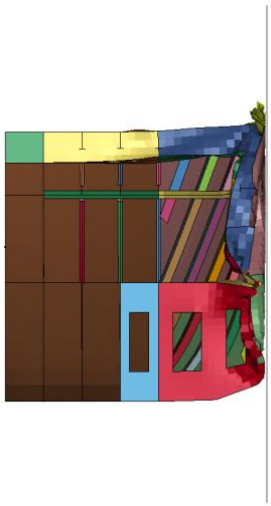
t = 1.0 s	
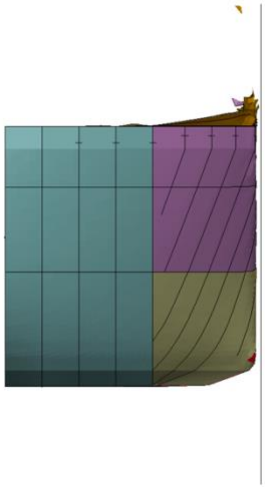	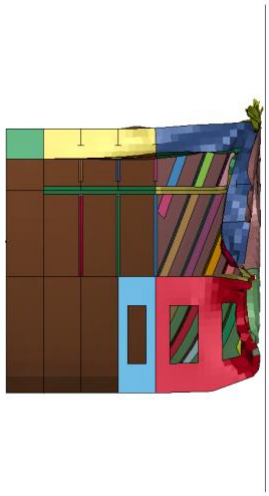

Simulation B1	
t = 0.0 s	
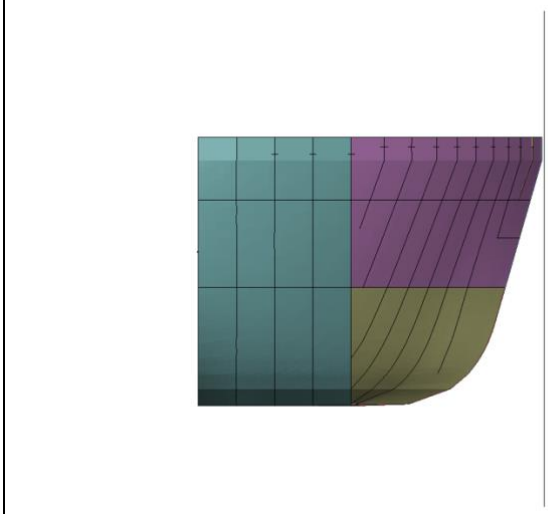	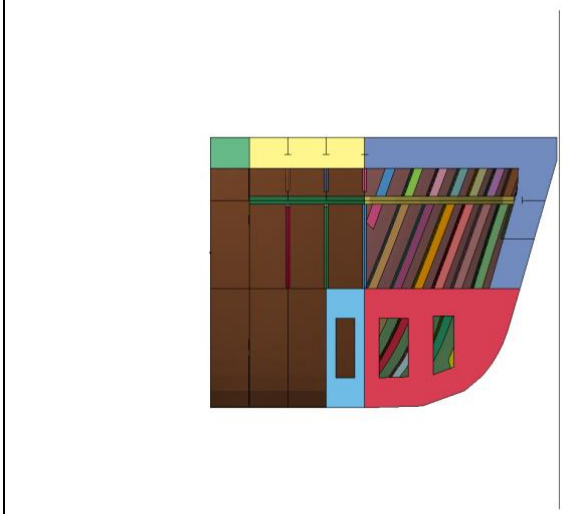
t = 0.25 s	
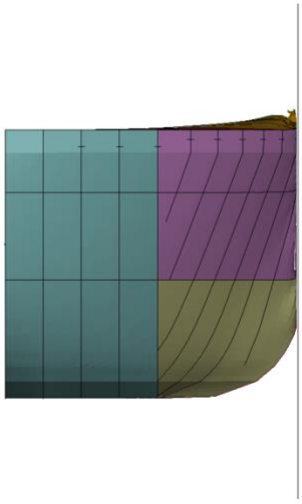	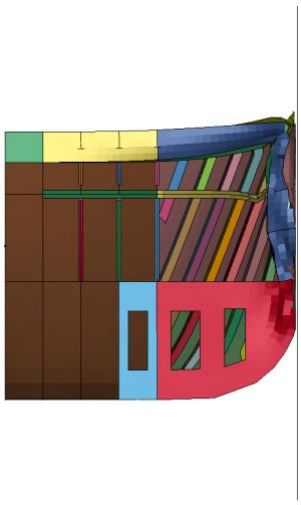
t = 0.50 s	
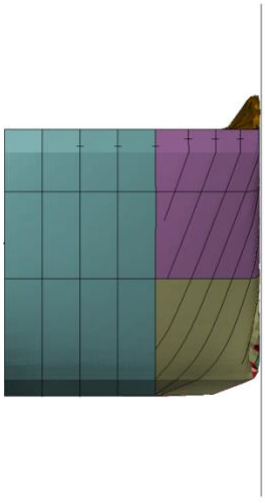	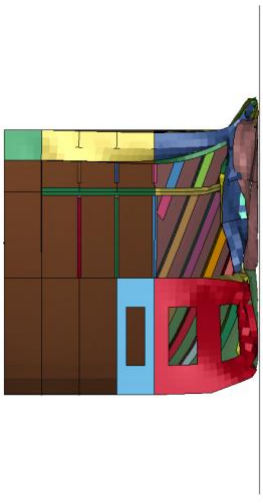

t = 0.75 s	
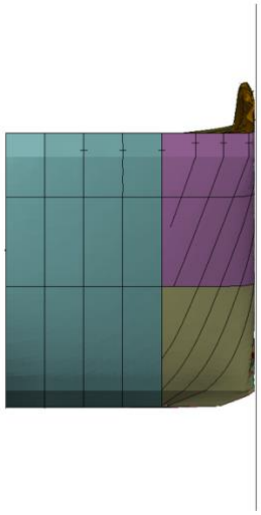	
t = 1.0 s	
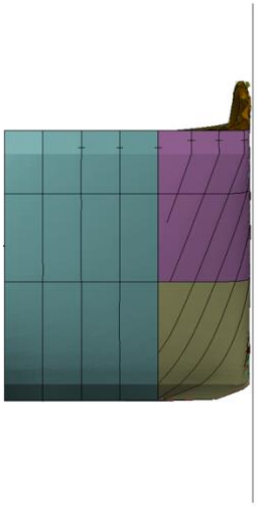	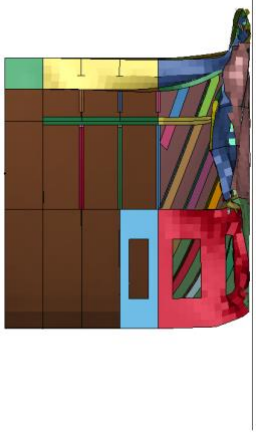

Simulation B2	
t = 0.0 s	
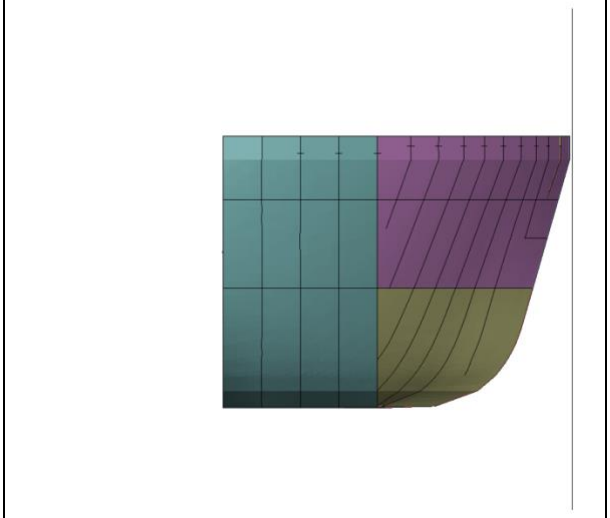	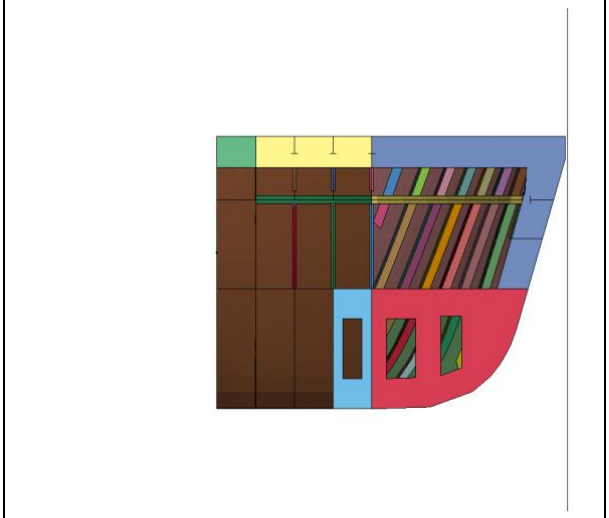
t = 0.25 s	
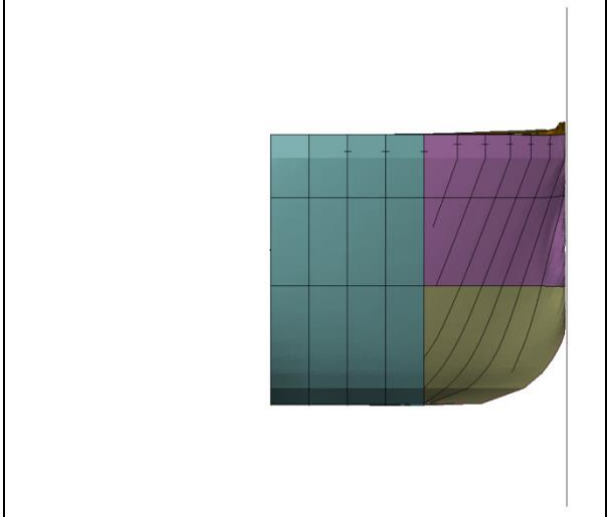	
t = 0.50 s	
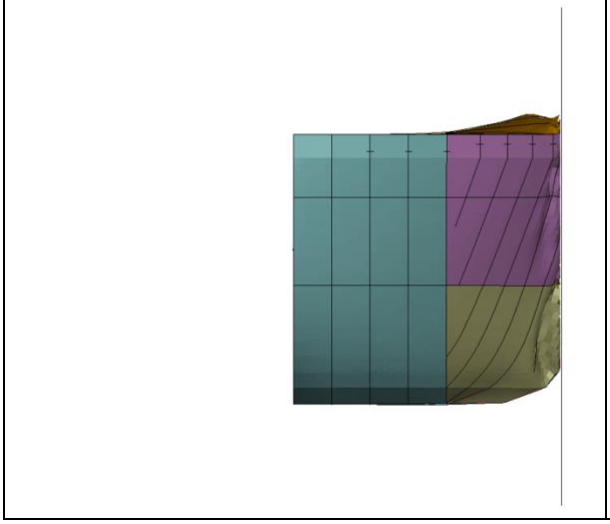	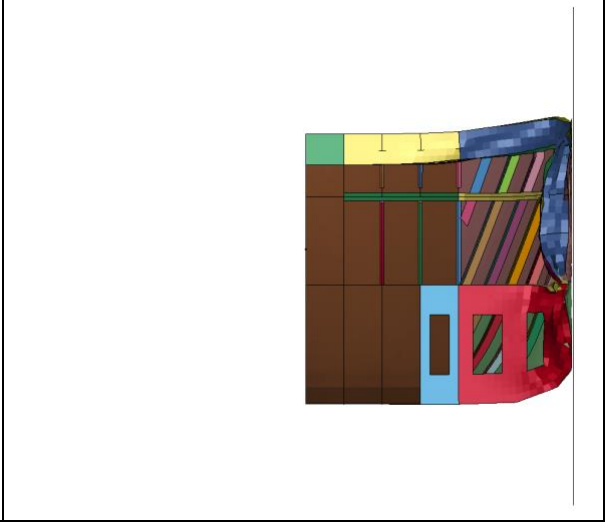

t = 0.75 s	
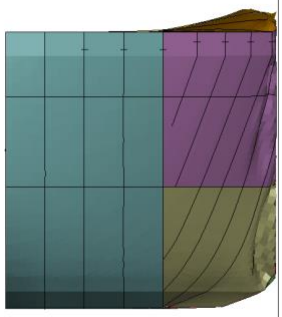	
t = 1.0 s	
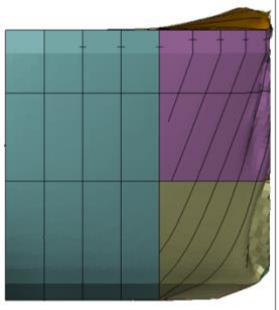	

Simulation C1	
t = 0.0 s	
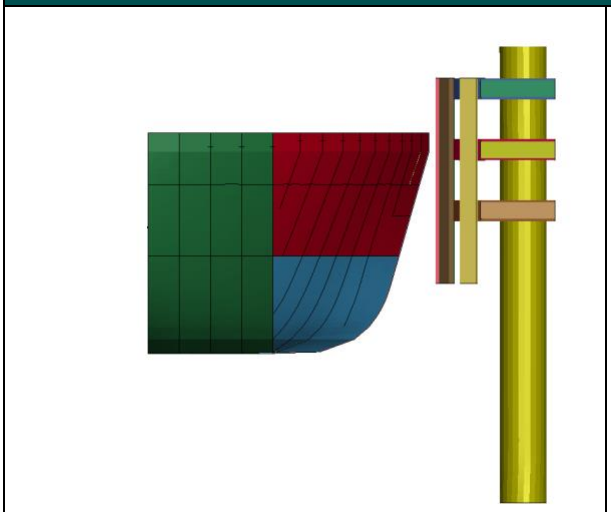	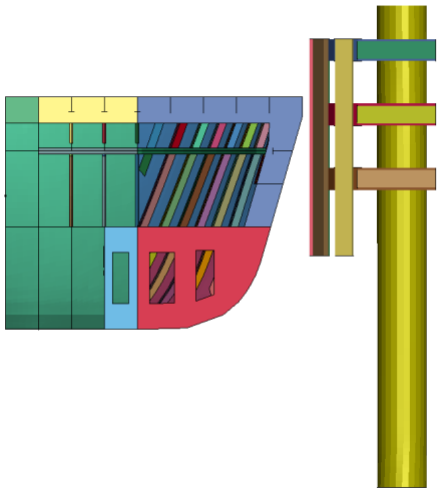
t = 0.25 s	
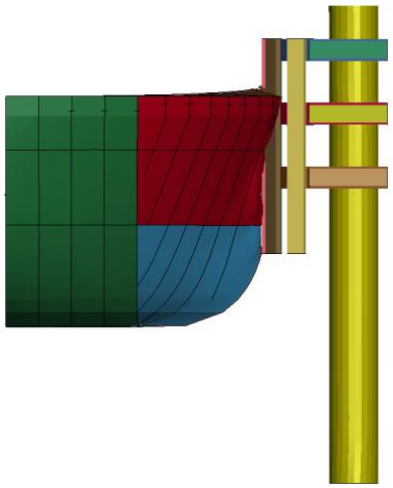	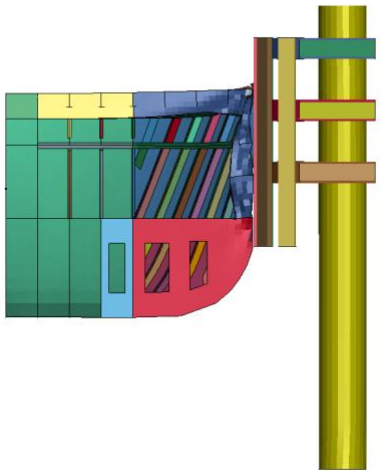
t = 0.50 s	
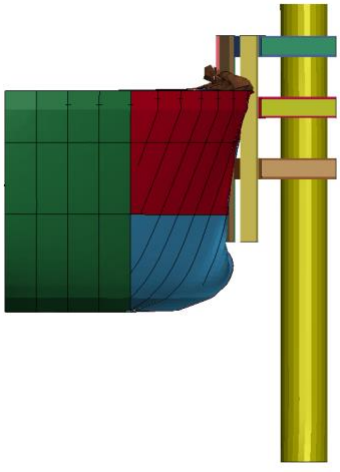	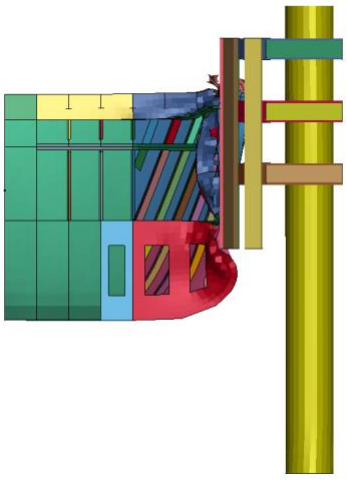

t = 0.75 s	
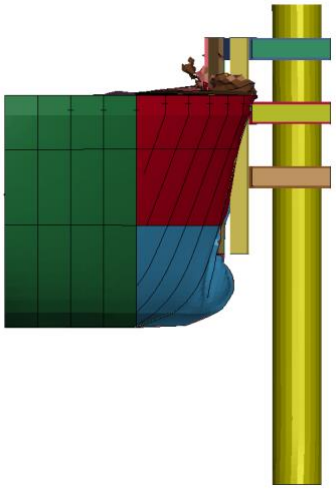	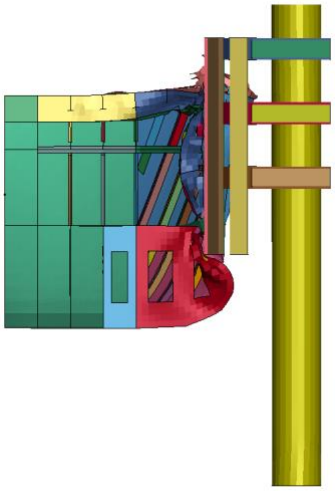
t = 1.0 s	
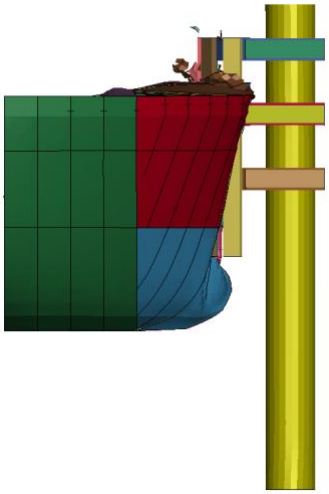	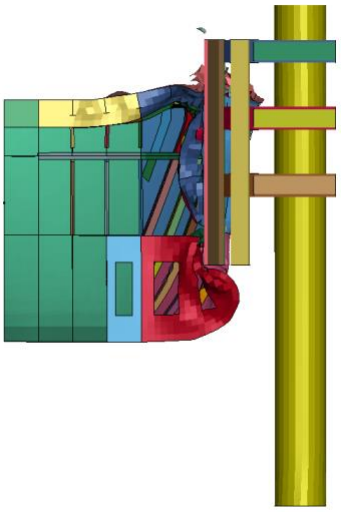

G

Simulation results sensitivity analysis: soil-fender structure (head-on)

Simulation D1	
t = 0.0 s	
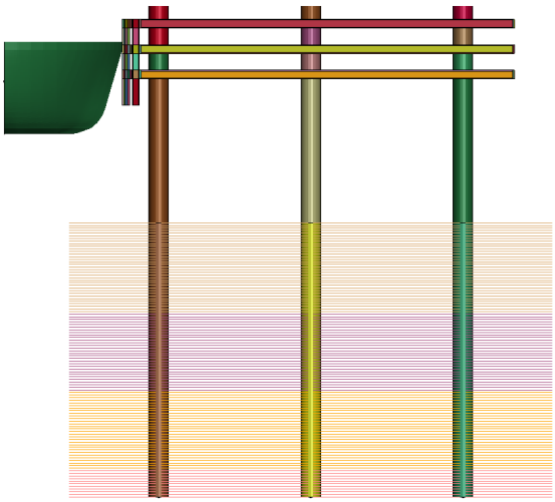	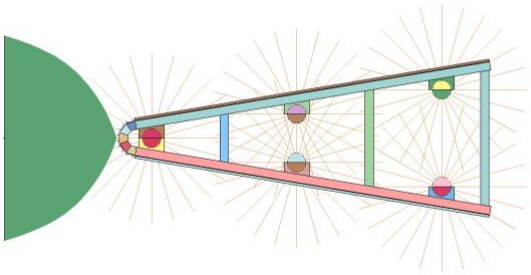
t = 0.50 s	
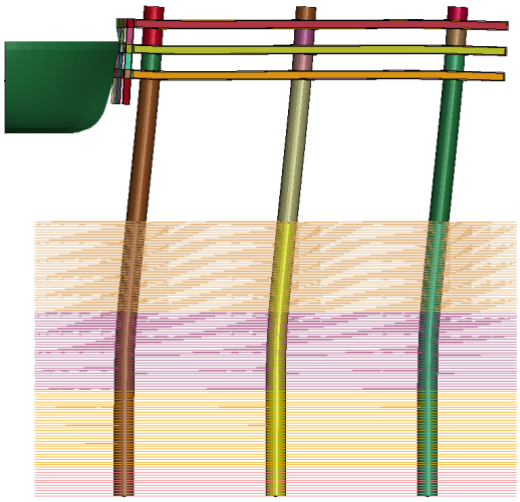	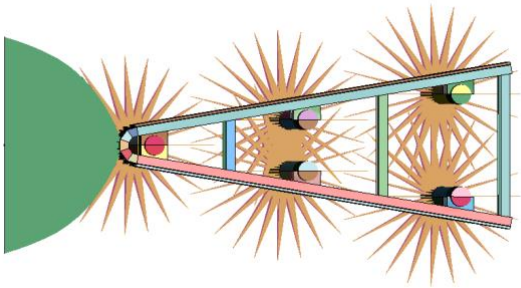
t = 1.00 s	
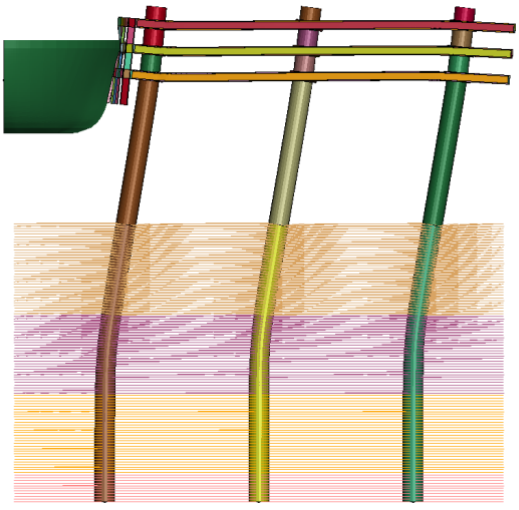	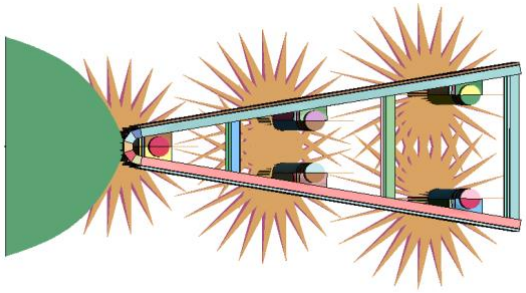

t = 1.60 s

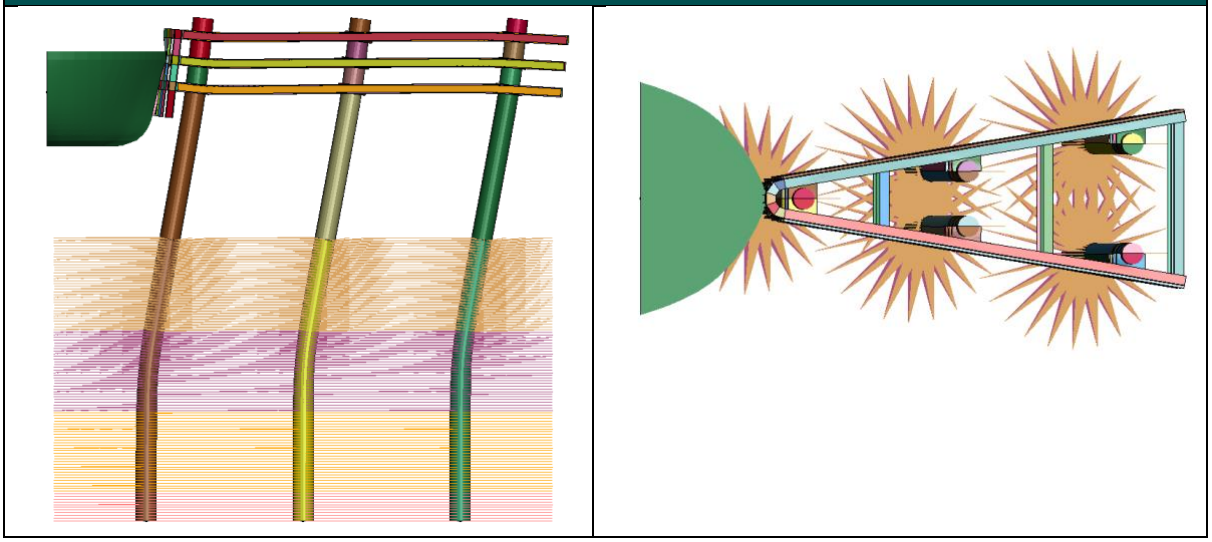

Simulation D2	
t = 0.0 s	
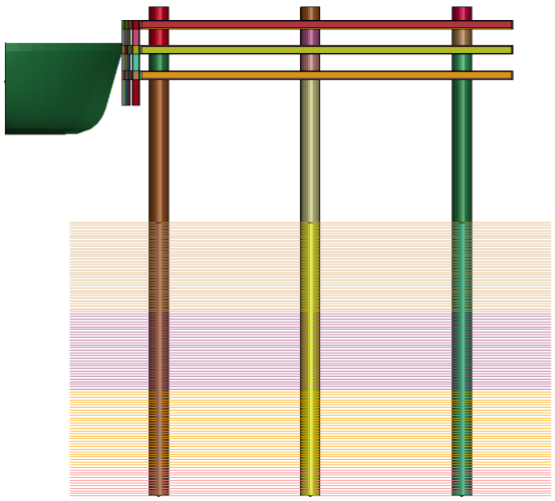	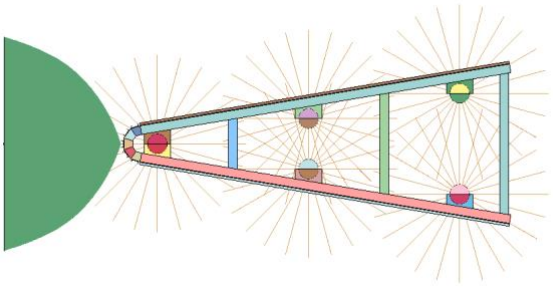
t = 0.50 s	
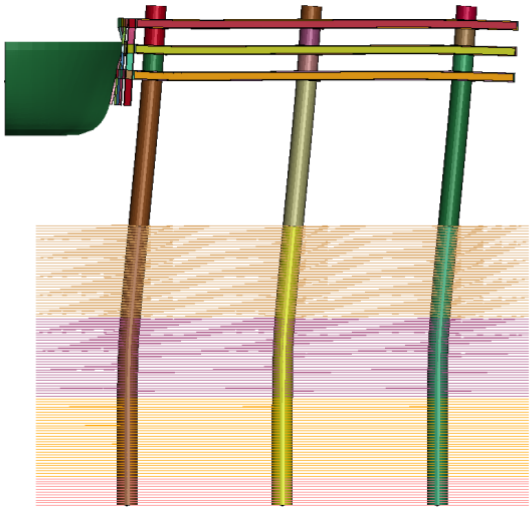	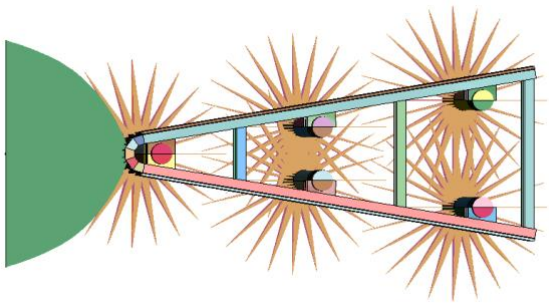
t = 1.00 s	
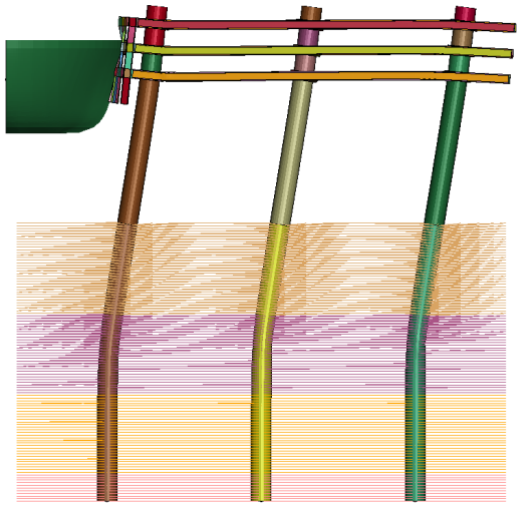	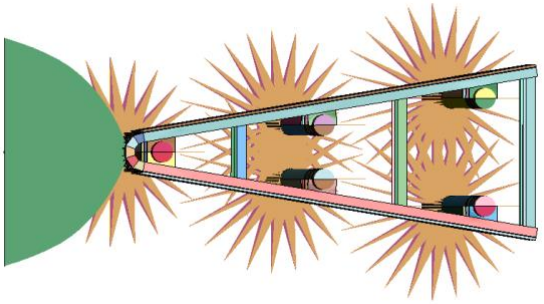

t = 1.60 s

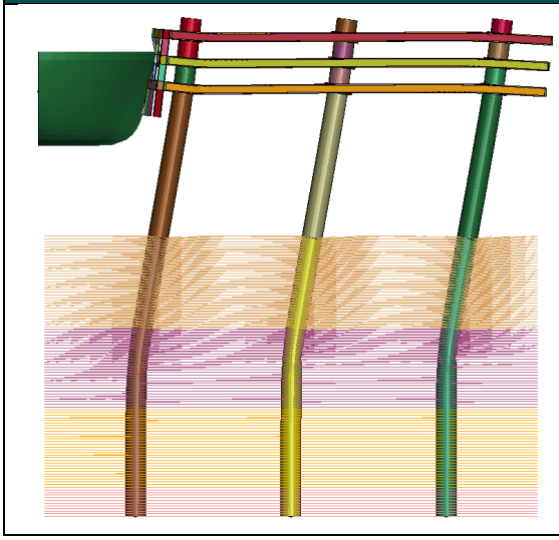

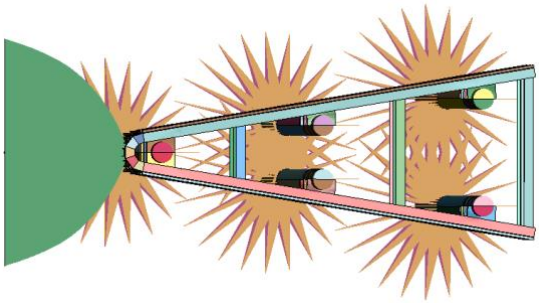

Simulation E1	
t = 0.0 s	
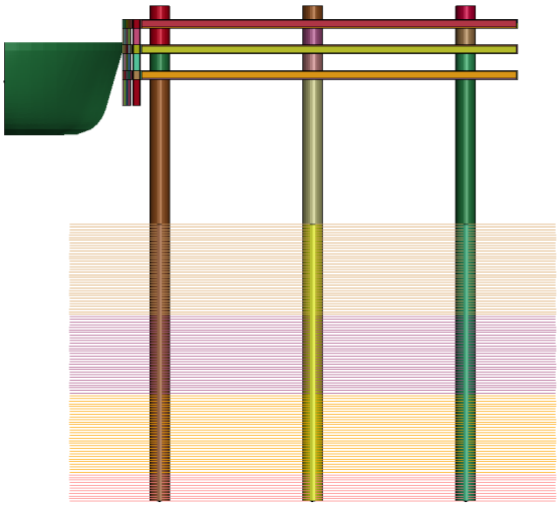	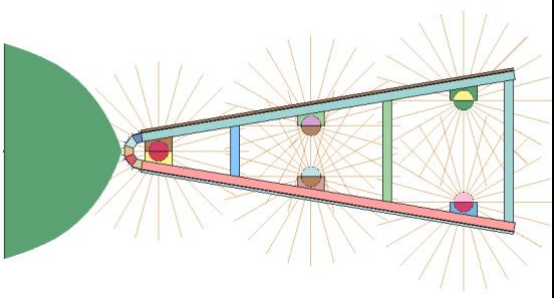
t = 0.50 s	
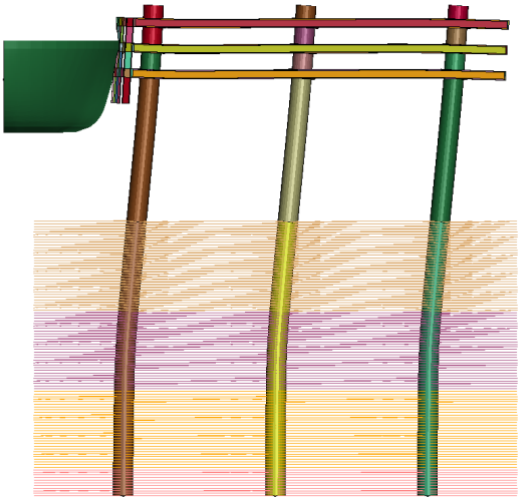	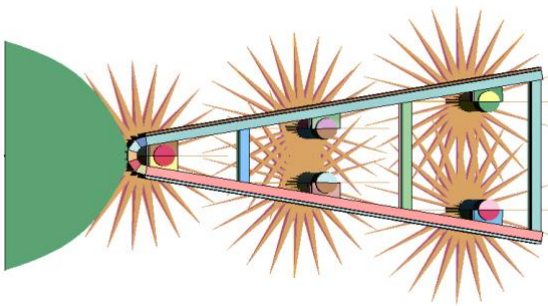
t = 1.00 s	
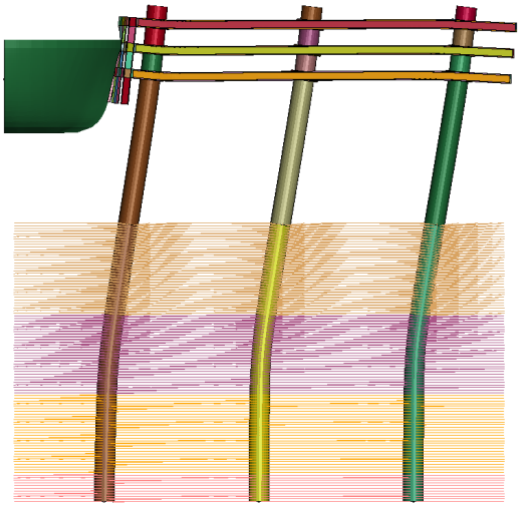	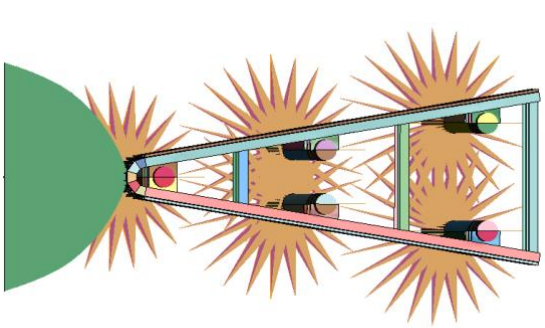

t = 1.60 s

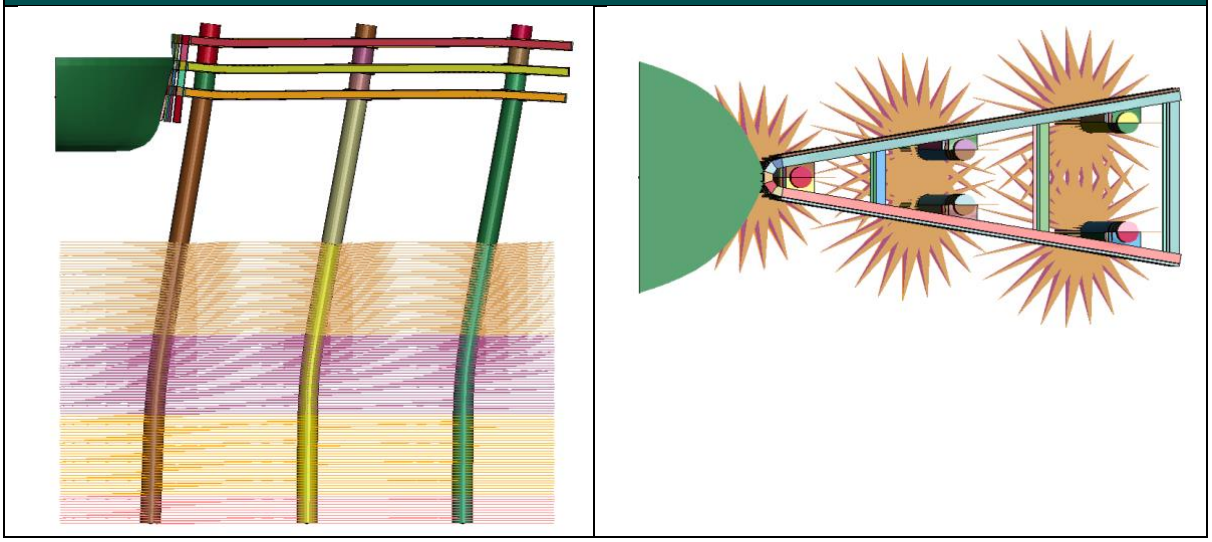

H

Simulation results sensitivity analysis: soil-fender structure (oblique)

Simulation F1	
t = 0.0 s	
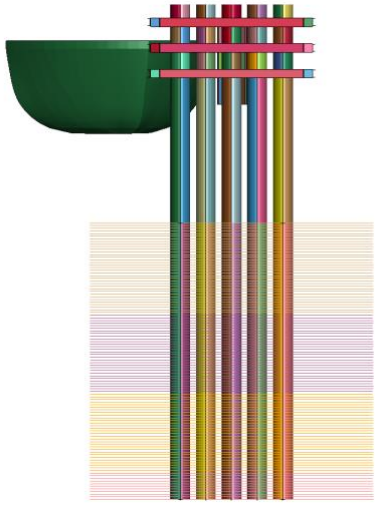	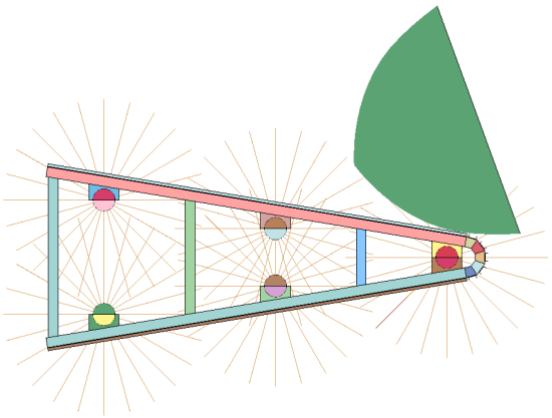
t = 0.50 s	
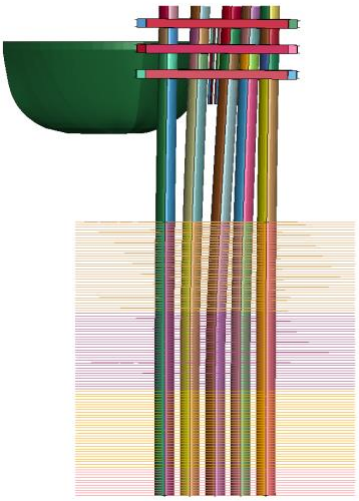	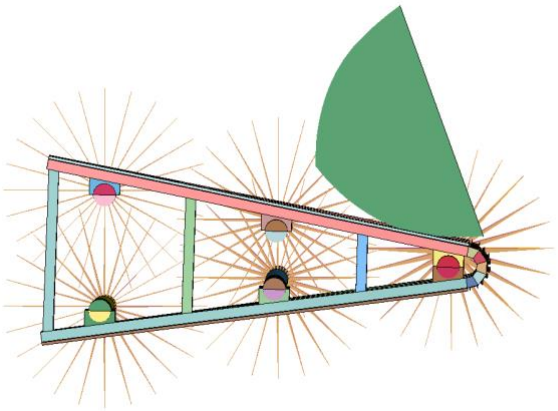
t = 1.00 s	
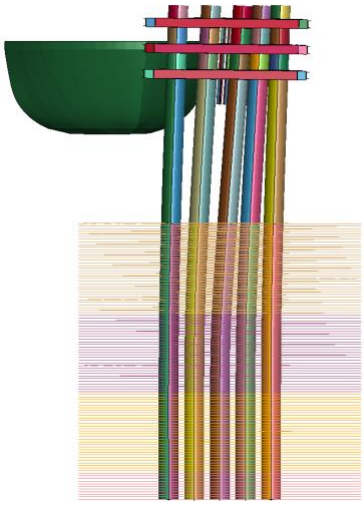	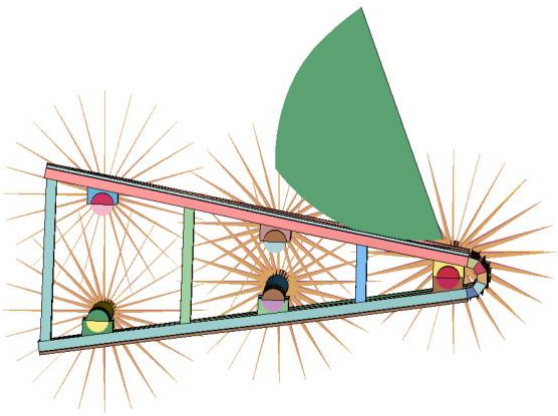

t = 1.50 s	
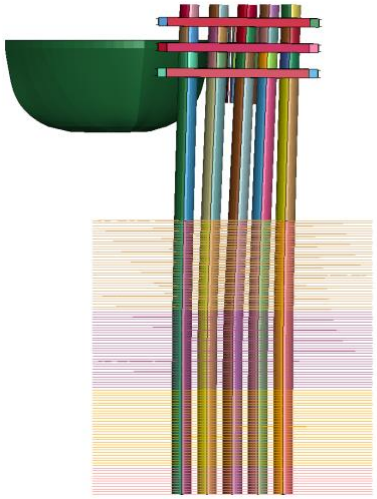	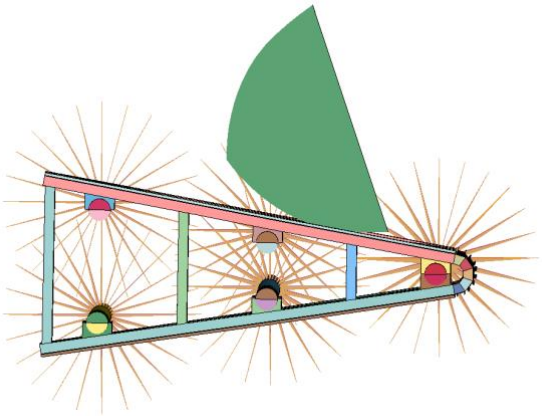
t = 2.00 s	
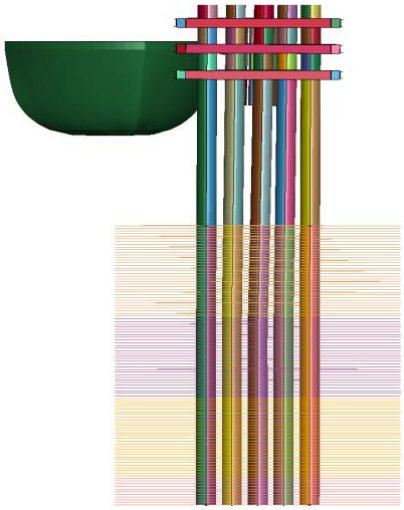	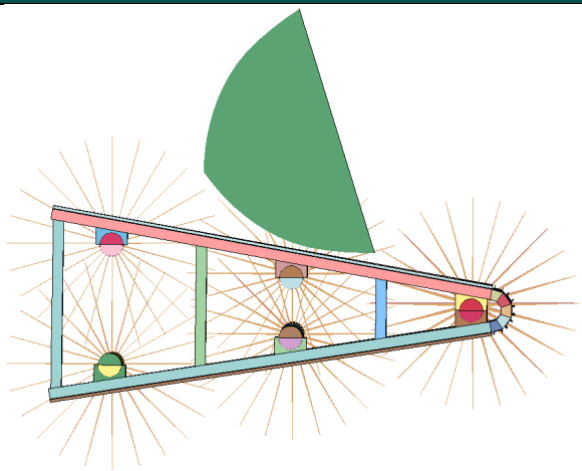

Simulation F2	
t = 0.0 s	
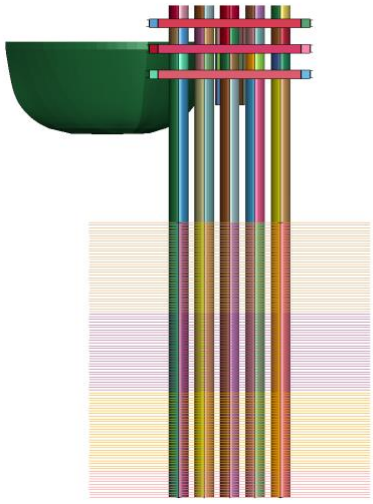	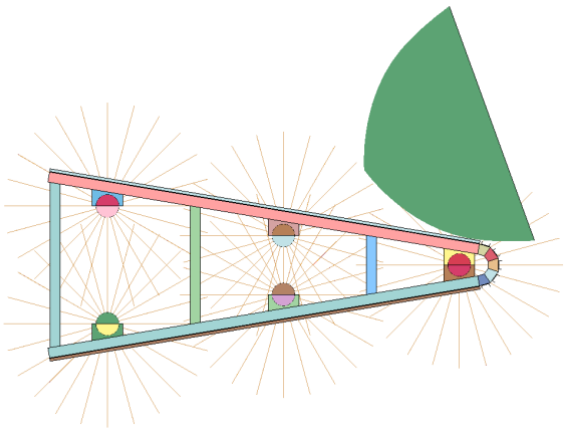
t = 0.50 s	
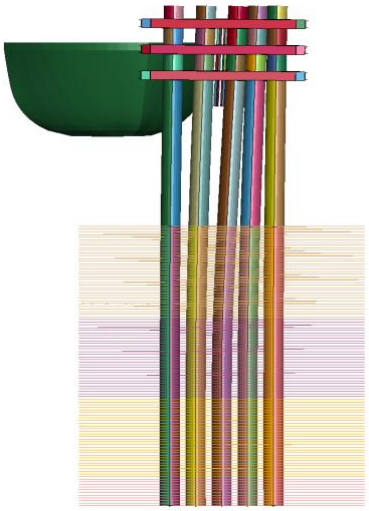	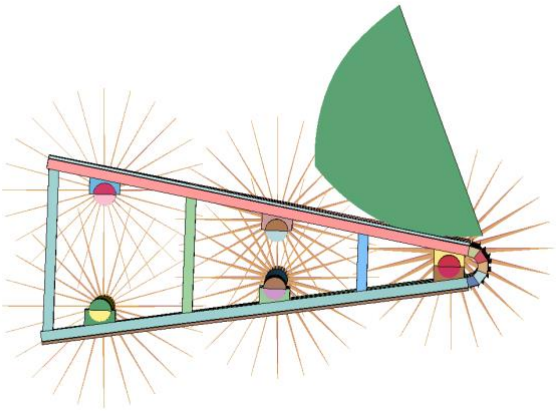
t = 1.00 s	
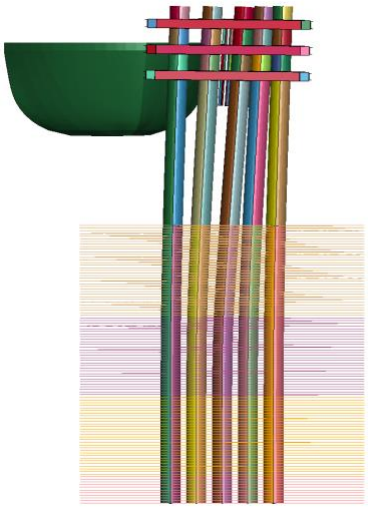	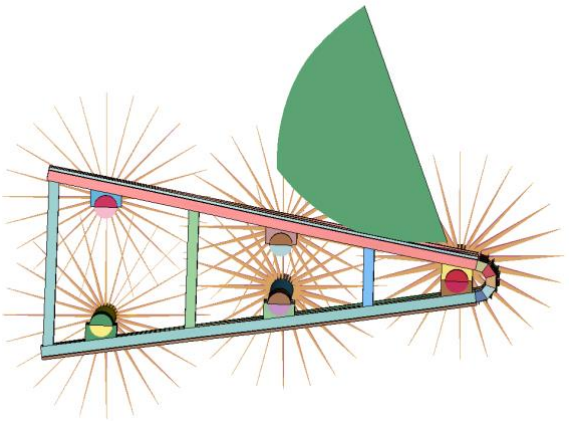

t = 1.50 s	
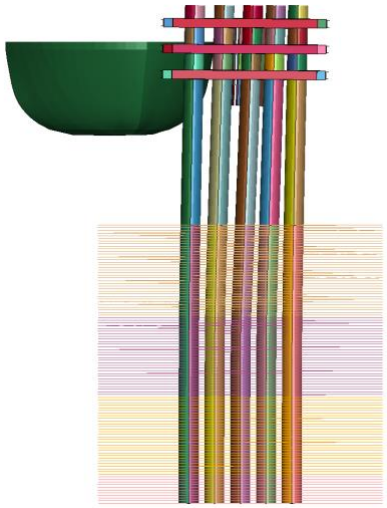	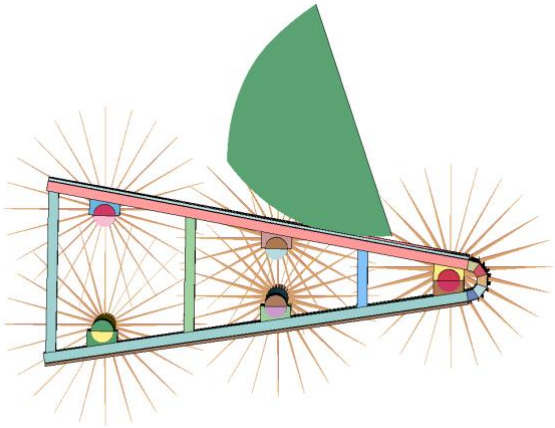
t = 2.00 s	
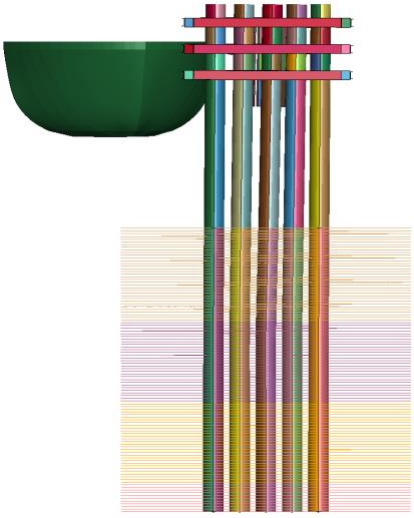	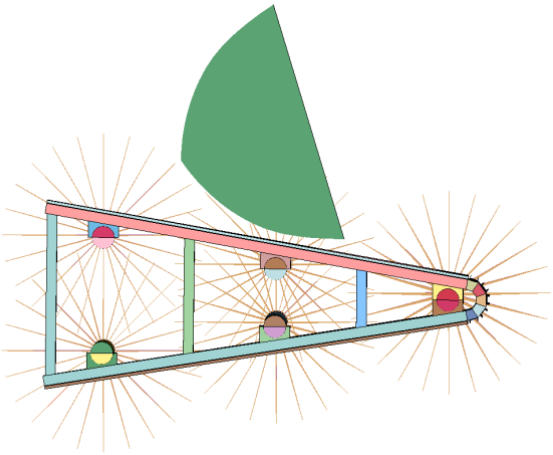

Simulation G1	
t = 0.0 s	
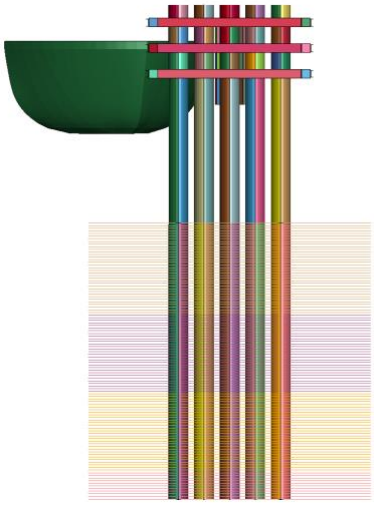	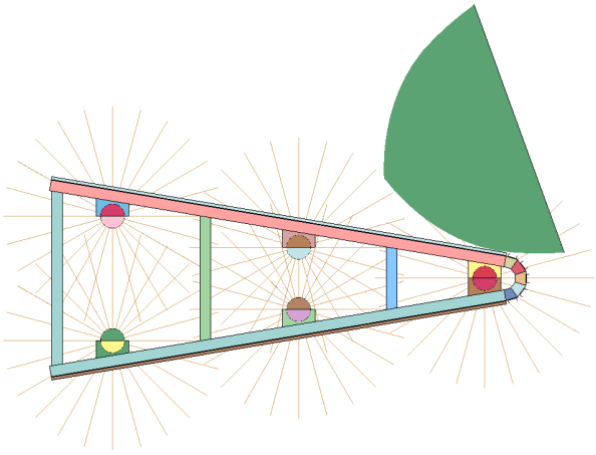
t = 0.50 s	
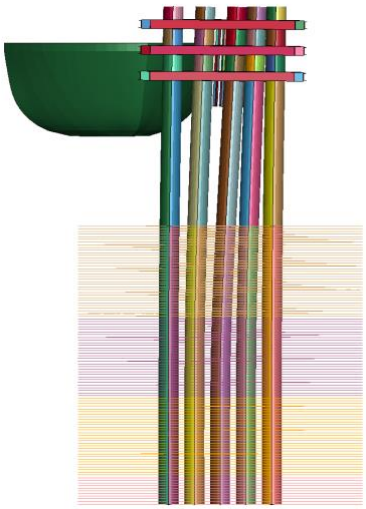	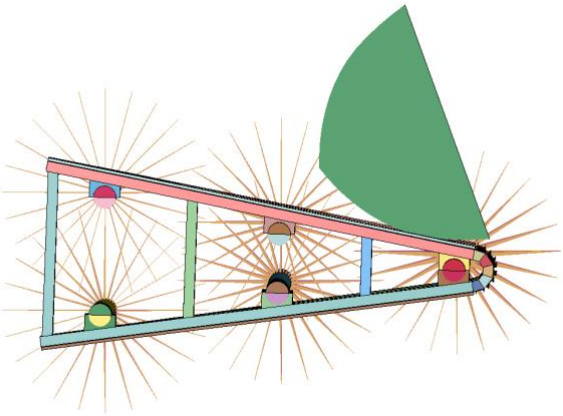
t = 1.00 s	
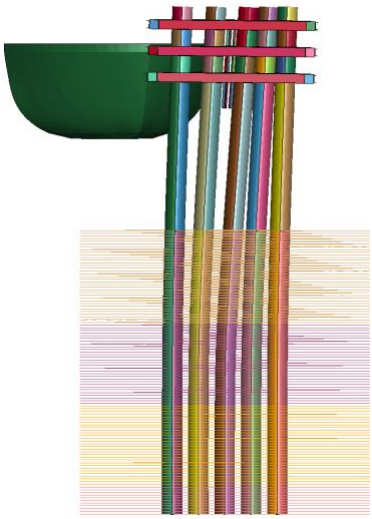	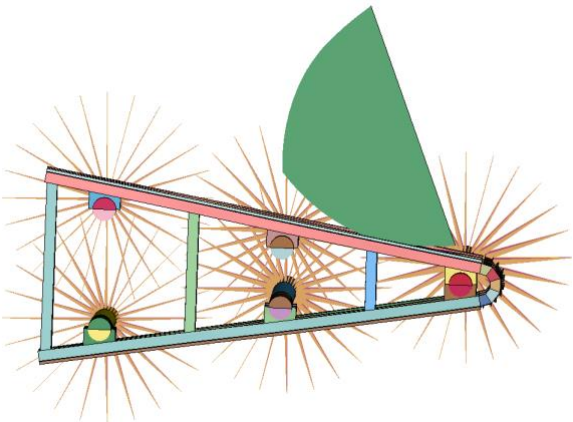

t = 1.50 s	
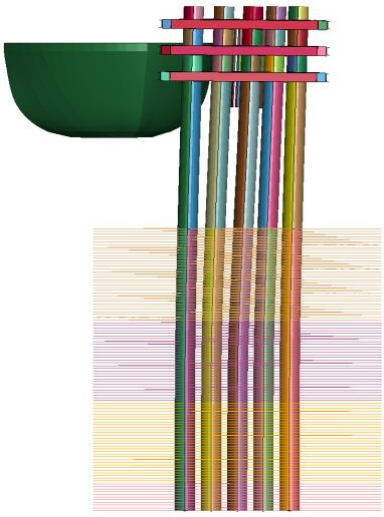	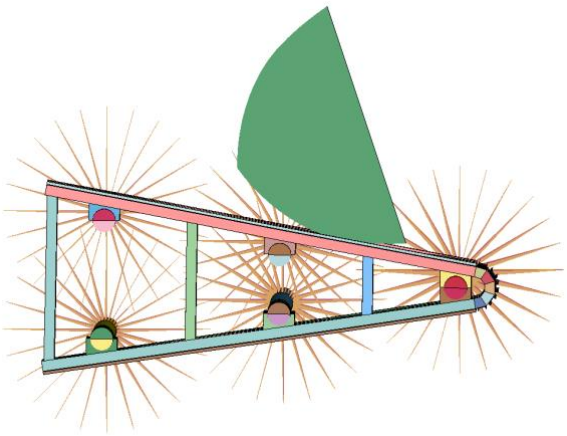
t = 2.00 s	
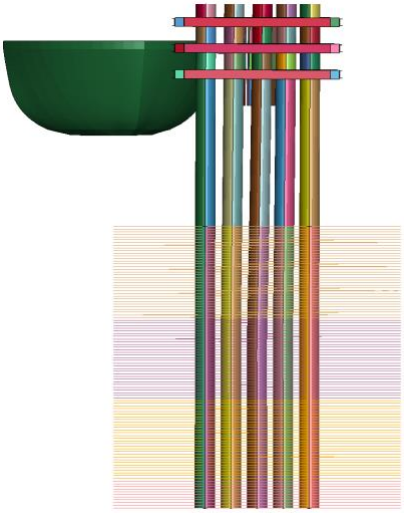	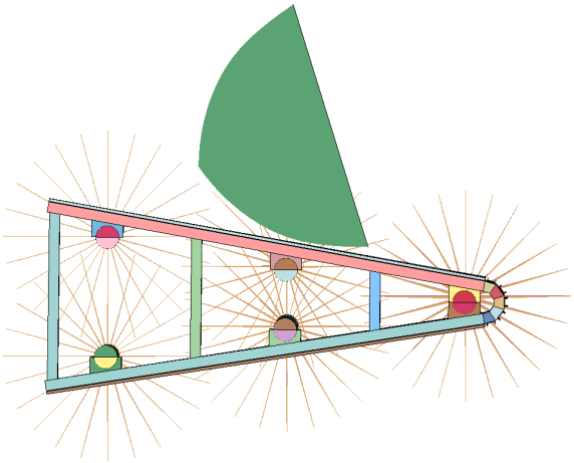

Simulation H1	
t = 0.0 s	
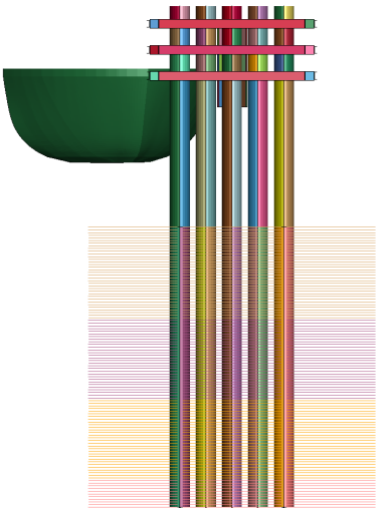	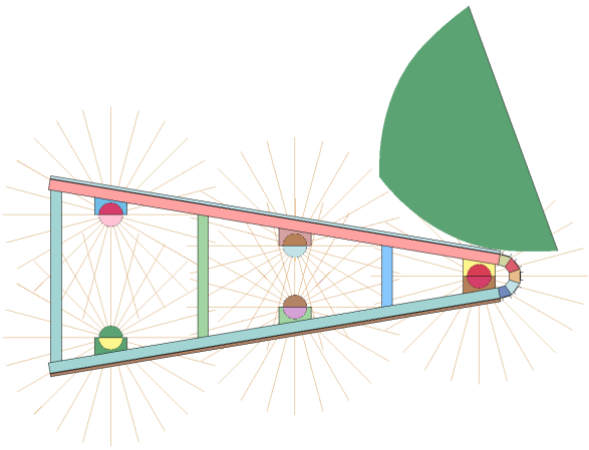
t = 0.50 s	
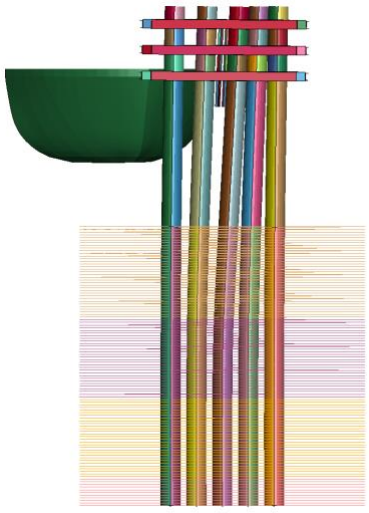	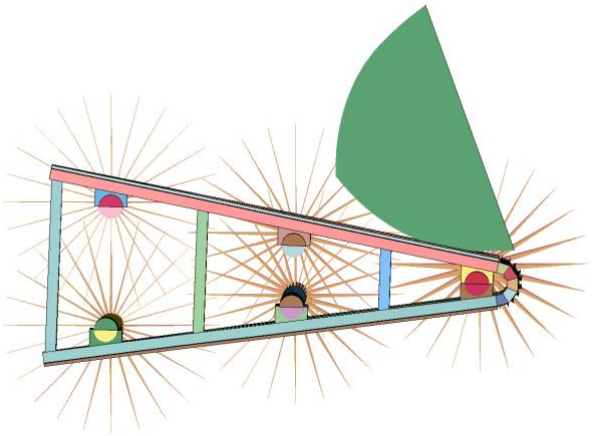
t = 1.00 s	
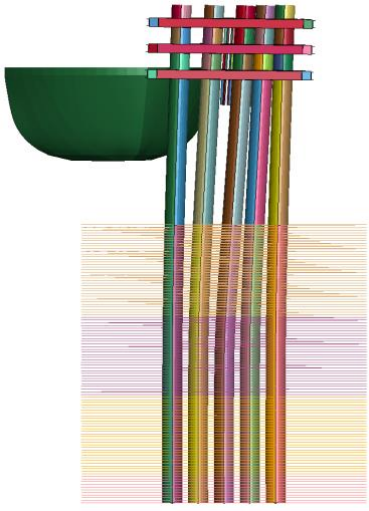	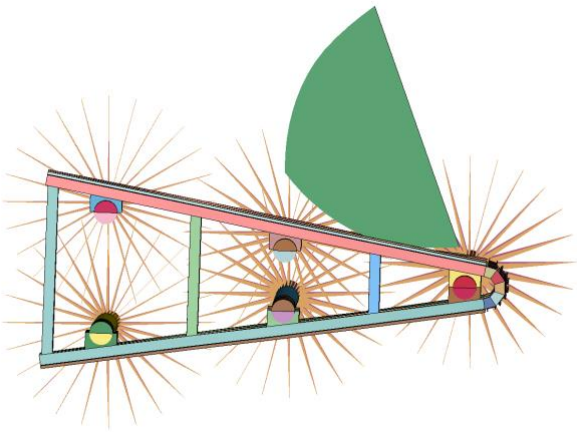

t = 1.50 s	
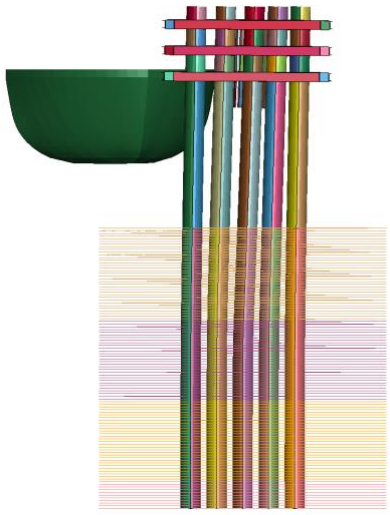	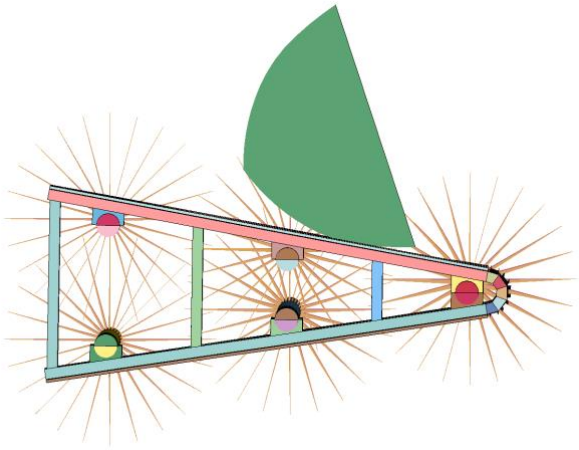
t = 2.00 s	
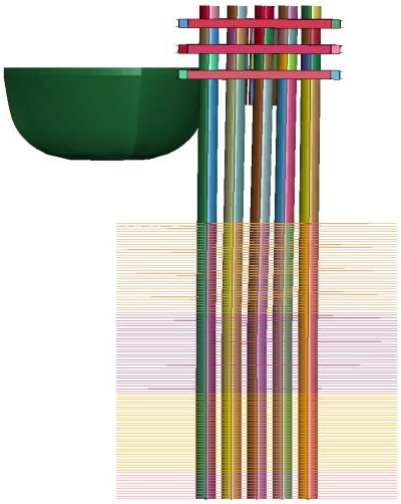	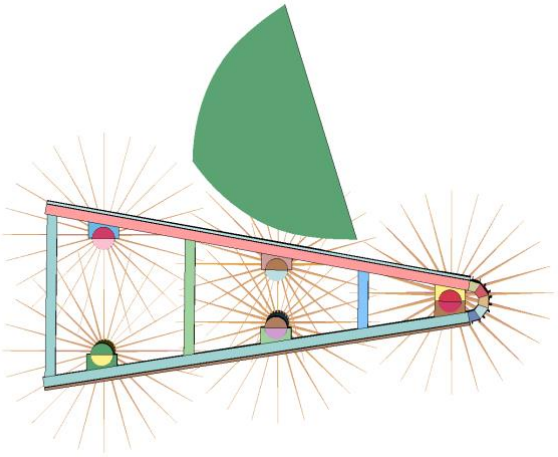

Simulation H2	
t = 0.0 s	
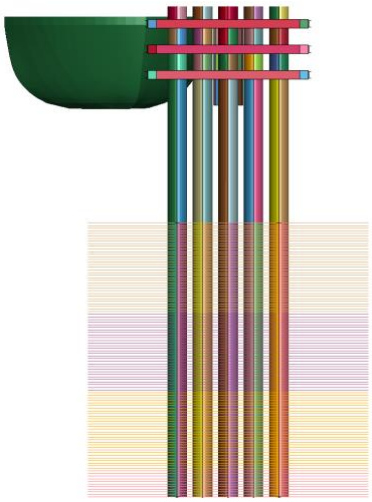	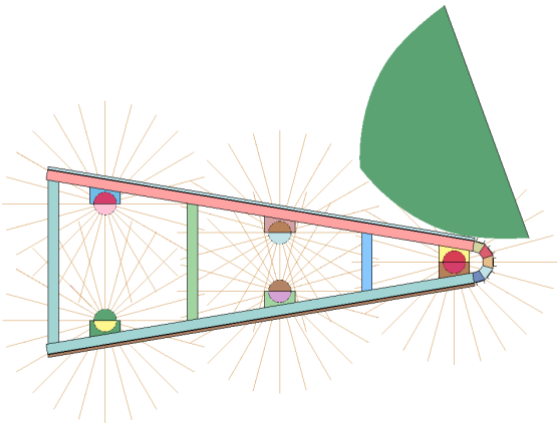
t = 0.50 s	
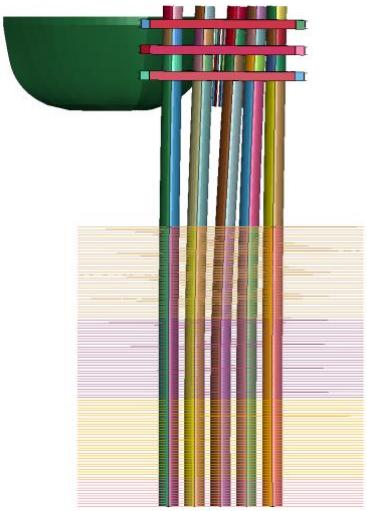	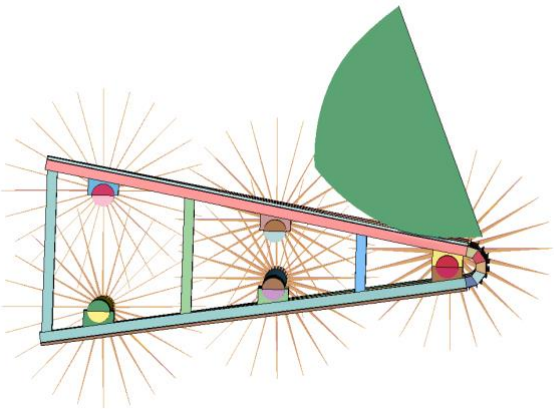
t = 1.00 s	
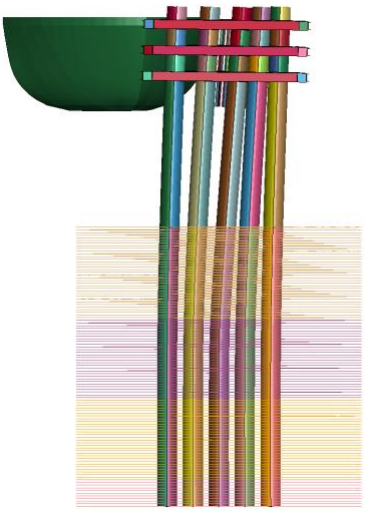	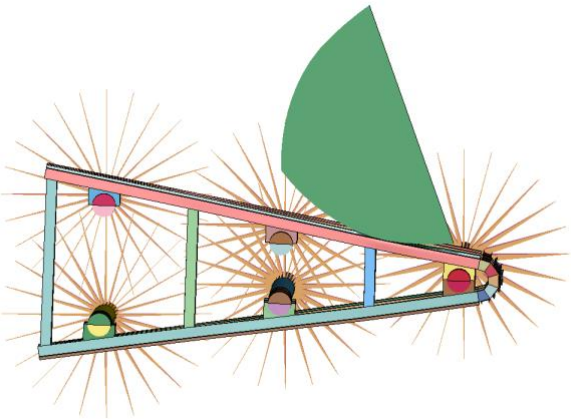

t = 1.50 s	
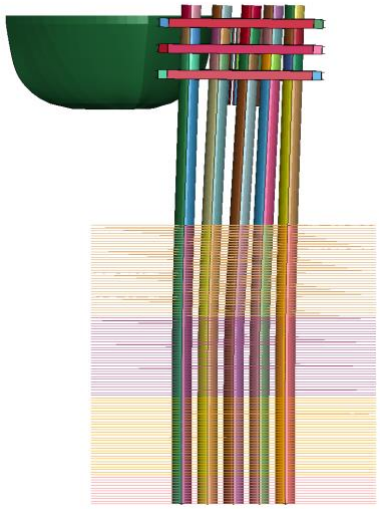	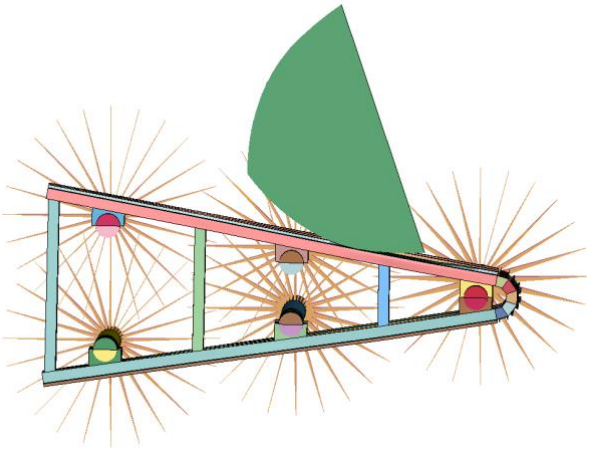
t = 2.00 s	
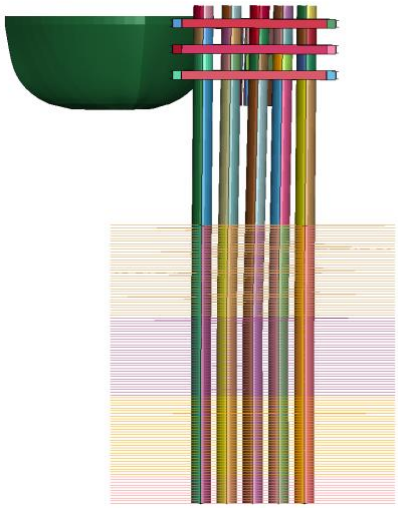	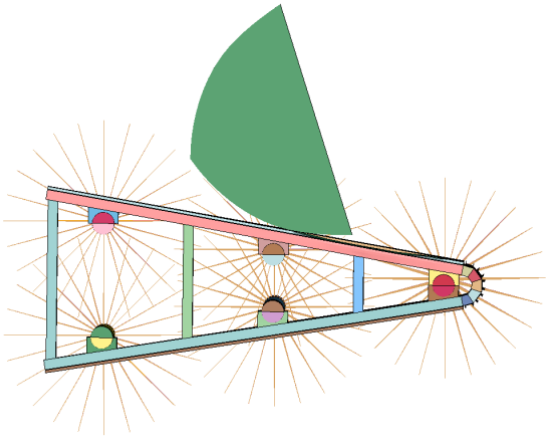

I

Simulation results detailed model

Head-On	
t = 0.0 s	
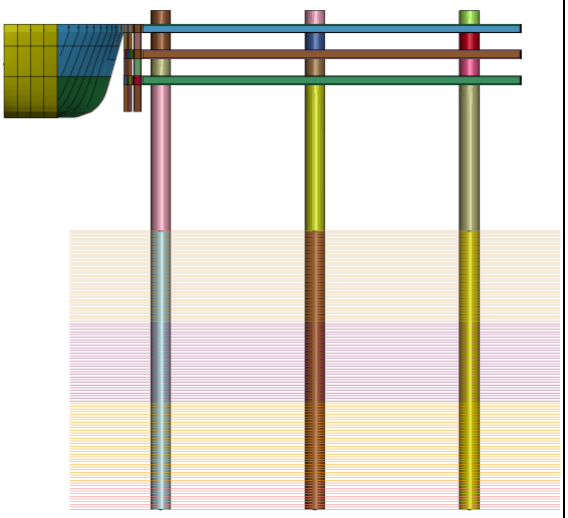	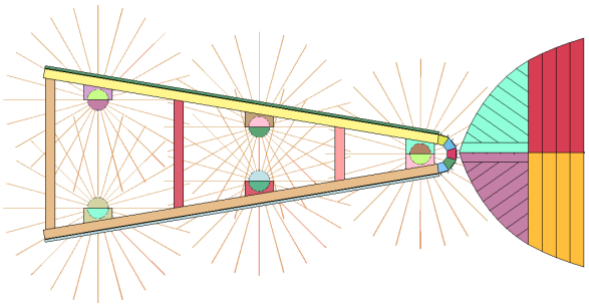
t = 0.50 s	
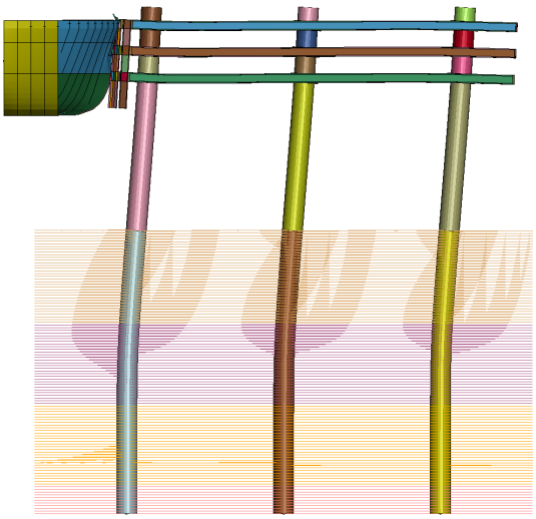	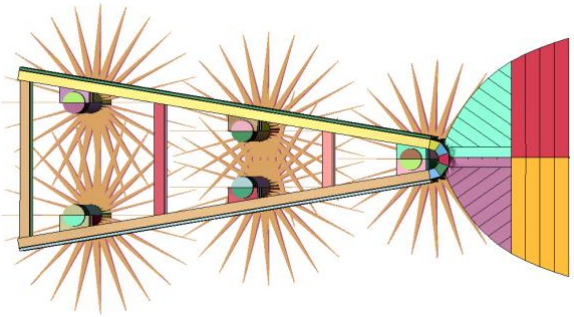
t = 1.00 s	
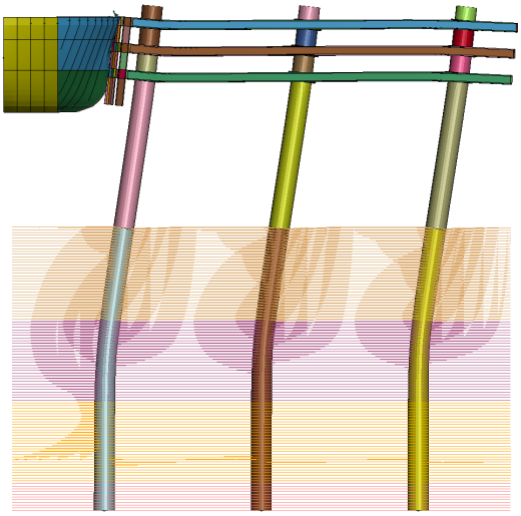	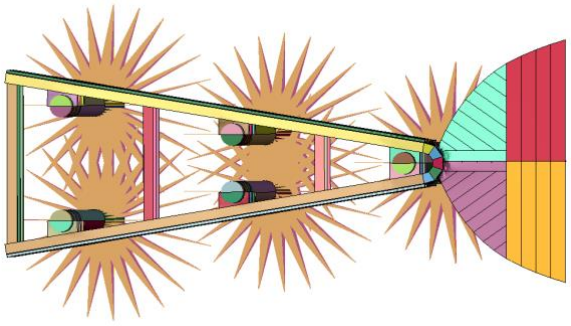

t = 1.50 s

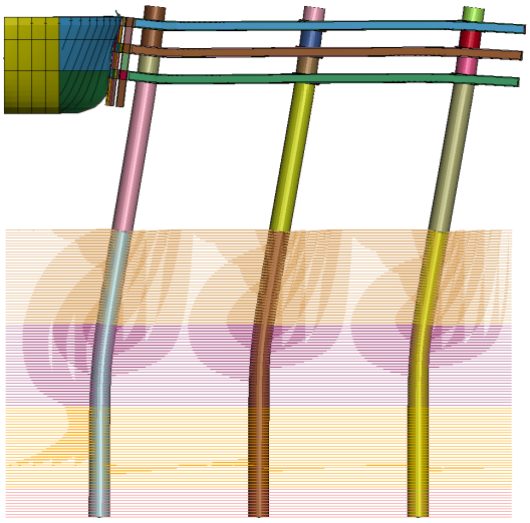

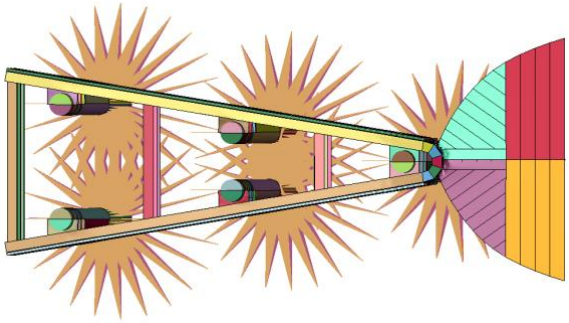

t = 2.00 s

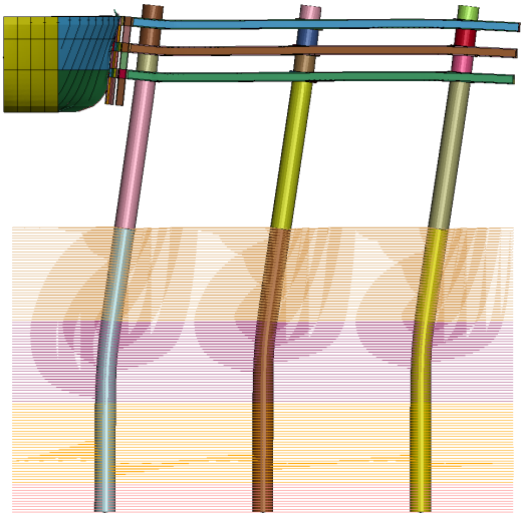

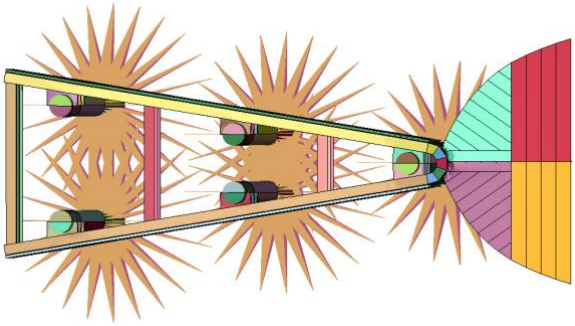

Oblique	
t = 0.0 s	
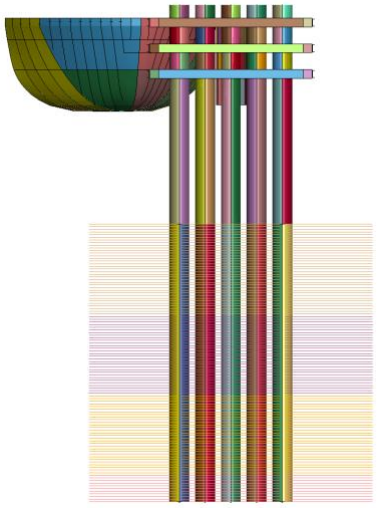	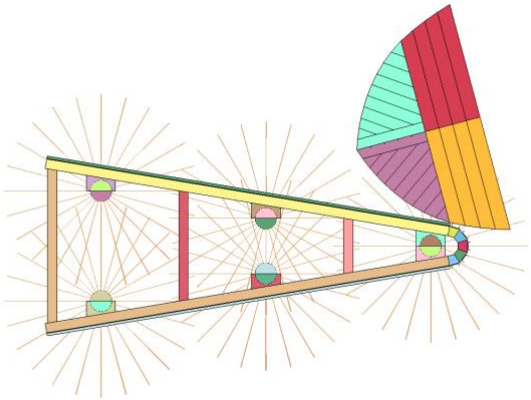
t = 0.50 s	
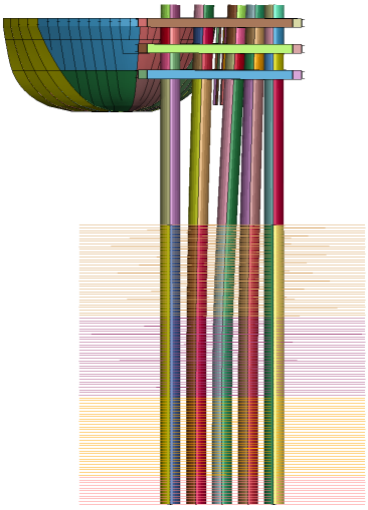	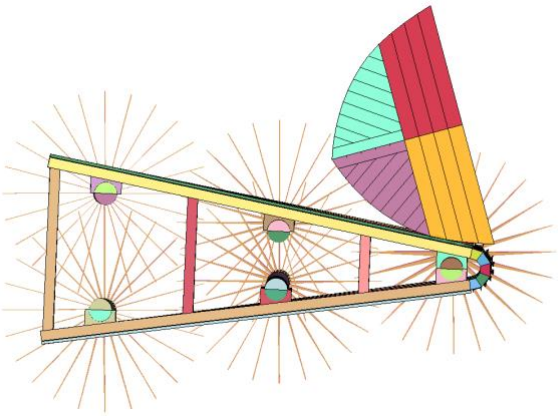
t = 1.00 s	
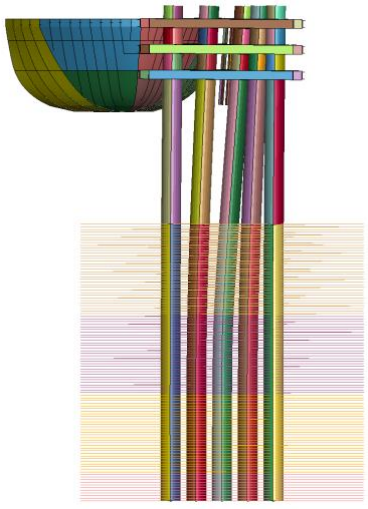	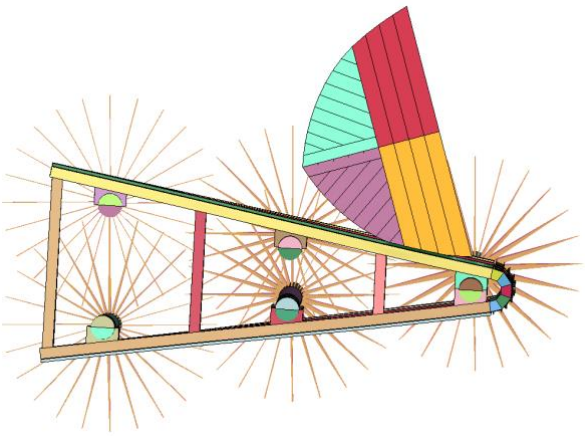

t = 1.50 s	
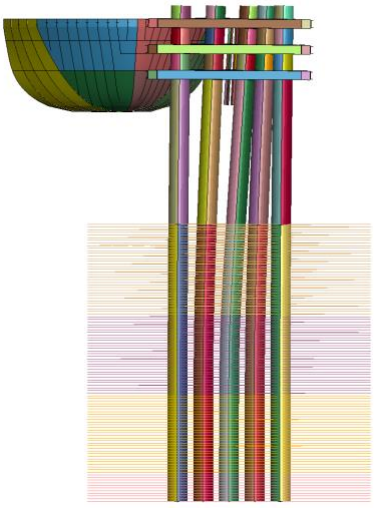	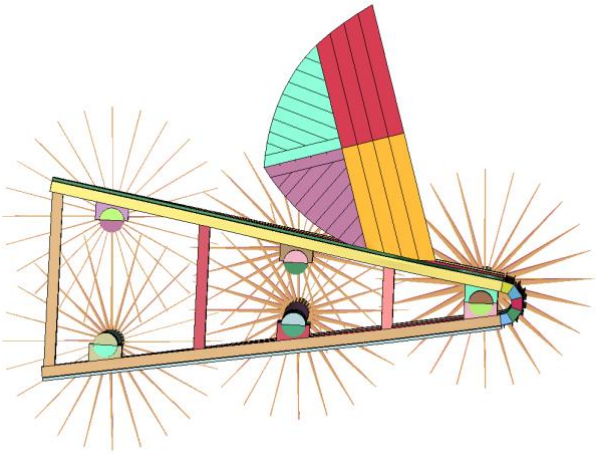
t = 2.00 s